Photocopy and Use Authorization

In presenting this thesis in partial fulfillment of the requirements for an advanced degree at Idaho State University, I agree that the Library shall make it freely available for inspection. I further state that permission for extensive copying of my dissertation for scholarly purposes may be granted by the Dean of the Graduate School, Dean of my academic division, or by the University Librarian. It is understood that any copying or publication of this dissertation for financial gain shall not be allowed without my written permission.

Signature _____

Date _____

Feature Extraction and Pattern Recognition with Fusion Classification

in Infrared Thermal Imaging for Serial Number Restoration

by

Anit Gurung

A thesis

submitted in partial fulfillment

of the requirements for the degree of

Master of Science in the Department of Chemistry

Idaho State University

Summer 2020

This resource was prepared by the author(s) using Federal funds provided by the U.S. Department of Justice. Opinions or points of view expressed are those of the author(s) and do not necessarily reflect the official position or policies of the U.S. Department of Justice.

Committee Approval

To the Graduate Faculty:

The members of the committee appointed to examine the thesis of Anit Gurung find it satisfactory and recommend that it be accepted.

Dr. John H. Kalivas
Major Advisor

Dr. Rene Rodriguez
Committee Member

Dr. Dewayne Derryberry
Graduate Faculty Representative

Acknowledgements

The financial support of the National Institute of Justice through grant number 2017-DN-BX-0173, which has made this project possible, is greatly appreciated. I would like to thank my research committee for giving me the opportunity to work on this project and its dedication to making it a success. I want to express my sincerest gratitude to Dr. John H. Kalivas and Dr. Rene Rodriguez for their support and guidance in every step of the research. I would like to thank Lisa Lau for the experimental setup and thermal imaging data collection. For the Fusion Classification MATLAB code, I want to thank Brett Brownfield, Tony Lemos, who worked under the supervision of Dr. John H. Kalivas.

Table of Contents

List of Figures ix

List of Tables xiii

Abstract xiv

Chapter 1 1

1.0 Introduction 1

1.1 Motivation and Goals 5

1.2 Thesis Structure 6

Chapter 2 7

2.0 Literature Review 7

2.1 Serial Number Restoration 7

2.1.1 Background 7

2.1.2 Methodology 11

2.2 Infrared Thermal Imaging 13

2.2.1 Lock-in Thermography 14

2.2.2 Image Analysis 18

2.3 Pattern Recognition 19

2.3.1 Moment Invariants 21

2.3.2 Classification 25

Chapter 3 29

3.0 Lock-in Procedure 29
3.1 Sample 29
3.1.1 Acquisition 29
3.1.2 Preparation 32
3.2 Experiment Setup 32
3.2.1 Equipment 32
3.3 Setup 33
3.4 Lock-in Thermography Analysis 37
3.5 Image Enhancement 41
CHAPTER 4 45
4.0 ACIP 45
4.1 Image Description 45
4.2 Fusion Classification 51
4.2.1 Reference Classes 52
4.2.2 Classifiers 56
4.2.3 Fusion 61
Chapter 5 70
5.0 Results and Discussion 70
5.1 Stainless Steel (SS) 70
5.2 Gun Barrel (GB) 75

5.3 Laser Engraved Needle Holder (NH) 78

5.4 Discussion 80

Chapter 6 83

6.0 Conclusion 83

6.1 Future Work 84

References 85

Appendix I: Images of Reference Alphanumeric Characters 96

Appendix II: Similar reference class 99

Appendix III: Additional Results 100

List of Figures

Figure 2-1 Types of crystalline metal structure [28] 7

Figure 2-2 Representation of Young's Modulus (E) [8] 8

Figure 2-3 Dislocation motion through crystalline structure of metal [29] 9

Figure 2-4 The relationship between stress and strain based on two types of stainless steel, (a) P675 SS and (b) 303 SS [33] 10

Figure 2-5 Percent transmittance of different infrared wavelength (μm) through the atmosphere [46] 13

Figure 2-6 Schematic diagram of the lock-in imaging process of a certain lock-in period [15] 15

Figure 2-7 Reconstruction of a letter E by a) Legendre moments, b) Zernike moments, and c) Pseudo-Zernike moments; Original Image and reconstructed image using 2nd through 20th order of moments [16] 22

Figure 2-8 Classification using PCA and PLS-DA [85] 26

Figure 2-9 An example of kNN classification [88] 27

Figure 3-1 Stamped Serial Number (2,6,2,5, and 0) on Stainless Steel plate with depth of 0.17mm, 0.15mm, 0.15 mm, 0.16 mm and 0.18mm respectively [1] 30

Figure 3-2 Non-defaced two, partly defaced six, and completely defaced two, five and zero [1] 30

Figure 3-3 Schematic diagram of the experimental setup for infrared lock-in thermography (LIT) [15] 34

Figure 3-4 Thermal imaging with no external heating of stamped serial numbers, 2 (non-defaced) and 6 (partially defaced), on a stainless steel: a) without a black electric tape and b) black electric tape on the surface 37

Figure 3-5 Thermal images (3-dimensional), phase shift (ϕ) and amplitude (A) images for undefaced 2 at each 7 different lock-in frequencies (0.125, 0.25, 0.5, 1, 2 ,4 and 8Hz) 39

Figure 3-6 Thermal images (3-dimensional), phase shift (ϕ) and amplitude (A) images for partially defaced six at each 7 different lock-in frequencies (0.125, 0.25, 0.5, 1, 2 ,4 and 8Hz) . 40

Figure 3-7 Binary image processed from phase shift at optimal lock-in frequency (1Hz) for undefaced two (left) and partly defaced six (right) with two trials: a) Original, b) Replicate..... 43

Figure 3-8 Flow chart of Phase Image Analysis 44

Figure 4-1 Schematic diagram for image description process for reference and phase binary images 45

Figure 4-2 An example of morphological operations performed on binary image converged to different object area percentage a) 35% b) 50% and c) 65%..... 46

Figure 4-3 Scale and Translation invariant object in a unit circle with three different object's proportions: a) 35% b) 50% and c) 65%..... 48

Figure 4-4 Undefaced two (35%) original enhanced binary image and their reconstructed image using fifth-order PZM through 20th order PZM..... 50

Figure 4-5 Feature vectors (20th order, 441 moments) of undefaced two based on two different polynomials, a) Pseudo-Zernike polynomials and b) Radial polynomials. The blue line represents 35%, green line represents 50% and green line represents 65%..... 51

Figure 4-6 Three-Dimensional (3-D) Score Plot; a) RM vs. PZM b) 35% vs. 50% vs. 65% (RM), c) 35% vs. 50% vs. 65% (PZM). 54

Figure 4-7 Fusion Classification input matrix and sum fusion value (undefaced 2 - original) with RM of a specific proportion (35%) and tuning parameter window size of forty-five 62

Figure 4-8 Fusion Classification input matrix and sum fusion value (undefaced 2 - original) with PZM of a specific proportion (35%) and tuning parameter window size of forty-five 63
Figure 4-9 Fusion Classification input matrix and sum fusion value (undefaced 2 - original) with RM of a specific proportion (65%) and tuning parameter window size of forty-five 64
Figure 4-10 Fusion Classification input matrix and sum fusion value (undefaced 2 - original) with PZM of a specific proportion (65%) and tuning parameter window size of forty-five 65
Figure 4-11 Bar plot of Sum Fusion for original of undefaced two (SS) with RM and varying object percentage a) 35%, b) 50% and c) 65%. The magenta color bar represents the lowest sum fusion value (lowest rank)..... 67
Figure 4-12 Bar plot of Sum Fusion for original of undefaced two (SS) with PZM and varying object percentage a) 35%, b) 50% and c) 65%. The magenta color bar represents the lowest sum fusion value (lowest rank)..... 68
Figure 5-1 Phase and Enhanced Binary images of partially defaced Six (SS) 70
Figure 5-2 Bar plot of Sum Fusion for partially defaced six (SS) with RM and varying object percentage a)35%, b) 50% and c) 65%. The magenta color bars represent the lowest sum fusion value (lowest rank)..... 71
Figure 5-3 Phase and Enhanced Binary images of defaced six (SS) 72
Figure 5-4 Bar plot of Sum Fusion for defaced two (SS) with RM and varying object percentage a)35%, b) 50% and c) 65%. The magenta color bars represents the lowest sum fusion value (lowest rank) 72
Figure 5-5 Phase and Enhanced Binary images of defaced five (SS)..... 73

Figure 5-6 Bar plot of Sum Fusion for defaced five (SS) with RM and varying object percentage a)35%, b) 50% and c) 65%. The magenta color bars represents the lowest sum fusion value (lowest rank) 73
Figure 5-7 Phase and Enhanced Binary images of defaced zero 74
Figure 5-8 Bar plot of Sum Fusion for defaced five (SS) with RM and varying object percentage a)35%, b) 50% and c) 65%. The magenta color bars represents the lowest sum fusion value (lowest rank) 74
Figure 5-9 Phase and Enhanced Binary images of defaced one (GB) 76
Figure 5-10 Bar plot of Sum Fusion for defaced two (GB) with RM and varying object percentage a)35%, b) 50% and c) 65%. The magenta color bars represent the lowest sum fusion value (lowest rank) 76
Figure 5-11 Phase and Enhanced Binary images of defaced two (GB) 77
Figure 5-12 Bar plot of Sum Fusion for defaced two (GB) with RM and varying object percentage a)35%, b) 50% and c) 65%. The magenta color bars represent the lowest sum fusion value (lowest rank) 77
Figure 5-13 Phase and Enhanced Binary images of defaced three (NH) 78
Figure 5-14 Bar plot of Sum Fusion for defaced three (NH) with RM and varying object percentage a)35%, b) 50% and c) 65%. The magenta color bars represent the lowest sum fusion value (lowest rank) 79
Figure 5-15 Phase and Enhanced Binary images of defaced four (NH) 79
Figure 5-16 Bar plot of Sum Fusion for defaced three (NH) with RM and varying object percentage a)35%, b) 50% and c) 65%. The magenta color bars represent the lowest sum fusion value (lowest rank) 80

List of Tables

Table 3-1 System Overview of FLIR SC6700 32

Table 3-2 Fixed settings of control variables in the FLIR software..... 35

Table 3-3 Tabulation of Lock-in frequencies and the respective frame rate..... 38

Table 5-1 Defaced serial number on Stainless Steel plate and their selected lock-in frequency. . 70

Table 5-2 Defaced serial number on a Gun Barrel and their selected lock-in frequency 75

Table 5-3 Defaced serial number on a needle holder and their selected lock-in frequency 78

Feature Extraction and Pattern Recognition with Fusion Classification in Infrared Thermal Imaging for Serial Number Restoration

Thesis Abstract -- Idaho State University (2020)

In forensics, identifying the obliterated serial number unique to each firearm is very important in assisting a criminal investigation. A non- destructive method based on infrared lock-in thermography (LIT) and pattern recognition technique were developed for recovery of the defaced serial with marginal human bias. This thesis focuses on assessing the developed semi-automated method for consistency, validity, and comprehensive automation. Amplitude and phase shift using LIT is suitable to distinguish defective and non-defective regions based on differences in thermal emissivity at an optimal lock-in frequency. The technique has a limitation on shallow defects caused by imprint, which leads to low signal to noise ratio. Image analysis, such as smoothing, segmentation, and morphological operations, can enhance feature extraction. Image description technique, such as pseudo-Zernike moments, is used to characterize the extracted feature distinctively. Pattern recognition based on the library of reference alphanumeric characters can be achieved with fusion classification. These techniques are aligned to formulate an automatic character identification protocol (ACIP) for serial number restoration.

Keywords: Infrared Lock-in thermography, Serial number restoration, Thermal emissivity, Feature extraction, Lock-in frequency, Pseudo-Zernike moments, Pattern recognition, and Fusion classification

Chapter 1

1.0 Introduction

Federal law requires manufacturers to engrave a unique serial number on every firearm [1-3]. The serial number is generally removed when guns are associated with criminal activities [4]. Chemical (acid) etching is a standard procedure to restore defaced serial number [4-6]. This technique is effective but destructive and requires highly trained experts. As an alternative, a non-destructive and user-friendly method for recovery of the defaced serial number was developed. This new technique is based on infrared thermography in which an infrared camera captures thermal images to evaluate the apparent temperature. Infrared thermography measures potential temperature (thermal emissivity) differences. The difference is triggered by the change in thermal conductivity with the regions of plastic strain underneath the metal surface. The localized distortion of crystalline structure in a metal due to stamping causes plastic strain [7-9]. There are different ways of collecting thermal images for each thermography, such as lock-in, pulse, and transient, to characterize the temperature differences [10-13].

The developed method is primarily based on lock-in thermography (LIT) of the restoration of an obliterated serial number. Thermal images are captured at a particular frame rate with periodic thermal excitation of a sample using heat sources such as a laser. Based on the lock-in principle, thermal images are integrated to produce amplitude and phase images for each lock-in period [14-15]. The amplitude image can characterize the surface attributes, whereas the phase image is associated with the subsurface. The phase image is less likely to be affected by the temperature gradient on the surface or heat sources. As a result, the phase is more applicable to bring out useful data to distinguish between the stamped and non-stamped region of serial number underneath the metal surface. The ideal lock-in frequency is essential for LIT analysis.

The sensitivity of LIT is high at the optimal frequency, avoiding blind frequencies, which would generate a better phase image.

However, still, there is a limitation to achieve the best possible spatial resolution with a phase image as the temperature difference is very marginal across the surface. The depth of the plastic strain zone is shallow to get any significant variation in temperature. Also, the area of stamped character or force applied to engrave can cause a variety of depth as well as the spread of the plastic strain zone. These factors are unquantifiable to attain accurate local lock-in frequency to extract useful features. As a result, the signal to noise ratio (SNR) on each thermal image is shallow. This issue makes feature extraction using a single-phase image to be less sensitive. Low sensitivity creates enormous complexity for a productive examination of phase image.

The phase image can be simplified to a binary model for further analysis. The optimal threshold depending on the distribution is determined for image binarization. Image smoothing with a box filter can be used to reduce the noise and enhances contrast that can be visually comprehended as any pattern. Image segmentation and morphological operations such as dilation and erosion can be applied to strengthen patterns, which could be applicable for better visual interpretation. It is imperative to decide visually whether the enhanced image resembles the defaced character. The visual representation is likely subject to human bias as the binary phase image can be interpreted differently. Hence, the mathematical description for image characterization can be beneficial to minimize human bias.

The mathematical functions such as geometric moments, Legendre moments (LM), Zernike moments (ZM), and Pseudo-Zernike moments (PZM) have abilities to represent the image features and describe images [16-17]. The application of moment invariants in the field of

pattern recognition has been very useful. However, geometric moments are not orthogonal, and as a consequence, reconstructing the image from the moments is deemed to be a difficult task. Based on the theory of orthogonal polynomials, it can be shown that the image can be easily reconstructed from a set of orthogonal moments, such as Legendre moments, Zernike moments, and Pseudo-Zernike moments. The Pseudo-Zernike moments have the best overall performance among various moments based on noise sensitivity, information redundancy, and image description [17-18]. For this study, the PZM is used to fully characterize the features that generate a unique vector representation of phase image and references. Images are preprocessed to be scale and translation invariant before computation of Pseudo-Zernike moment; the rotational invariance can be achieved. The order of the PZM is determined based on its image reconstruction capability. The predetermined PZM vector generated for the phase image is a basis for pattern recognition.

The underlying pattern described in binary phase image can be classified into a specific letter or a number from a set of thirty-six alphanumeric characters (0-9 and A-Z). There are multiple pattern recognition techniques, such as neural networks, library matching, and classification [19,20]. Neural networks require a large training dataset for simulation, which could only be applicable for digital images. Library matching is usually appropriate when the reference library contains a specific instance of the binary phase image. Classification is a method in which the image is classified into a particular category (class) rather than a single case. It is almost impossible to acquire a phase image for a defaced serial number that could exactly resemble a specific example from a reference library. For serial number restoration, classification is more practical for pattern recognition. The intra-class and inter-class variation among reference categories can be adjusted for classification to function efficiently.

There are multiple methods (classifiers) to perform classification for pattern recognition. Most commonly used stand-alone classifiers such as partial least squares discriminant analysis (PLS-DA) [21,22], and k-nearest neighbors (kNN) [23,24] are based on corresponding tuning parameter values. As a tuning parameter, PLS-DA has a number of latent variables (LVs), and kNN has the number of nearest neighbors and distance measures. The applicability of each stand-alone classifier depends on intra-class and inter-class variation within the data and can be optimized with a tuning parameter. Tuning parameter selection is a complex problem with no concrete consensus. In addition, there are similarity measures, such as cos θ and Euclidean distance, that can be considered as non-traditional classifiers with no tuning parameters. The purpose of these classifiers is to evaluate the degree of similarity between unknown and class mean. All classifiers utilize a piece of specific information which suggests variability, likely prompting misclassification with method selection.

These classifiers can be ensembled to obtain robust classification with consensus and improved pattern recognition. There are two approaches to combine classifiers. Grouping of classifiers based on one single algorithm is one approach [25]. Random Forest is one of these types of methods. The purpose of this approach is to create a robust classifier from a collection of weak classifiers. The other outcome is to combine the result of multiple optimized classifiers. For better performance, eventually, these methods require the optimization of tuning parameters associated with each classifier.

The alternative approach is fusion classification [26]. For fusion classification, non-optimized classifiers are fused based on the respective window of tuning parameter values instead of selecting an optimal tuning parameter value. For better consensus, non-traditional classifiers are stacked with non-optimized classifiers. An appropriate fusion process, sum fusion

rule, is used [26,27]. The sum fusion is the sum of the normalized raw values (across classes) computed for each classifier. For each tuning parameter window, the lowest sum for a category associated with the alphanumeric character is predicted to the defaced number or letter. The majority vote, another fusion approach, is applied to the outcomes of all tuning parameter windows. The consensus for pattern recognition with fusion classification is achieved.

1.1 Motivation and Goals

The motivation of this study is to enhance the previously developed non-destructive method for serial number restoration and create a robust automated process for identification of recovered defaced serial number. The overall goal of this project is to determine the best-fitted control variables and measurements for infrared lock-in thermography and develop an automatic character identification protocol (ACIP) to recover the defaced serial number.

These goals were attainable with the digital device's availability for accurate measurements and an additional image analysis application, including feature enhancement and pattern recognition techniques. For the completion of this study, the three primary goals are presented as follows:

1. To evaluate experimental design, including sample preparation and environment, for collecting thermal images.
2. To assess the efficacy of infrared lock-in thermography for feature extraction.
3. To develop an automatic character identification protocol (ACIP – black box) that is user-friendly and minimizes human bias for serial number restoration.

1.2 Thesis Structure

This thesis is organized with multiple chapters (sections) illustrated as follows: Chapter 2 outlines a review of relevant literature and background information for serial number restoration, feature extraction using infrared lock-in thermography, and image analysis. Chapter 3 describes the experimental design, including sample preparation, environment, and control variables to collect thermal imaging data based on the LIT review. Section 4 outlines ACIP for pattern recognition, including image preprocessing, feature enhancement, creation of reference library, image description, and classification. Chapter 5 provides results for different samples based on ACIP applied to image generated using LIT analysis. Section 6 contains the conclusion of all studies carried out in the project and the future work.

Chapter 2

2.0 Literature Review

This section presents a brief literature review of several concepts, fundamentals, and background which are related to serial number restoration, infrared lock-in thermography, and image analysis; such as plastic and elastic deformation underneath the metal surface, infrared radiation, thermal conductivity and emissivity, lock-in principles, and multivariate image analysis.

2.1 Serial Number Restoration

The manufacturers of firearms are required by the Gun Control Act of 1968 to engrave a unique serial number for identification. In forensics, tracing a gun is essential to speed up the criminal investigation when firearms are involved. The serial number is generally removed, which can act as evidence of the crime scene. The restoration of a defaced serial number would be beneficial.

2.1.1 Background

Most firearms are made up of metals such as iron, aluminum, zinc, or alloy. Different techniques such as die-stamping (mechanical) and laser etching are used to stamp a serial

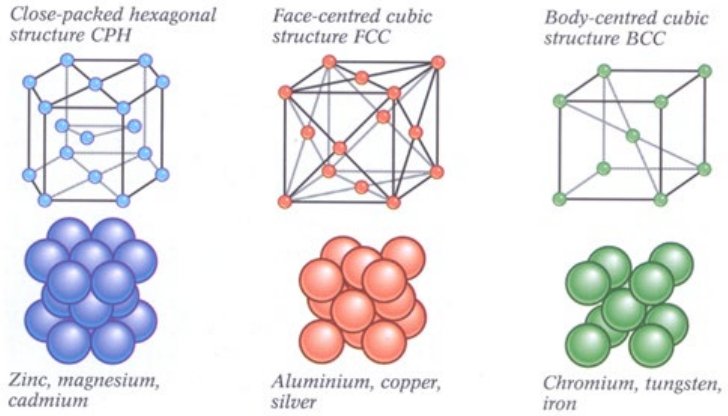

Figure 2-1 Types of crystalline metal structure [28]

number on the metal surface. The atoms of pure metals are arranged in a closely packed pattern, which gives the crystalline structure. As shown in Figure 2.1, the most common arrangements are body-centered cubic (BCC), face-centered cubic (FCC), and close-packed hexagonal (CPH). Each unit cell of the crystalline structure is called grain. These arrangements of grains determine the physical and chemical properties of the metal.

While stamping a serial number on the metal surface, an enormous force or external energy is applied, which could distort the arrangement of atoms. The distortion leads to the alteration of the crystalline structure underneath the metal surface. Figure 2.2 shows the graphical representation of Young's Modulus (E), which measures the elasticity of a metal.

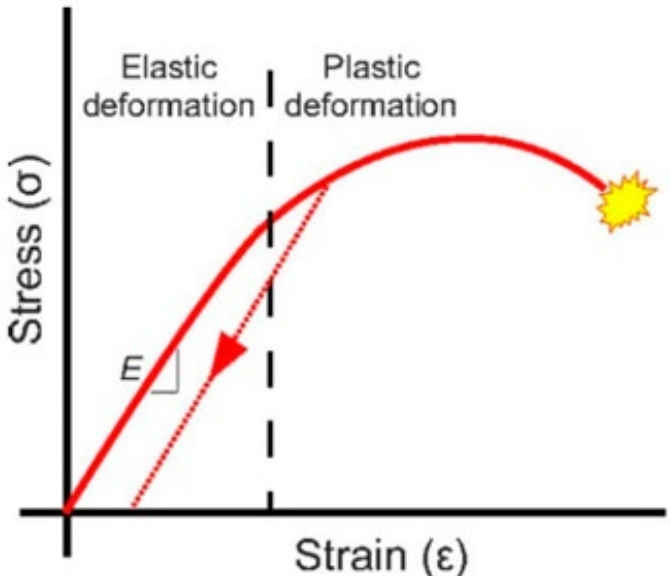

Figure 2-2 Representation of Young's Modulus (E) [8]

The severity of deformation depends on the ratio of stress (σ) by strain (ε) of the metal. Stress is defined as the force applied over the metal surface area. A strain is defined as deformation caused by stress. Elastic deformation occurs up to the point where the crystalline structure is stretching and not deforming. If the metal is stressed beyond that point, the grains in the metal will begin to distort and permanently change the crystalline structure. This

phenomenon is called plastic deformation. Figure 2.3 demonstrates how the grains dislocate and penetrate through the crystal when the stress is applied.

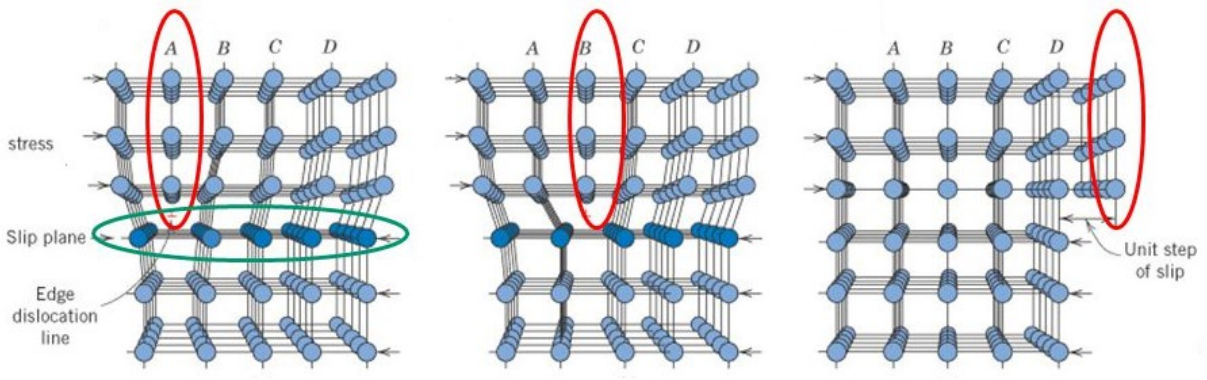

Figure 2-3 Dislocation motion through crystalline structure of metal [29]

The change in the crystalline arrangement of this local zone of plastic strain causes localized changes in the metal physical properties such as thermal conductivity (k) and emissivity (ε) and density [30,31]. Metals are a good conductor of heat due to a large number of free electrons moving about the crystalline structure. When the structure is distorted, the electrons cannot move freely. This phenomenon results in reducing the thermal conductivity in the localized plastic strain region from the non-deformation area underneath the metal surface. The relationship between the thermal emissivity perpendicular to the polished metal surface and thermal conductivity of pure metal can be described by Equation 2.1 [32].

$$\varepsilon = \left(1.0 \times 10^{-4}\right) \times \mathrm{T} \times k^{-\left(\frac{1}{2}\right)} \tag{2.1}$$

where:

ε is the thermal emissivity of a polished metal surface

T is the absolute temperature of a metal (K)

k is the thermal conductivity (W cm^{-1} K^{-1})

The lower thermal conductivity of the plastic strain region possibly contributes to slightly higher thermal emissivity. Also, the dislocation density increases with deformation. These changes affect the temperature gradient of the deformed area to be different from the non-deformed area.

The magnitude of the plastic strain depends on metal properties and the indentation geometry used for engraving serial numbers. Figure 2.4 illustrates plastic strain for two types of stainless steel (P675 SS and 303 SS) and how this relates to the zone of plastic deformation [33].

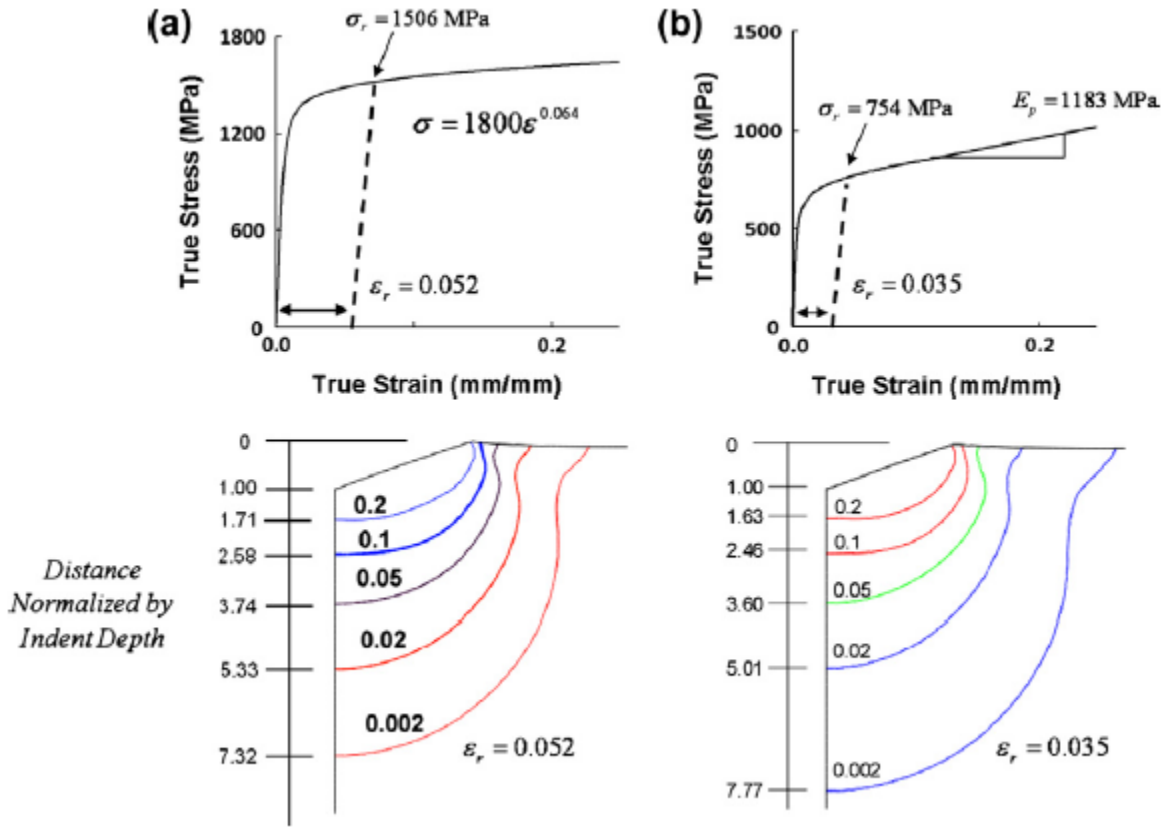

Figure 2-4 The relationship between stress and strain based on two types of stainless steel, (a) P675 SS and (b) 303 SS [33]

The magnitude of plastic deformation decreases with the depth of the distortion until the point where there is elastic or no strain. Hence, the bottom of the obliteration is an essential part of recovering defaced serial number. As the depth of the defacing increases, the degree of accuracy

This resource was prepared by the author(s) using Federal funds provided by the U.S. Department of Justice. Opinions or points of view expressed are those of the author(s) and do not necessarily reflect the official position or policies of the U.S. Department of Justice.

for serial number restoration diminishes. Eventually, when the defacing reaches or exceeds the extent where there is elastic or no deformation, it becomes impossible to recover the defaced serial number.

Generally, methods to obliterate serial numbers involve standard procedures that will remove enough surface material up to the depth where the serial number is no longer visible with naked eyes. These include filing, sanding, and scraping with a sharp tool, that is likely not to create any zone of plastic deformation underneath the metal surface. This condition will allow for the high possibility of serial number restoration. Nevertheless, overstamping on the serial number is another method which can cause similar plastic strain as the actual serial number imprint. This filing technique could blur the subsurface pattern of plastic deformation and create false identification of a restored serial number.

2.1.2 Methodology

Multiple methods have been tested for serial number restoration. These methods utilize the localized change in the region's physical and chemical properties with plastic deformation relative to the non-stamped area. Some of the established methods are chemical etching and electrolytic etching [34]. Electron backscatter diffraction (EBSD) with scanning electron microscopy [35-37], and magnetic particle inspection [38] are newly developed methods.

Traditional methods are destructive and require expertise. The most commonly used way is chemical etching. This method examines the corrosion process where there is a difference in the reaction rate between the engraved and non-engraved areas to the chemical reagent (acid). Depending on the metal, the proper composition of chemical reagents is used to achieve the best visible contrast between defaced and clean areas on the metal surface [39-43]. The electrolytic etching is similar to chemical etching in which an electric field is applied to control the etching

process. The electrolysis of the metal is used to speed up or slow the reaction rate. The optimal voltage depending on the metal is determined to get the best result for restoring the serial number. In these techniques, the use of highly concentrated acid solutions during the etching process has a significant drawback as it permanently destroys whether the defaced serial number was restored entirely or not.

Newly developed methods are designed to be non-destructive. These methods have not been entirely successful compared to traditional techniques, but these techniques can still be used as an alternative. The most commonly used non-destructive method is a magnetic particle inspection. This technique relies on the difference in magnetic permeability between the zone of plastic deformation and the non-deformed region for recovery of the defaced serial number. Although this method is relatively successful for serial number restoration, it has limitations. This method is only applicable to metals that have magnetic properties and primarily mechanical stamping approaches. Another non-destructive method currently in development is EBSD with scanning electron microscopy. This technique assesses the diffraction pattern of electron beam targeted onto stamped and non-stamped area by mapping crystallographic orientation at high resolution. EBSD software for quality mapping is implemented to generate the best visual contrast. During the experimental stage, this method has shown the potential for recovering obliterated serial numbers on firearms. With the primary focus on developing efficient non-destructive techniques, these methods could potentially enhance or replace traditional plans as a standard protocol for serial number restoration in forensics.

2.2 Infrared Thermal Imaging

Infrared thermal imaging is the non-destructive evaluation method with a wide variety of applications in non-destructive testing, medicine, and process monitoring. This technique relies primarily on the intensity of infrared radiation emitted by the surface of the object as a function of temperature [44,45]. The infrared (IR) region of the electromagnetic spectrum lies between 0.75 μm and 1mm. For thermographic measurement, the area is divided into three sub-regions according to atmospheric attenuation. Short-wave infrared (SWIR) lies between 1 μm and 2.5 μm, medium-wave infrared (MWIR) ranges from 3 μm and 5 μm, and long-wave infrared (LWIR) from 8 μm and 12 μm. Atmospheric attenuation prevents an object's total radiation from reaching the camera. If no correction for attenuation is applied, the apparent measured temperature will be lower with increased distance. The correction of atmospheric attenuation is performed at each spectral range using IR camera software. The spectral range of IR camera depends on the type of IR detector; indium gallium arsenide for SWIR, indium antimonide for MWIR, and mercury cadmium telluride for LWIR [30]. Figure 2.5 shows the infrared region for the thermographic measurement [46].

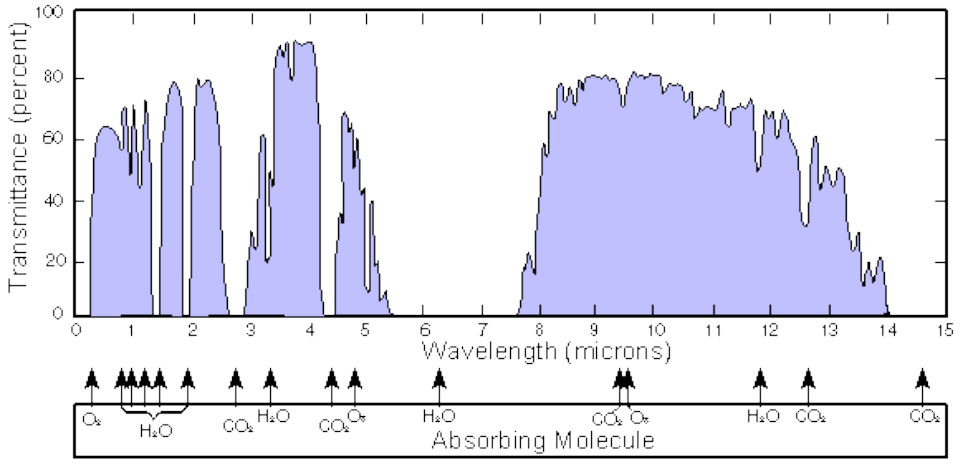

Figure 2-5 Percent transmittance of different infrared wavelength (μm) through the atmosphere [46]

There are two major categories of infrared thermography (IRT) - passive and active. Passive thermography is simply collecting thermal images relying only on the infrared radiation emitted from the surface contributed by the internal thermal energy of the object. Active infrared thermography involves applying external thermal energy into the object, thermal conductivity, recording thermal images in real-time, and understanding the spatial distribution of surface temperature [13,47-49]. These include pulse, transient, and lock-in. Vibration and transient thermography are primarily used for defect detection. Lock-in thermography is used for both defect depth analysis and feature extraction. Lock-in thermography (LIT) is particularly useful for detecting near-surface defects because of its sensitivity to interface between materials, which is similar to a local change in thermal conductivity within defective areas [48-49]. LIT can be applied to develop a new non-destructive method for serial number restoration.

2.2.1 Lock-in Thermography

Lock-in thermography involves generating periodic energy waves at a lock-in period or frequency into the surface of an object under observation. The heat flow, as the thermal wave propagates through the object, will be affected by thermal conductivity differences across the observed surface, so changes in the phase of the stream are experienced. The temperature changes are observed at predetermined lock-in frequency using thermographic images collected over the entire lock-in period at an equal time interval. These images reveal information about changes in the object's thermal conductivity across the surface under observation [49].

According to the lock-in principle, synchronization of the thermographic image sequence and the lock-in frequency is assumed with a fixed number of thermal images per lock-in period and weighing factors on each image. The optimal lock-in correlation among thermal images uses harmonic (sine or cosine) function as a weighting factor to achieve the best signal to noise ratio.

This approach compresses thermal images to generate different kinds of images containing dominant information, which could display the local variation between defective and non-defective areas [50,51]. These developed images have some surface information suppressed, making them less sensitive to uneven heating and local emissivity variations, which are concerns in using other thermal imaging techniques. As a result, LIT is more useful than other thermography techniques. These processed images have better surface temperature signals that are more robust than thermal models for analyzing subsurface components [15,50,51]. Figure 2.6 illustrates step by step process to perform LIT analysis.

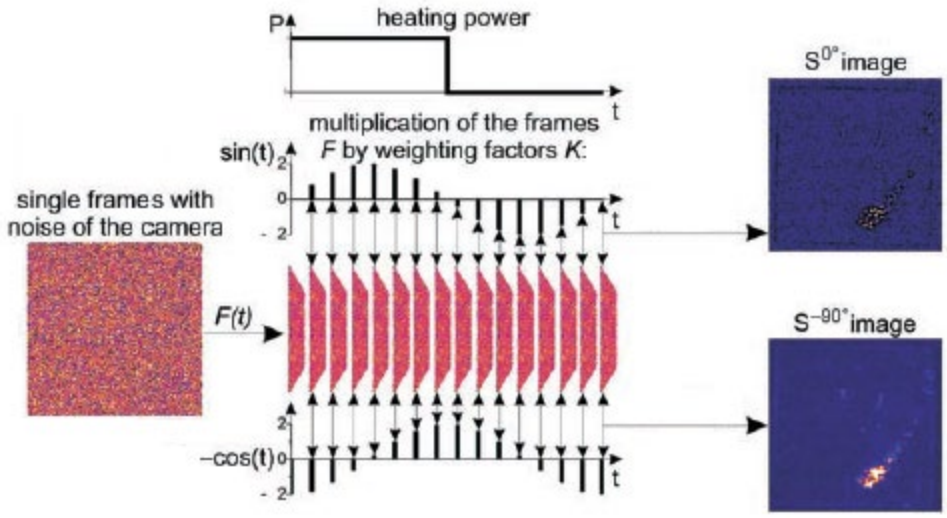

Figure 2-6 Schematic diagram of the lock-in imaging process of a certain lock-in period [15]

A non-sinusoidal thermal energy wave is induced into the surface of a sample. An infrared camera is used to collect thermal images (**F**(*t*)) of the sample surface over the entire lock-in period (t) at equal time intervals. Two-channel lock-in correlation is used to process the thermal images. The correlation method uses two sets of weighting factors resembling sine and -cosine function, respectively, at a complete cycle (360˚). The correlation is performed twice in parallel with these two weighing factors. The first channel measures the signal in phase with the sine function, and the second channel measures the signal in phase with the -cosine function, which is

-90˚ out of phase from the sine function. The in-phase image ($\mathbf{S}^{0^\circ}$) and out-of-phase image ($\mathbf{S}^{-90^\circ}$) is calculated using Equations 2.2, and 2.3 [14].

$$S_{x,y}^{0^\circ} = \frac{1}{n}\sum_{k=1}^{n} 2\sin(t_k) \times F_{x,y}(t_k) \tag{2.2}$$

$$S_{x,y}^{-90^\circ} = \frac{1}{n}\sum_{k=1}^{n} -2\cos(t_k) \times F_{x,y}(t_k) \tag{2.3}$$

$$t_k = \frac{k-1}{n} \times 360^\circ$$

where:

n is the number of thermal images per lock-in period

x,y is the pixel coordinate of the two-dimensional thermal image

$F_{x,y}(t_k)$ is the thermal image pixel value at a specific time

t_k is the relative angle in the time domain

$S_{x,y}^{0^\circ}$ is the in-phase signal (positive or negative) at (*x,y*) pixel coordinates

$S_{x,y}^{-90^\circ}$ is the -90˚ out of phase signal (positive or negative) at (*x,y*) pixel coordinates

A phase independent amplitude image (**A**), and a signal phase shift image (**P**) are then generated using Equations 2.4 and 2.5 [14].

$$A_{x,y} = \sqrt{(S_{x,y}^{0^\circ})^2 + (S_{x,y}^{-90^\circ})^2} \tag{2.4}$$

$$P_{x,y} = \tan^{-1}\left(\frac{-S_{x,y}^{-90^\circ}}{S_{x,y}^{0^\circ}}\right) \text{ (-180 if } S_{x,y}^{0^\circ} \text{ is negative)} \tag{2.5}$$

where:

$A_{x,y}$ is the phase-independent amplitude value at (*x,y*) pixel coordinate

$P_{x,y}$ is the -90˚ phase shift value at (*x,y*) pixel coordinate

A significant drawback of LIT is blind frequencies, i.e., lock-in frequencies at which the contrast between clean and defective areas is minimal. Defect detection in phase images developed at these frequencies is usually unreliable, and thus, such rates need to be avoided. This shortcoming can be addressed by evaluating defect depth analysis, which involves calculating phase images of undefaced stamped serial numbers over several thermal input frequencies.

For serial number restoration, optimization of lock-in frequency contributes to efficient feature extraction. The defaced and non-defaced region has distinct structures that are subject to visual interpretation for identification. However, the visual description is not yet practical due to the low quality of spatial resolution in processed images, likely caused by an insignificant temperature difference.

2.2.2 Image Analysis

For serial number restoration, optimization of lock-in frequency contributes to efficient feature extraction. The defaced and non-defaced region has distinct structures that are subject to visual interpretation for identification. However, the visual description is not yet practical due to the low quality of spatial resolution in processed images caused by an insignificant temperature difference. Even though the resolution is low, image processing techniques enhance the features [52-54].

Univariate image analysis is a method to perform some operations on an image's spatial domain (two- or three-dimensional) to get an enhanced image. Image analysis concentrates mainly on spatial relationships between pixels in a grey level image. This kind of image analysis is generally used for digital image processing. A single-phase or amplitude image processed via lock-in thermography can be treated like a digital image. For serial number identification, two critical components of the image area of interest are where one of the components is associated with the defaced city and the other one with a non-defaced area. Image binarization should better characterize the images obtained from the LIT analysis since there are only two regions of interest for analysis. The process of binarization works by finding a threshold value in the histogram of pixel values – an amount that effectively divides the histogram into two parts, one represents the object, and the other is a background. Image smoothing, segmentation, and morphological operations (dilation or erosion) are used in binary image processing for feature enhancement. These techniques intend to remove background noise from the image, which improves the image quality for a better visual interface.

On the other hand, multivariate image analysis (MIA) is a methodology for analyzing multidimensional images, where the image coordinates are position (pixels of 2-D or 3-D) and

variable number [55,56]. The variables can be time, wavelength, energy, and many others. MIA focuses on the correlation of structure between the variables to provide additional information useful for exploring images and classifying regions in them. A wide range of applications for MIA includes medical imaging, hyperspectral imaging, remote sensing, microscopy, and many more. Principal component analysis (PCA) is the backbone of MIA [55-59], which can be applied with infrared lock-in thermography (LIT) for serial number restoration.

PCA utilizes multiple lock-in parameters, which generates numerous images with distinct features. These conditions could include various temporal phases, amplitude, or thermal images [59] at different lock-in frequencies with or without optimization. The technique is based on the fact that sequential images are highly correlated and often contain almost the same information object pattern in the image. The analysis is used to remove the time-series correlation by identifying the optimal linear combination of original temporal images accounting for the variation of pixel values in an image. Image preprocessing, such as smoothing (box filtering) is still required before carrying out PCA on amplitude or phase images for additional feature extraction. The significant challenges of using PCA with LIT are - determining the optimal number of images to get a consistent result and finding a model that resembles the defaced serial number. Image processing techniques such as binarization, segmentation, and others can also be used on each generated image via multivariate image analysis.

2.3 Pattern Recognition

Pattern recognition is an automatic recognition of an object in the image which involves three primary operations, including representation, feature extraction, and classification. Feature extraction and representation are used to describe an image. The two parts are collaboratively referred to as an image description. Classification is a technique to assign the image to a specific

category (class) from a set of pre-defined types. Image description and classification method are the two entities for consideration to bolster pattern recognition.

The size or location of an object within the image should not matter for pattern recognition since the shape of an object defines the image [60]. Several methods are applied to transform an image into a set of unique descriptive features that represent the picture [61-63]. Different representations are based on several feature extraction techniques, including statistical functions such as zoning, global descriptors such as moments, and geometrical and topological features such as strokes and chain codes [64-66]. The most important properties for a proper feature extraction technique include invariance against some geometric transformations (scale, translation, and rotation), stability to noise, blur, and small local deformations as well as completeness in describing the shape of an object [67,68]. A method that has proven to be very robust in meeting these attributes is moment invariants.

There are several ways to identify the image based on the best image descriptor available. Two major approaches are library (reference) matching and classification. Library matching involves searching every instance within the library and linking independently. The similarity measures determine the strength of the pairing to each case, computational methods of quantifying the similarity between objects. These measures are primarily based on a vector to vector similarity, including correlation coefficient, Euclidean distance, cosine, and cosine. Classification is the method of assigning an object to a category or class (collection of instances). The efficiency of this method depends on intra-class and inter-class variation. The most commonly used classification techniques (classifiers) are PLS-DA, kNN, support vector machine [69], and neural networks [70-72]. Classification with image moment invariants, especially Zernike and Pseudo-Zernike moments, are applied in various fields [73-74].

2.3.1 Moment Invariants

Moment invariants are properties of connected regions in binary images that are invariant to translation, rotation, and scale. Moments are scalar quantities used to characterize a function and capture its significant features. The role of moments has been utilized as pattern features in many applications to achieve invariant recognition of two-dimensional image patterns [75,76]. In image processing, they are measurable quantities insensitive to particular deformations and provide enough discrimination power to distinguish among objects belonging to different classes [77]. Also, moments with orthogonal basis functions, represent an image with a set of mutually independent descriptors, thus minimizing redundancy [16,75-77].

Regular or geometric moments which form the basis for most moment-based feature extraction techniques are defined by Equation 2.6 [16].

$$M_{pq} = \int_{-\infty}^{\infty}\int_{-\infty}^{\infty} x^p y^q F(x,y)dxdy \tag{2.6}$$

where:

(x, y) is the pixel coordinates of an image

F (x, y) is real image intensity, piecewise continuous function

p and q are non-negative integers

For images with discrete pixel locations, the integrals are estimated with summations. These essentially define moments by projecting a function onto a monomial basis set $x^p y^q$. However, this basis set is not orthogonal, and as such, there is some redundancy in the information associated with the moments developed [76,77].

Various types of orthogonal moments have been developed and used in image recognition processes to varying degrees of successes solving redundancy issues [30]. Three classes of orthogonal moment invariants that have proven to extract robust features for the classification of images are LMs, ZMs), and PZMs [31]. LMs are based on Legendre polynomials, whereas ZMs and PZMs rely on radial polynomials. Figure 2.7 shows an example of the image reconstruction ability of these orthogonal moments [16].

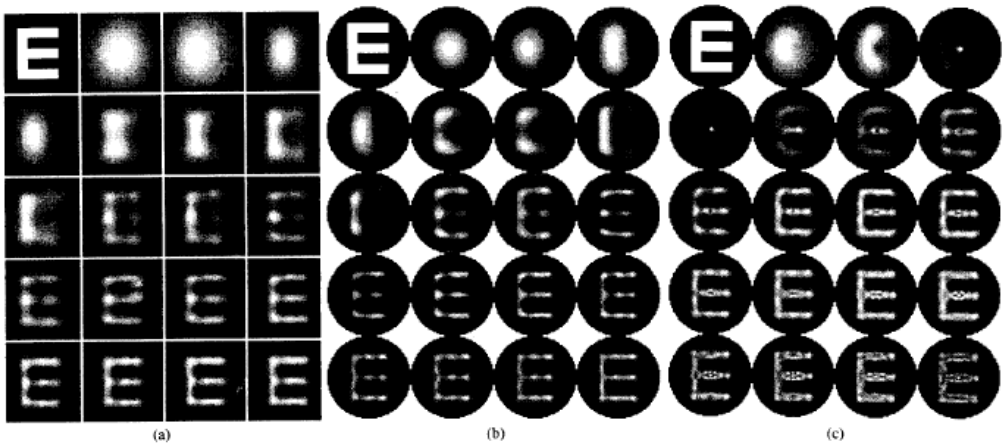

Figure 2-7 Reconstruction of a letter E by a) Legendre moments, b) Zernike moments, and c) Pseudo-Zernike moments; Original Image and reconstructed image using 2nd through 20th order of moments [16]

Most of the image information can be recaptured by using a sufficiently large number of a particular set of image moments (order of the moments). In terms of overall performance, which includes sensitivity to image noise, aspects of information redundancy, and capability for image representation, ZMs and PZMs outperform all other moments. ZMs are the most widely used family of orthogonal moments due to their other property of being invariant to an arbitrary rotation of the object they describe. Even though PZMs are also derived from Zernike polynomials, PZMs are used in many pattern recognition and image processing applications as alternatives to the traditional ZMs. It has been proved that PZM have better feature representation capabilities and are more robust to image noise than ZMs [78].

- **Pseudo-Zernike Moments**

Zernike polynomials were introduced and later derived from the requirement of orthogonality and invariance properties for use in characterizing images [79]. One of the components that form Zernike polynomial is real-valued radial polynomials, and the other part is imaginary. Pseudo-Zernike polynomials differ from Zernike polynomial only on the constraints applied in the radial polynomial. The pseudo-Zernike polynomials form an utterly orthogonal set over the interior of a unit circle and are of the form shown in Equation 2.7 [79].

$$\begin{gathered} Z_n^m(x,y) = Z_n^m(r,\theta) = R_n^m(r)e^{jm\theta} \\ j = \sqrt{-1} \\ r = \sqrt{x^2 + y^2} \\ \theta = \tan^{-1}\left(\frac{y}{x}\right) \end{gathered} \tag{2.7}$$

$$R_n^m(r) = \sum_{k=0}^{n-|m|} \frac{(-1)^k (n-k)! r^{n-2k}}{k!\left(\frac{n+m}{2}-k\right)!\left(\frac{n-m}{2}-k\right)!} \tag{2.8}$$

$$Z_n^m(r,\theta) = R_n^m(r)\cos(m\theta) \text{ for } m \geq 0$$

$$Z_n^m(r,\theta) = R_n^m(r)\sin(m\theta) \text{ for } m < 0$$

where:

n is a number of basis polynomials that define the order of Pseudo-Zernike moments,

m is a positive or negative integer bound by $|m| \leq n$,

Z_n^m is the pseudo-Zernike polynomial,

R_n^m is the real-valued radial polynomial,

r is the length of the vector from the origin to the x, y-coordinates, and

θ is the angle between the vector and the x-axis in the counterclockwise direction.

The PZMs are calculated using Pseudo-Zernike polynomial and the input images, as shown in Equation 2.9.

$$\mathrm{A}_n^m = \frac{n+1}{\pi} \sum_{x,y} F(x,y) \times \mathrm{Z}_n^{m*}(r,\theta) \tag{2.9}$$

where,

A_n^m is the PZM coefficient

$(n+1)^2$ = number of PZM coefficients at n^{th} order of the moment

The PZMs are rotation invariant, and images could be preprocessed to make them scale and translation invariant, thus removing these variables from the image classification problem [78]. Such preprocessing is achieved using affine transformations to map variables (pixel intensity values at a location in the case of images) into new variables (new locations for images) by applying a linear combination of translation and scaling operations [73-80]. The rotational invariance using PZM is shown in Equation 2.10, which is derived by rotating the images with phase angle (α) from Equation 2.9.

$$\beta = \theta + \alpha$$

$$F(r,\beta) = F(r,\theta)$$

$$\mathrm{A}_n^m(\beta) = \frac{n+1}{\pi} \sum_{x,y} F(r,\beta) R_n^m(r) \mathrm{e}^{-jm\beta}$$

$$\mathrm{A}_n^m(\beta) = \mathrm{A}_n^m e^{-jm\alpha}$$

$$\left|\mathrm{A}_n^m(\beta)\right| = \left|\mathrm{A}_n^m\right| \tag{2.10}$$

The rotation of an image does not change the magnitude of the moments with the rotation invariance of pseudo-Zernike moments. Another useful property of pseudo-Zernike moment is the orthogonality of the orders of independent basis polynomials. This orthogonality property makes it possible to determine the quality of features extracted at each request of basis polynomials by reconstructing the images at a particular order [81]. Due to the orthogonality between the order of PZMs, they capture unique features at different moment orders, minimizing information redundancy. These properties make the PZM more suitable as an image descriptor, an exclusive vector representation of an image.

2.3.2 Classification

Classification techniques (classifiers) that involve a comparison of a vector to a spatial domain defined by a class are based on tuning parameters. These standalone classifiers include PLS-DA, kNN, and others. Optimization of the tuning parameter is a necessity for a single method to be a robust classifier. Each classifier utilizes different characteristics to define a class. For example, PLS-DA and kNN rely on different fundamental attributes of a class to classify an image.

PLS-DA is a linear classification method that combines the projection-based regression method, partial least squares (PLS) with the discrimination power of a classification technique [82-83]. PLS finds a linear regression model with a maximum covariance between the dependent and independent variables. The linear regression models are called latent variables (LVs) that are the linear combination of independent variables. Hence, the tuning parameters of PLS-DA are LVs (1,2, 3... full rank), which describes the appropriate sources of data variability. PLS1-DA is applied for one dependent variable ($\mathbf{y}$) and PLS2-DA for multiple independent variables ($\mathbf{Y}$). These response variables are replaced by the set of dummy variables describing the categories

that express the class membership of the statistical units. This constraint does not allow for other response variables than the one for defining the types of images. As a consequence, all independent variables play the same role for the class assignment.

PLS-DA is performed to sharpen the separation between groups of observations, by selecting LVs such that a maximum separation among classes is obtained to understand which tuning parameter carries the class separating information [84]. The efficiency of the method is dataset dependent. Figure 2.8 is an illustration of enlarged separation between two types using PLS-DA for classification at a specific number of LVs [85].

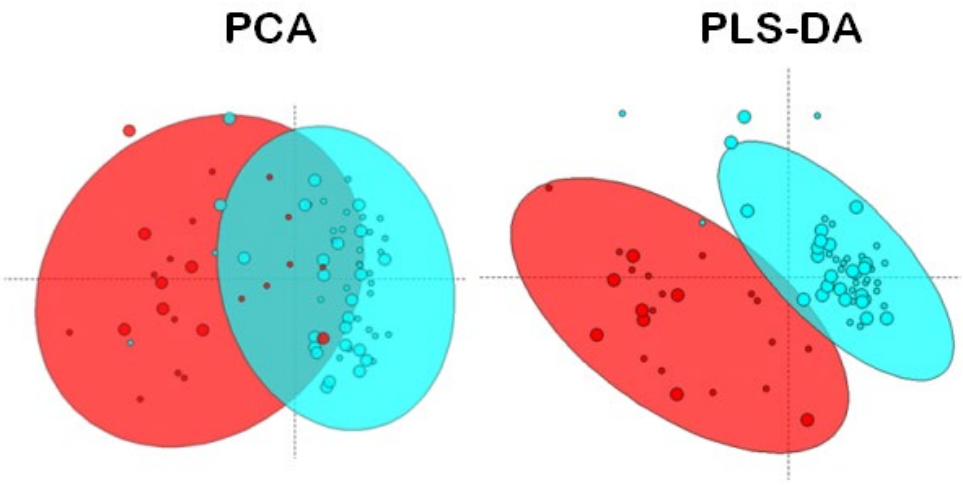

Figure 2-8 Classification using PCA and PLS-DA [85]

The kNN is a non-parametric classification method based on distance measures, such as Manhattan, Chebyshev, and Euclidean distance [86]. An object is classified by a majority vote of its k neighbors, with the purpose assigned to the class most common among its k nearest neighbors [86,87]. Figure 2.9 demonstrates a schematic diagram of the kNN classification [88].

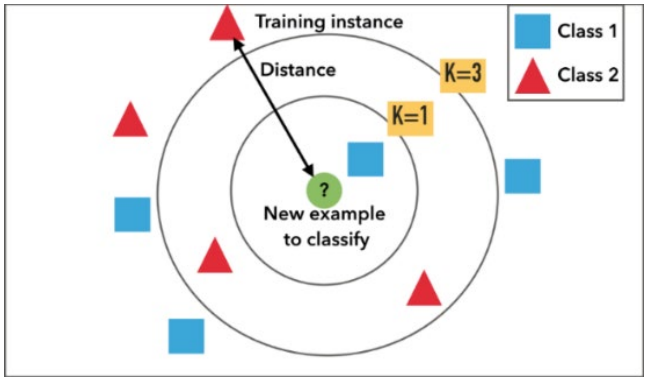

Figure 2-9 An example of kNN classification [88]

The number of neighbors (k) is the parameter used for kNN classification. The distance is measured between the independent variables of each training sample and a new sample. The most commonly used distance measure is the Euclidean distance. It can be observed in Figure 2.9 that depending on the value of k; the object can be classified either way. This problem demands optimization of the tuning parameter.

Additionally, similarity measures such as cosine and Euclidean distance can be used as classifiers to compare a vector to the mean class (vector). No tuning parameters are required. These can be considered as weak classifiers as some of the information associated with a class could be minimized by averaging. As a result, these classifiers are not as reliable to classify an image independently.

There is no consensus on a single classification method and how to optimize it. Hence, several ensembles (fusion) approaches have been developed to avoid method selection. Fusion tends to strengthen the classification compared to a single classifier since the outcome is based

on diverse information provided by multiple classifiers [89,90]. There are three approaches to fuse classifiers. One of the strategies uses a separate algorithm such as random forests and other bagging processes to come up with a set of classifiers. The purpose of this approach to combine weak classifiers to form reliable classifiers. This fusion method still requires method selection and optimization of the tuning parameter. The second approach is to combine optimized classifiers, which is more efficient, as this fusion strategy avoids choosing a single method for classification. However, this still requires picking a set of classifiers and the best single tuning parameter for each classifier. The third approach is to ensemble non-optimized classifiers with tuning parameter window. Rather than selecting an individual tuning parameter, windows of tuning parameters are used. For example, with PLS-DA, the LVs are 1,2,3…, p where p is the total number of LVs used, and windows of LVs are 1,1-2, 1-3, 1-4…,1-p. This approach makes it possible to avoid both method and tuning parameter selection for robust classification.

Chapter 3

3.0 Lock-in Procedure

The methodology for this study was designed to acquire useful thermal imaging data based on the lock-in principle. A different set of samples are tested to validate the application of infrared lock-in thermography (LIT) for serial number restoration. The procedure is carried out in three main stages as outlined below:

1. Sample – acquisition, and preparation
2. Equipment setup
3. Analysis of lock-in thermography (LIT)

3.1 Sample

A set of samples were used in this study to develop a feature extraction process of the defaced serial number. These test samples include a metal plate, a needle holder, and a gun barrel.

3.1.1 Acquisition

The experimental process was mostly developed by testing on a stainless-steel plate (72 mm × 25 mm) stamped with several numbers. This sample obtained as a test piece from Precision Forensic Testing [91], was stamped using an open back inclinable (OBI) press. The numbers were stamped to depths of approximately 0.17mm, 0.15mm, 0.15mm, 0.16mm, and 0.18mm for the 2,6,2,5 and 0 respectively, as measured using a profilometer. Initially, 6.35 mm thick, the stamped numbers were defaced in a controlled manner. A uniform thickness of 0.16mm was mechanically shaved off the top surface, leaving the numbers barely visible. Each number except the first was then progressively shaved off to a depth 0.03 mm beyond the previous. The first number on the plate is left visible to serve as a control, ensuring consistent knowledge of the

positions of the defaced numbers. Figures 3.1 and 3.2 show the original and damaged sample, respectively [1].

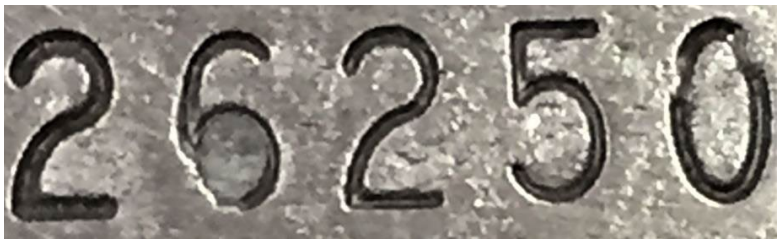

Figure 3-1 Stamped Serial Number (2,6,2,5, and 0) on Stainless Steel plate with depth of 0.17mm, 0.15mm, 0.15 mm, 0.16 mm and 0.18mm respectively [1]

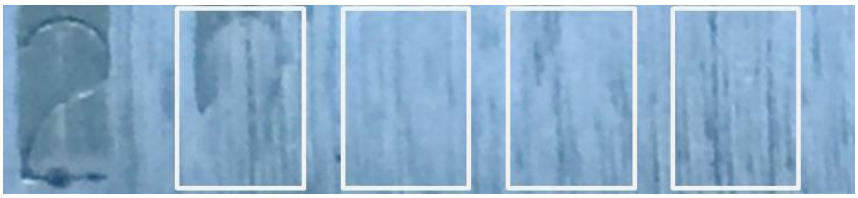

Figure 3-2 Non-defaced two, partly defaced six, and completely defaced two, five and zero [1]

Another sample acquired and defaced is a gun barrel for a Stevens Model 95 12-gauge shotgun. The shotgun had no serial number, and so some numbers stamped on the barrel were defaced using a common filing technique to simulate the serial number defacing. Two numbers (1 and 2) were damaged on the barrel surface and used to test the recovery process. Figures 3.4 and 3.5 show the barrel's images before and after defacing with the red box, indicating the numbers removed.

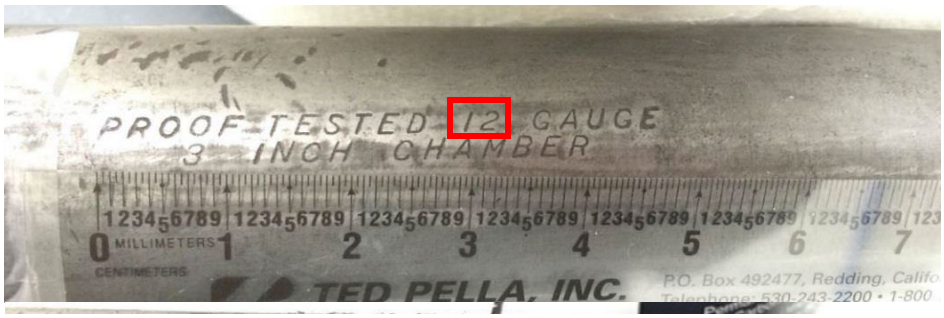

Figure 3.3 Stamped numbers (1 and 2) on a gun barrel [1]

Figure 3.4 Defaced stamped numbers (1 and 2) on a gun barrel [1]

A laser engraved surgical needle holder (Model BM034R) was obtained. This sample is used to test the efficacy of the method on laser engraved samples. Numbers 0,3, and 4 and a letter R were filed to simulate defacing serial numbers. Figures 3.5 and 3.6 show the needle holder before and after some part of the serial number was damaged.

Figure 3.5 Laser engraved serial number (BM034R) on a surgical needle handler [1]

Figure 3.6 Defacing 0,3,4 and R of a laser engraved serial number on a surgical needle handler [1]

3.1.2 Preparation

The surface areas around the defaced numbers on all the acquired samples were polished with ~600-1500 grit sandpaper to ensure a smooth surface for homogeneous distribution of thermal emissivity. The polished surfaces were then thoroughly cleaned with ethanol to remove any extraneous material from the metal surface's smoothing process. The polished surfaces were then covered with a black vinyl electric tape (thickness of 0.18 mm and thermal emissivity ~0.95) to reduce surface emissivity differences.

3.2 Experiment Setup

3.2.1 Equipment

- **Infrared (IR) Camera**

A FLIR SC6700, Science-Grade MWIR InSb Infrared Camera, along with the software, is used to collect thermal images for the experiments performed for this thesis. The computer with FLIR software is connected to the IR camera via an Ethernet cable for the operation of control variables and store thermal images. The specifications for the camera are shown in Table 3-1.

Table 3-1 System Overview of FLIR SC6700

Detector Type	Indium Antimonide (InSb)
Spectral Range	3.0- 5.0 µm or 1.0- 5.0 µm
Resolution	640 × 512
Detector Pitch	15 µm
Standard Temperature Range	-20 ˚C to 350 ˚C
Operating Temperature Range for Lens	-40˚C to 50 ˚C

- **Laser**

A 5W Ar-ion CW laser, from Coherent inc., was used as the primary thermal excitation source for all samples tested. The laser was operated in all-lines mode (351.1 nm, 363.8 nm, 454.6 nm, 457.9 nm, 465.8 nm, 476.5 nm, 488.0 nm, 496.5 nm, 501.7 nm, 514.5 nm, and 528.7 nm) to maximize the amount of power reaching the sample. The laser was generally set to produce 2.5-2.75 W of thermal energy, allowing approximately 1.2-1.5W of thermal energy to reach the sample after going through the prisms used to direct the beam and the top hat filter, which converted the Gaussian profile of the laser beam to a square pattern.

- **Function Generator**

An FY 6900 Dual-channel Arbitrary Waveform Signal Generator is used as a function generator. The function generator is used to generate a non-sinusoidal periodic waveform (square) with frequencies ranging from 0.01~100 MHz at two channels. Also, the device is used to synchronize the laser pulsing frequencies with the frame rate of the camera, as well as act as an external device.

- **Shutter**

A Uniblitz mechanical shutter was used to pulse the laser energy to the sample under study. It is synchronized to the square waveform frequency generated by the function generator.

3.3 Setup

The LIT analysis system involves guiding the thermal energy from a heat source via a pulse generator onto the sample surface and collecting the infrared radiation emitted from the sample surface. In the previously developed method, the significant components of the experiment were an infrared camera, a function generator, and two thermal energy sources [1]. One source is the laser used to perform lock-in thermography. The other source is a hot plate

where the sample is placed. This setup allows the experiment to be carried out at a higher sample temperature. As shown in Figure 3.3, the new experimental setup has an IR camera, a function generator, and a single thermal energy source, i.e., laser, allowing the experiment to be carried out at room temperature.

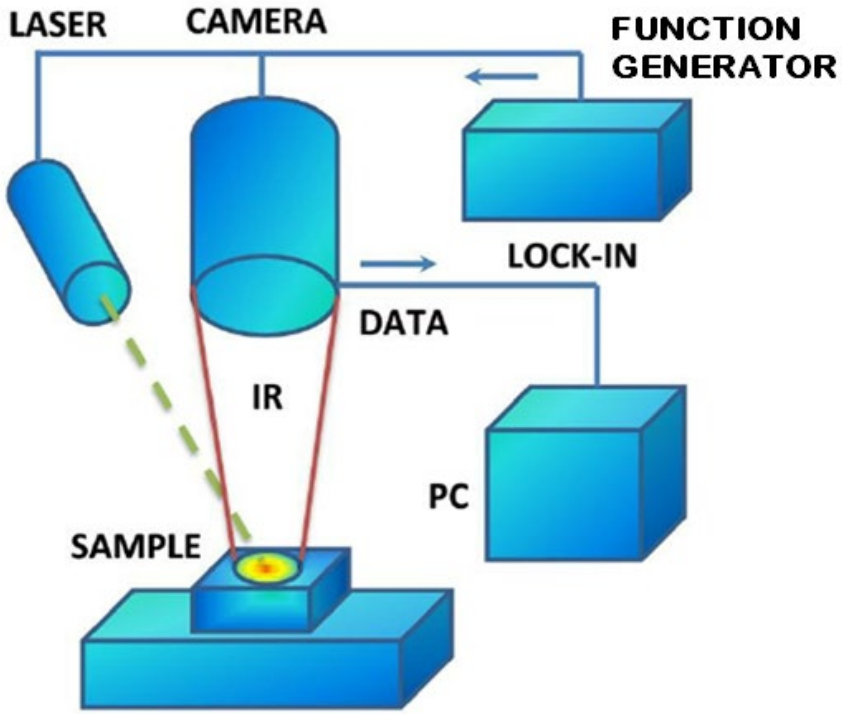

Figure 3-3 Schematic diagram of the experimental setup for infrared lock-in thermography (LIT) [15]

The primary heat source, a 5W Ar-ion CW laser, operating in all-lines mode, is chopped with a Uniblitz mechanical shutter to apply pulsed energy to the samples. The laser was controlled to generate 2.5-2.75W of thermal energy. However, losses through the top-hat filter transform the Gaussian shape into a square-shape profile to ensure that the intensity profile of the beam is constant across the surface area under observation. Reflection losses from the optical prisms result in only about half of the power reaching the sample. Thus approximately 1.2-1.5W of laser light hit the sample. This amount of laser power gave a decent amount of temperature

variation over the lock-in period while avoiding overheating the electric tape. This phenomenon provides the ability to capture the temporal thermal gradient of the plastic deformation zone.

The control variables of the FLIR SC6700 IR camera are adjusted for the measurements using the FLIR software. The settings in the software were specified based on the research design. Table 3-2 illustrates the specifications of control variables in FLIR software used for this experiment.

Table 3-2 Fixed settings of control variables in the FLIR software

CONTROL VARIABLES	**SETTINGS**
Sequencing	Preset
Temperature Calibration Range	10˚C to 90˚C
Dwell	No. of frames (thermal images)
Integration	≥ Frame rate
Sync Source	External
Sync Polarity	High
Trigger Source	External
Trigger Polarity	Low

As mentioned previously, an FY 6900 dual-channel signal generator is an external device used to regulate the thermal energy from the laser and thermal imaging using an IR camera simultaneously. One of the channels (channel 1) is used to control the pulsation of a shutter for controlled operation of the energy supply from the laser, ensuring that the thermal energy from is delivered to the sample in a non-sinusoidal pattern. The other channel (channel 2) is connected to the FLIR SC6700 IR camera as a sync source as well as a trigger device. The function generator

synchronizes the laser pulses with the IR camera's control variables, ensuring a fixed rate of recording thermal images over an entire period of pulsation regardless of the lock-in frequency used in pulsing the thermal energy be achieved. Channel 2 is used as a manual trigger to collect thermal images of the sample surface as the pulsed thermal energy propagates through the sample. The experiment is conducted at room temperature (~20˚C to 25˚C). The temperature distribution on the surface is monitored using the infrared camera to collect thermal imaging data over the lock-in period.

For the samples with stamped or laser engraved numbers (defaced or non-defaced), the setup is adjusted with the camera field of view narrowed to capture areas over two of the removed stamped number. The adjustment is made to enhance the detail captured with more pixels per millimeter and to ensure an even spread of the pulsed thermal energy from the laser beam to avoid possible lateral thermal gradients. The collected images are then digitally split to have datasets focused on the areas around each removed number.

During the experiments, thermal energy is pulsed into the surface of the sample (covered with black vinyl electric tape) under observation using the laser at a defined lock-in frequency. Data was collected at several rates independently and used to generate phase and amplitude images for the undefaced number on the stainless-steel plate. This variation was used to determine an optimal range of lock-in frequencies, and avoid the blind frequencies. These optimal frequencies should adequately characterize the change in a thermal gradient within the stamped area and non-stamped areas on the metal surface. The thermal images for defaced serial numbers are collected at the determined range of lock-in frequencies.

3.4 Lock-in Thermography Analysis

An in-depth analysis of lock-in thermography was performed by testing on undefaced stamped number 2 and partially defaced six on a stainless-steel test sample. The black vinyl electrical tape was placed on the surface to cover to minimize enormous differences in thermal emissivity for accurate measurement of the surface temperature. Figure 3.4 shows the improvement in thermal emissivity difference for precise measurement of apparent surface temperature.

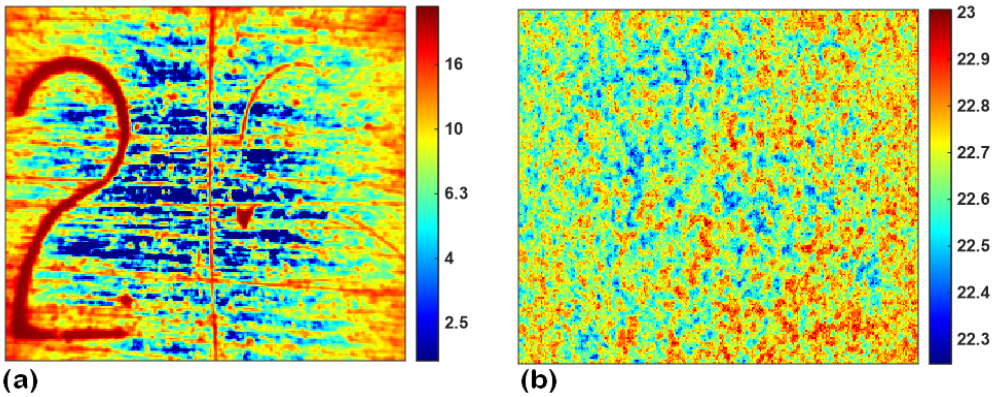

Figure 3-4 Thermal imaging with no external heating of stamped serial numbers, 2 (non-defaced) and 6 (partially defaced), on a stainless steel: a) without a black electric tape and b) black electric tape on the surface

Since the numbers are not visible in the thermal image as well, undefaced two and partially defaced six are considered equivalent where numbers now have the same surface features and different subsurface features. This condition is ideal for controlled testing for defaced serial number restoration.

The test sample is then placed underneath the IR camera at room temperature. The non-sinusoidal (square) thermal excitation (heating and cooling for each half of the lock-in period) is performed by targeting laser pulse to the surface. The temporal thermal images (frames) are collected at an equal time interval with varying lock-in frequencies to analyze the optimal lock-in frequency for feature extraction. The fixed number of frames (thermal images) per lock-in cycle

– 8 frames per cycle, are recorded for uniformity. Four thermal images are recorded when the laser is on and the other four images when the laser is off at each period. The variation of lock-in frequencies and the frame rate for each lock-in period is presented in Table 3-3.

Table 3-3 Tabulation of Lock-in frequencies and the respective frame rate

Lock-In Frequency (Hz)	**Frame Rate (Hz)**
0.0125	1
0.25	2
0.5	4
1	8
2	16
4	32
8	64

The thermal images for undefaced two and partially defaced six are collected and processed based on the lock-in principle. For feature extraction of the stamped numbers, phase shift (P) and amplitude (A) images are computed at all the lock-in frequencies mentioned in Table 3-3. Figures 3.5 and 3.6 show the features of thermal, phase, and amplitude images at different lock-in frequencies for undefaced two and partially defaced six, respectively.

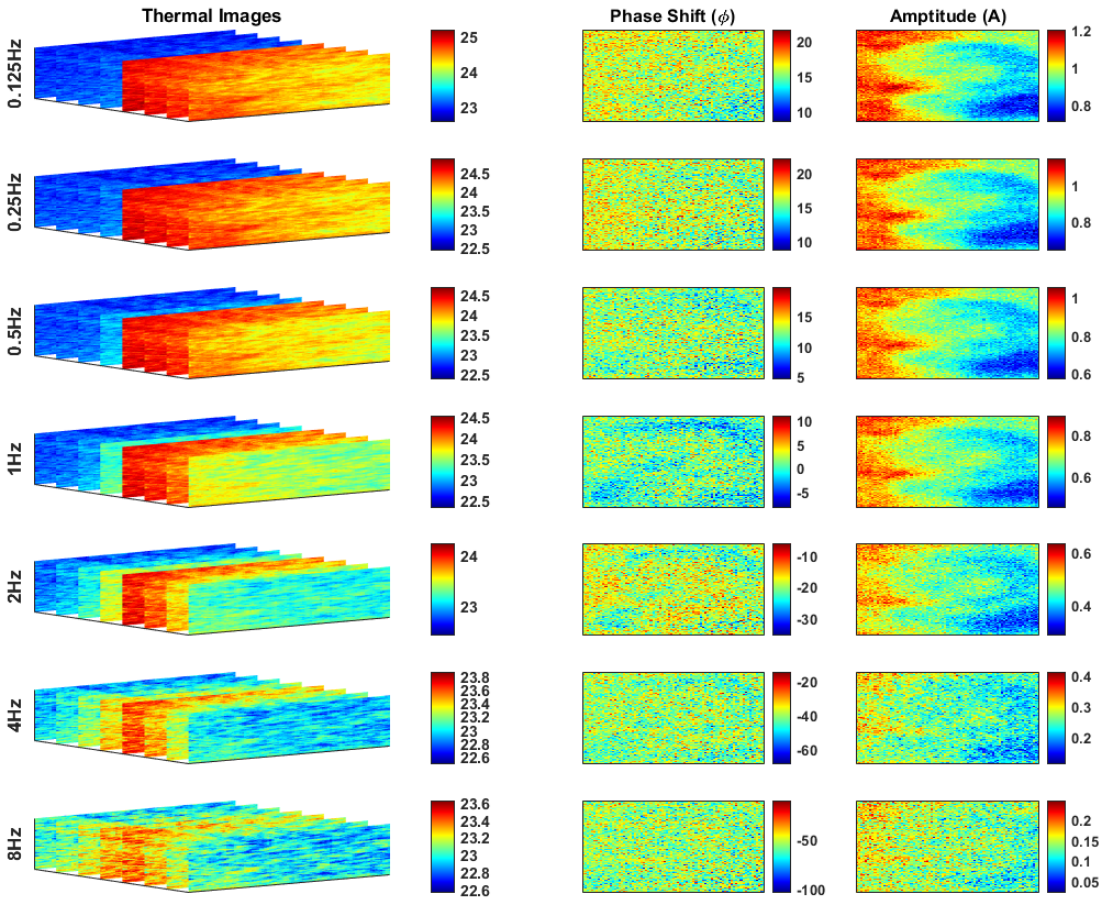

Figure 3-5 Thermal images (3-dimensional), phase shift (ϕ) and amplitude (A) images for undefaced 2 at each 7 different lock-in frequencies (0.125, 0.25, 0.5, 1, 2 ,4 and 8Hz)

As the lock-in frequency increases, the change in temperature decreases. At 8Hz, the temperature change is approximately 1˚C, whereas the lock-in frequency of 0.125 has a variation of about 2.5˚C. The amplitude image of amplitude extract features from the surface or close is hugely affected by the occurrence of a temperature gradient observed in thermal images. The temperature gradient is caused mainly by the uneven distribution of laser power across the sample surface, some variation in surface emissivity, and IR camera's field of view. However, the temperature gradient does not hurt the phase images as the feature extracted is underneath the surface. The lock-in frequency defines the depth of subsurface that is being analyzed. The phase image at 1Hz seems to extract the features of number 2, which can be observed visually.

Frequency of 0.5 and 2Hz also have some features, but not entirely clear, as seen in 1Hz. The lock-in frequency analysis for undefaced 2 indicates that the optimal rate would be close to 1 Hz, which could vary from 0.5 to 2 Hz. For more verification, a similar analysis to optimize the range of lock-in frequency is carried out on partially defaced 6, as shown in Figure 3.6.

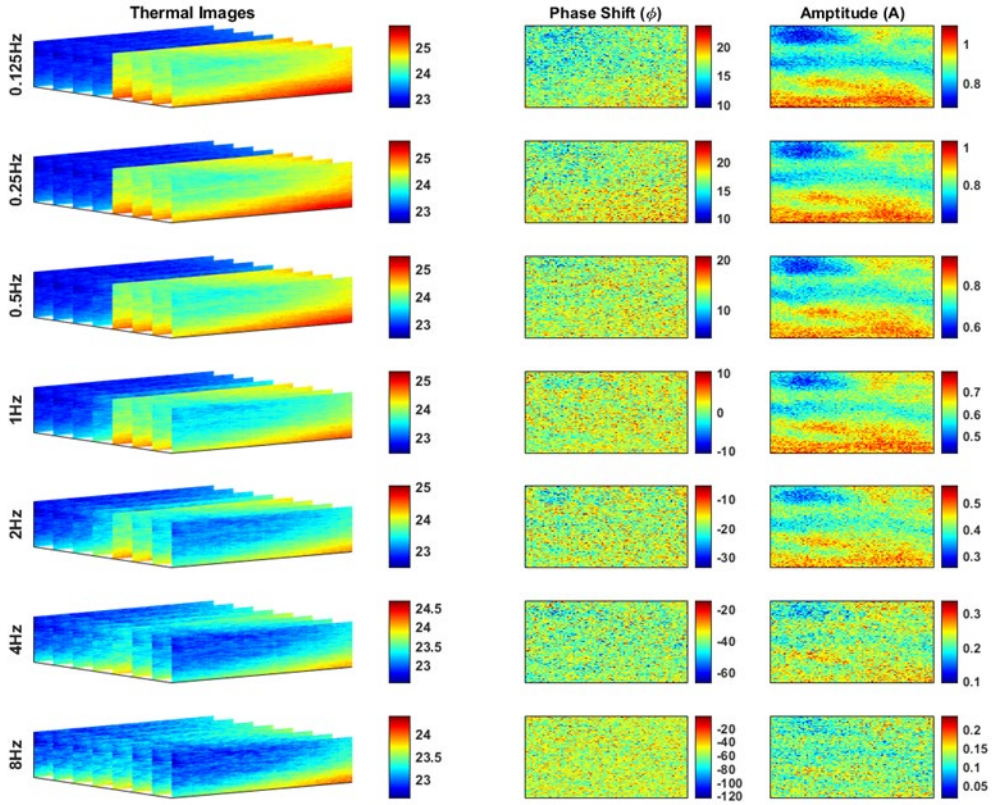

Figure 3-6 Thermal images (3-dimensional), phase shift (ϕ) and amplitude (A) images for partially defaced six at each 7 different lock-in frequencies (0.125, 0.25, 0.5, 1, 2 ,4 and 8Hz)

In this experiment, the amplitude is also slightly affected by the temperature gradient as a similar trend between amplitude and thermal images is observed in Figure 3-6. Phase image seems to be the choice based on previous analysis. However, the spatial resolution of the phase image is not good enough for visual interpretation, since the number is partially defaced. The pattern cannot be clearly defined by either lower or higher phase shift values. As a result,

determining the range of optimal frequency based on a visual understanding of phase images is not possible. Further image analysis on the defaced serial number may show the efficacy of the range of optimal frequency proposed based on a single visual review of phase images associated with undefaced two, which is treated as a defaced serial number for testing. The same experimental design is used to collect thermal images and compute phase images for the rest of the defaced number from all test samples.

3.5 Image Enhancement

The image analysis efficiency is tested with phase images obtained for each of the serial numbers engraved on the stainless-steel plate. The region of interest used in image analysis is expected to be the exact location of each serial number's stamped area. The undefaced two and partly defaced six were used as a cross-reference to locate the approximate section of phase image, which resembles the plastic stain pattern of each serial number. The visual interpretation of phase image associated with undefaced 2 suggests that the small phase values define the features that resemble the stamped region and higher values to be non-stamped areas within the image.

The phase images are converted to binary images using a threshold value. The phase values can be positive or negative. For data transformation, these values are scaled to a fifth power where the positive and negative directionality is still preserved. This transformation is performed to maximize the separation between low and high values so that the distribution is close to being bimodal. The proposed idea behind the change is to improve the thresholding, which, in turn, helps minimize background noise. An additional step of normalizing the transformed data to a maximum or minimum value ranging from 0 through 1 is performed to be

consistent with further image processing. The normalized value, close to 0, is now the representative of a non-stamped region, and large amounts, close to 1, represent stamped regions.

For binarization, the threshold value is set to be 75th percentile of the pixel values. The value higher than the threshold is called a foreground pixel (1) and less than or equal to limit as background (0). To further improve the quality of the binary image, the image is processed with a smoothing technique called box filtering to reduce background noise. Box filtering involves each pixel value being substituted with the average weight of pixels within the box (17 by 17 pixels) centered on that pixel—image smoothing results in no binarization. Re-binarization of the processed image is done with the threshold of the 50th percentile.

Image segmentation is applied to simplify the representation of an image into more meaningful images, which is easier to analyze. Image segmentation is the process of partitioning a binary image into multiple segments. For this process, the pixel area with less than the area of box size used for image smoothing is removed so that the unconnected small pixel area does not affect the overall object pattern in an image.

The image analysis is performed on phase image obtained from lock-in thermography for recovery of every defaced serial number used for testing. The phase image for an original and a replicate, was evaluated to recover the undefaced number two and partially defaced six. The location of the phase image that contains the defaced number is assumed based on a visual inspection of enhanced binary images obtained via image analysis. The size (height and width) of the phase image region containing the defaced number is tuned with image analysis until the approximate representation of a number or letter pattern is achieved. The decision making for approximation is made based on visual inspection of the multiple enhanced binary images

obtained using different image sizes and moving locations (left to right or top to bottom) about the assumed location.

The phase image replicates are obtained for the undefaced 2 and partially defaced 6 at the optimal lock-in frequency for verification of feature extraction via LIT. The replicates are different from one another on two settings; a new set of black electric tape is placed on the metal surface and positioning of the defaced area changes within the region where the laser hits on the surface for external heat. The experimental setup, laser power and lock-in frequency are same across replicates. The room temperature may vary from ~20˚C to 25˚C depending on the time when the experiment is carried out. The image enhancement techniques are applied to phase replicates. Small adjustment had to be made for similar outcome. Figure 3-7 shows the binary image developed from the phase shift in the presumed location of the stamped number on a stainless-steel plate.

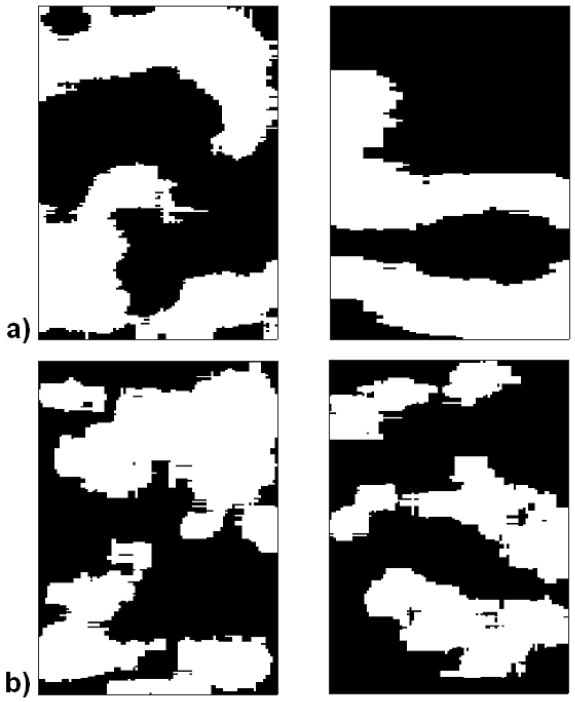

Figure 3-7 Binary image processed from phase shift at optimal lock-in frequency (1Hz) for undefaced two (left) and partly defaced six (right) with two trials:
a) Original, b) Replicate.

These binary images are the representation of the pre-defined location on the stainless-steel plate that is assumed to have the features of plastic deformation zones underneath the surface. The visualization of the profile associated with a binary image's foreground pixels helps to identify the defaced serial number. Each binary image seems to fairly represent the pattern related to every stamped serial number on the stainless-steel plate. The model for a recovered undefaced number is slightly more apparent than a partly and completely defaced serial number. However, this approach is likely to be biased due to prior knowledge of the stamped serial number. If the damaged serial number were a real unknown, some of the patterns could be interpreted differently, resulting in varying identification. For unbiased identification of features present in the binary image, ACIP, develop using a pattern recognition technique, is used. Figure 3.8 illustrates the complete flowchart of phase image processing for feature enhancement.

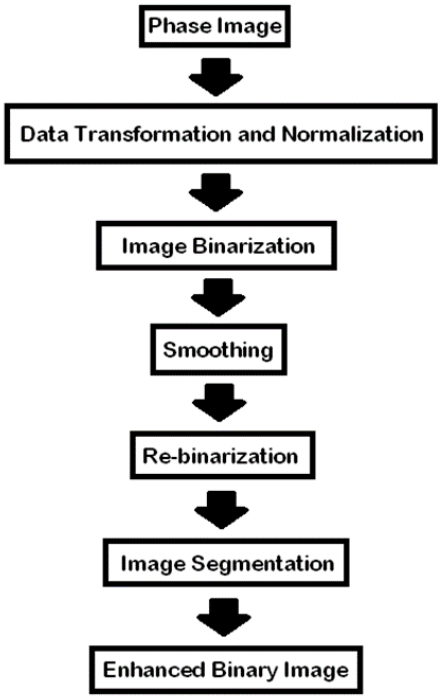

Figure 3-8 Flow chart of Phase Image Analysis

CHAPTER 4

4.0 ACIP

The MATLAB code is written for the protocol. The programming code uses Statistical and Machine Learning Toolbox and Image Processing Toolbox present in MATLAB software.

4.1 Image Description

The first stage of ACIP is to describe images distinctly. Figure 4.1 illustrates the procedure to describe every binary image in the reference database and the phase binary image.

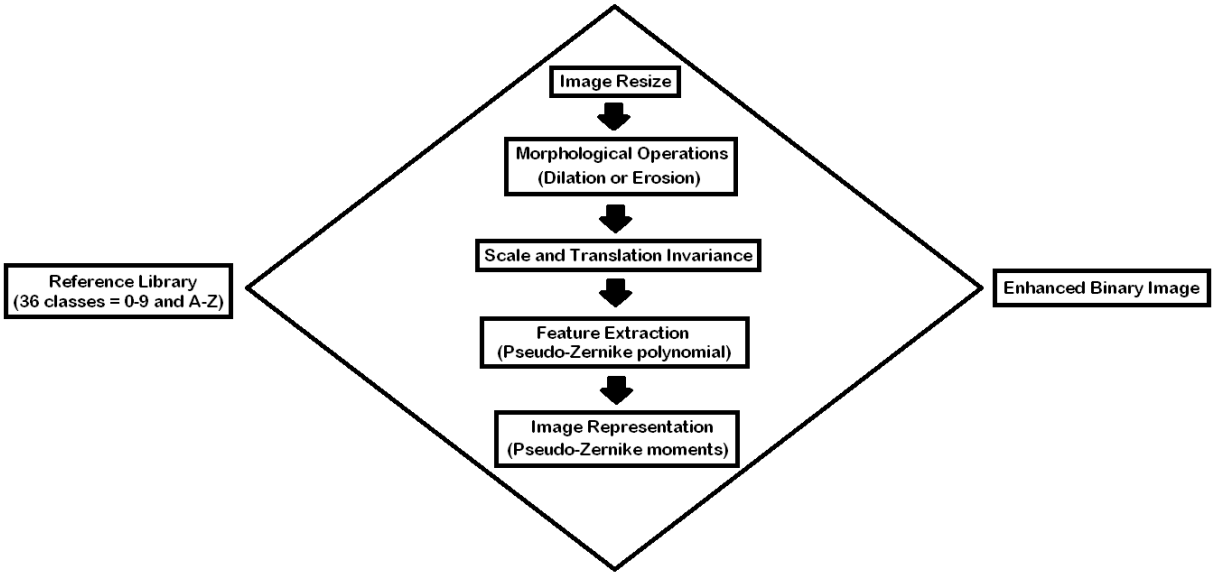

Figure 4-1 Schematic diagram for image description process for reference and phase binary images

The system is divided into five sub-stages: image resizing, morphological operations, scale, translation invariance, feature extraction, and image representation. The first three are used for pre-processing the binary image for normalization among both databases (reference and unknown). The fourth is very crucial, which evaluates Pseudo-Zernike polynomials for a basis set to extract features of an image. The fifth step utilizes a set of moments derived from the basis

set of pseudo-Zernike polynomials for an accurate and unique vector representation of the image [1-3].

The phase and reference binary images (x × y pixels) are resized to a fixed dimension (200 × 100) for consistency across all images. The variation of morphological operations was analyzed for suitable applicability to enhance classification. The boundary of the object pattern in the binary image is enlarged using dilation and reduced with erosion. With dilation, additional features are added to the boundary of the object, and with erosion, the existing feature at the object boundary is removed. The morphological operations, such as dilation and erosion, are applied to the enhanced binary image to form an image with desired object proportion. Three different proportion, 35%, 50%, and 65%, are chosen based on their ability to retain the original pattern of the image with minimal variation consistently, as shown in Figure 4-2.

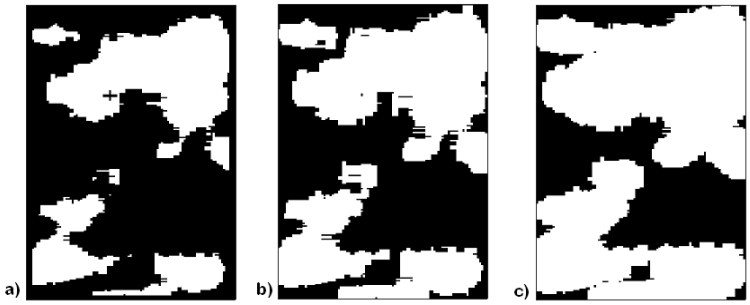

Figure 4-2 An example of morphological operations performed on binary image converged to different object area percentage a) 35% b) 50% and c) 65%

Mapping the image residing in a unit circle with the origin at the center of the image is required to evaluate the Pseudo-Zernike moments. Pixels outside a unit circle are not used in computing the moments. Thus, to ensure that all phases and library image pixels are captured within the unit circle, each binary image is placed into the square image of dimensions calculated, as shown in Equation 4.1.

$$N_x = N_y = 2\sqrt{n_x^{\,2} + n_y^{\,2}} \tag{4.1}$$

where:

n_x and n_y are respectively one half of the number of x and y pixels in the image, and

N_x and N_y are the new dimensions of the resized image.

Scale invariance is achieved by altering the object size such that its area (pixel count for binary images) is set to a predetermined value (β). This value (β) resizes the object in the image, either increasing its size or reducing it from its original area and needs to be determined empirically to ensure that the entire object still lies within the image and is large enough to be discernable without losing any information from the original image. For all image objects in this analysis, the β value is set to 5000 pixels, which makes the object within the inscribed unit circle with an image size that is being used. Even though the pre-selected β value is fixed, the scale invariance technique is only able to scale the object with approximation. The number of object pixels with scale invariance is close to the fixed β value (slightly higher or lower). The scale invariance is achieved by Equations 4.2 and 4.3.

$$g(x, y) = f\left(\frac{x}{a}, \frac{y}{a}\right) \tag{4.2}$$

$$a = \sqrt{\frac{\beta}{m00}} \tag{4.3}$$

where:

(x, y) are the pixel coordinates of each pixel in the image,

m00 is the area (pixel count for binary image), and

$g(x, y)$ is the invariant image pixel coordinates.

Translation involves moving the center of mass of the object in the image to the center of the image. The invariance is achieved, as shown in Equation 4.4.

$$h(x, y) = g(x + \overline{x}, y + \overline{y}) \tag{4.4}$$

where:

h(x, y) is the translation-invariant image pixel coordinates, and

($\bar{x}$, $\bar{y}$) is the centroid of the object in the binary image.

The dependency of scale and translation invariance on an object's proportion was analyzed for accurate image representation. Even though the images are scale and translation invariant, variation in the object's proportion controls the spatial domain of the pattern in a unit circle, as shown in Figure 4-3.

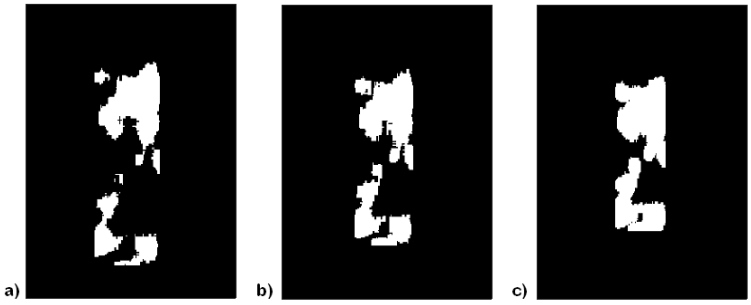

Figure 4-3 Scale and Translation invariant object in a unit circle with three different object's proportions: a) 35% b) 50% and c) 65%

PZMs are moment based overall shape descriptors which compute features by considering the entire image as a whole and represent the total aspects of the image. The polar coordinates with radius r and angle θ for any pixel (x, y) are calculated using equations 4.5 and 4.6 [75,76].

$$r = \sqrt{\left(\frac{x-\bar{x}}{d}\right)^2 + \left(\frac{y-\bar{y}}{d}\right)^2} \tag{4.5}$$

$$\theta = \tan^{-1}\left(\frac{x-\bar{x}}{y-\bar{y}}\right) \tag{4.6}$$

where:

(x, y) is the pixel coordinates of each pixel,

$(\bar{x}, \bar{y})$ is the pixel coordinates of the center of the image, and

d is half the length of the square-shaped image.

Equations 4.5 and 4.6 maps each pixel coordinates to the unit circle in polar coordinates. The radial polynomials $(\mathrm{R}_n^m(r))$ necessary for the determination of the Pseudo-Zernike basis polynomials are calculated using the radius r and defined order n as shown in Equation 4.7.

$$\mathrm{R}_n^m(r) = \sum_{k=0}^{n-|m|} \frac{(-1)^k (n-k)! r^{n-2k}}{k! \left(\frac{n+m}{2}-k\right)! \left(\frac{n-m}{2}-k\right)!} \tag{4.7}$$

where:

n is the order of pseudo-Zernike moments, and

m is a positive or negative integer bound by $|m| \leq n$.

The Pseudo-Zernike basis functions (polynomials) and the corresponding moments are determined from these real-valued radial polynomials, complex function, and the input images using Equations 4.8 and 4.9.

$$Z_n^m(x,y) = Z_n^m(r,\theta) = \mathrm{R}_n^m(r) e^{jm\theta} \tag{4.8}$$

$$\mathrm{A}_n^m = \frac{n+1}{\pi} \sum_{x,y} f(x,y) \times Z_n^{m*}(r,\theta) \tag{4.9}$$

where:

Z_n^m is the Pseudo-Zernike polynomial,

j is imaginary

A_n^m is the Pseudo-Zernike moment, and

f(x, y) is the intensity value of an image pixel with coordinates x, y.

The pseudo-Zernike moment vectors are developed by concatenating the pseudo-Zernike moments (A_n^m) at each order into a single vector. An image pixel can be recreated using the

pseudo-Zernike basis polynomial and the pseudo-Zernike moments up to a defined order, as shown in Equation 4.10.

$$\hat{f}(x,y) = \sum_{n}\sum_{m} \mathrm{A}_{n}^{m}\mathrm{Z}_{n}^{m}(r,\theta) \tag{4.10}$$

where:

$\hat{f}(x,y)$ is a reconstructed pixel in the translated (centered) representation

$(n+1)^2$ defines the number of moments or polynomials used at n^{th} order PZM for reconstruction

The image's reconstruction ability is used to determine the fixed number of moments for a precise and unique vector representation to describe the image. The reconstructed image is used as a foundation to determine fixed order PZM (number of moments) for image representation. Figure 4-4 shows an example of image representation using different order PZM.

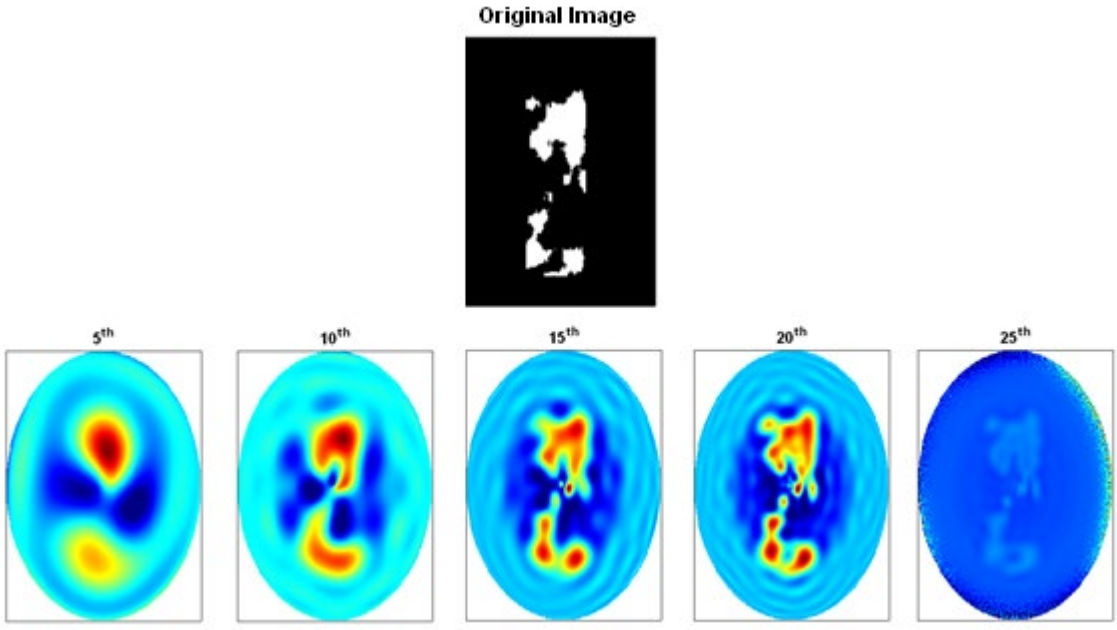

Figure 4-4 Undefaced two (35%) original enhanced binary image and their reconstructed image using fifth-order PZM through 20$^{\text{th}}$ order PZM

It can be observed that the pseudo-Zernike polynomial starts to gradually capture pieces of full-length features with incremental order until the complete information is captured. However, there

is a limit on the number of moments to be used. At higher order, the polynomial is very sensitive to image noise. At twenty fifth order PZM, there is significant noise in the reconstructed image. Hence, based on this analysis, the twentieth order PZM seems to be the best for an accurate image representation with full features and minimal noise.

The PZM incorporates rotational invariance, meaning the rotation of the object does not affect the moments. However, the image can also be constructed using radial moments (RM) from the radial polynomials, which do not have the property of rotational invariance. Figure 4-5 shows two distinct characteristics of PZM and RM representative vectors.

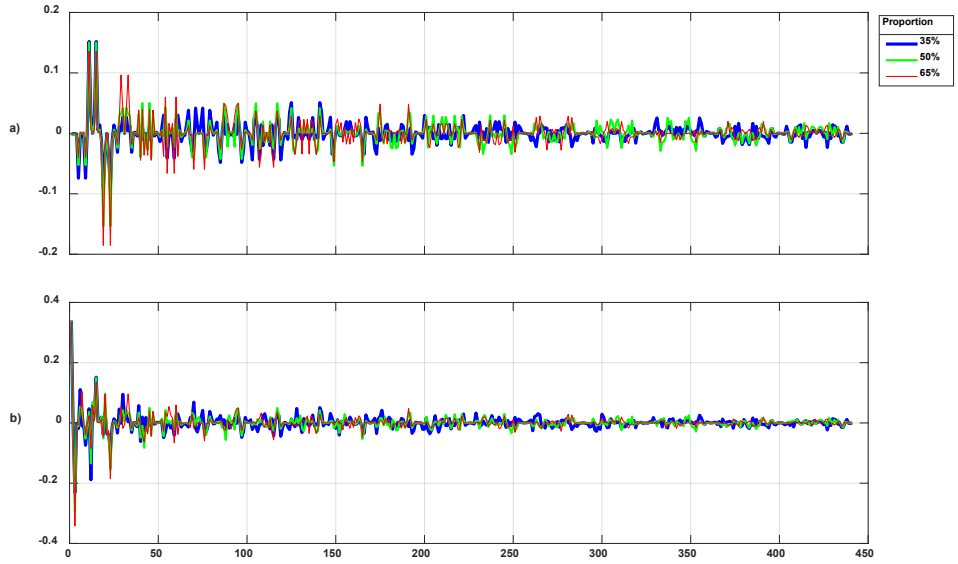

Figure 4-5 Feature vectors (20th order, 441 moments) of undefaced two based on two different polynomials, a) Pseudo-Zernike polynomials and b) Radial polynomials. The blue line represents 35%, green line represents 50% and green line represents 65%.

The RM and PZM vectors are very different from each other due to rotational variance and invariance property, respectively. These feature vectors are assessed independently to determine their suitability for fusion classification in Section 4.2.3.

4.2 Fusion Classification

The second stage of ACIP is fusion classification. Fusion classification involves defining reference classes, non-optimized classifiers, and fusion processes. Thirty-six classes of pre-

defined alphanumeric characters (0-9 and A-Z) are studied. Thirteen classifiers, including six of them with tuning parameter windows and rest with no tuning parameter, are used. A sum fusion rule is used to combine classifiers with a fixed set of tuning parameter window at each object's proportion independently. The sum fusion rule is applied across row normalized classifier values for each alphanumeric class. The number or a letter with the lowest sum value (lowest ranking) will be identified as a defaced serial number. For consensus identification, the majority vote of fusion outcomes among three different object proportions (35%, 50%, and 65%) is used to finalize the classification.

4.2.1 Reference Classes

The binary image of thirty-six alphanumeric characters (0-9 and A-Z) derived from Microsoft fonts are used. The twenty-five different fonts are used as instances for individual categories of numbers and letters. The Microsoft font names are Gungsuh, Franklin Gothic Book, Segoe UI Black, Cambria Math, Arial, New Gothic MT, Abadi, Agency FB, Bahnschrift, Bookman Old Style, Baskerville Old Face, Bauhaus, Bernard MT Conc, Bodoni MT Posted, Bodoni MT, Rockwell, Comic Sans MS, Segoe Print, Showcard Gothic, Wide Latin, Goudy Stout, Cooper Black, OCRB, Biome, and Niagara Gold. Two font styles, regular and italics, for each font are included in a class. Thus, each class contains fifty representation vectors associated with the fonts and their styles, as shown in Appendix I.

The intra-class variation based on the fifty instances in each class for three different object proportions is analyzed using PCA via SVD [95]. SVD factorizes a matrix (**X**), containing representation vectors, into three different matrices, as shown in Equation 4.11.

$$\mathbf{X}_{m\times n} = \mathbf{U}_{m\times k}\mathbf{\Sigma}_{k\times k}\mathbf{V}^{T}_{n\times k} \tag{4.11}$$

where:

m is the number of representation vectors

n is the length of the representation vector

k is the rank of $\mathbf{X}$ ($k \leq$ full rank)

$\mathbf{U}$ is the score matrix containing orthonormal eigenvectors ($\mathbf{u}$) or principal components (PCs)

Σ is the diagonal matrix of singular values,

$\mathbf{V}$ is the loading matrix containing orthonormal eigenvectors ($\mathbf{v}$)

The principal components (PCs) or scores describe the relationship between the feature vectors. Each principal component contains some percentage of variability among representation vectors. The first PC contains the highest percentage of $\mathbf{X}$ information since the first PC characterizes the mean representation vector of $\mathbf{X}$. The percentage decreases successively at higher PCs. The first few principal components describe a large percentage of the overall variation in $\mathbf{X}$; the first three principal components are used for the study.

The PCA analysis is the preliminary study that provides necessary information outlining the suitability of different image representation vectors (RM or PZM), an object proportion (35%, 50%, and 65%) for classification. For the comparison, thirty-six alphanumeric classes are included in $\mathbf{X}$. The variability among PZM and ZM is studied to assess the contrast between the moments. For this analysis, $\mathbf{X}$ contains RM and PZM vectors of all three object percentages. The first three PCs explain 74.3% of the variation that approximates overall variation. Also, the variability among the object's proportion for PZM and RM are analyzed independently. The first three PCs explain 82.5% of the variation in $\mathbf{X}$ with RM vectors and 71.1% for PZM. Figure 4.6a

shows the visual contrast between RM and PZM. Figure 4.6b and 4.6c represent the variation among three different object's proportion of RM and PZM, respectively.

The score plot indicates that there is a significant separation between RM and PZM. Also, there is good separation among the object's proportion for RM and PZM, respectively. Based on this analysis, it would be better to use a particular situation (individual moment of a specific object's size) as an independent reference library to classify the unknown defaced number with

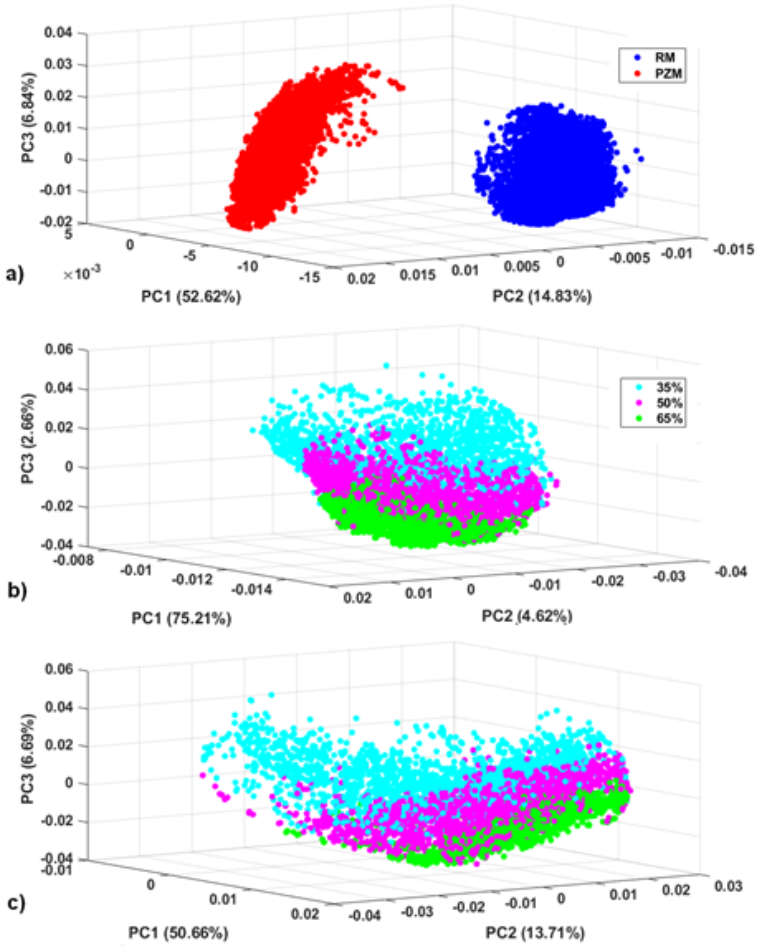

Figure 4-6 Three-Dimensional (3-D) Score Plot; a) RM vs. PZM
b) 35% vs. 50% vs. 65% (RM), c) 35% vs. 50% vs. 65% (PZM).

matching object proportion. Figure 4.6b and 4.6b suggests that the first PC captures significantly lower variance among classes with PZM (50.66%) compared to RM (75.21%). This observation

indicates classes with RM have more inter-class variation, which makes RM more suitable than PZM for classification.

PCA analysis for inter-class variation is studied between thirty-six alphanumeric characters for both RM and PZM. The study is performed on pairs of classes with all possible combinations. A total of 630 pairs of classes are determined for the study. Equation 4.12 illustrates how PCA is performed for comparison of two classes.

$$\begin{bmatrix} \mathbf{X1}_{s\times n} \\ \mathbf{X2}_{s\times n} \end{bmatrix}_{m\times k} = \begin{bmatrix} \mathbf{U1}_{s\times k} \\ \mathbf{U2}_{s\times k} \end{bmatrix}_{m\times k} \mathbf{S}_{k\times k} \mathbf{V}^{T}_{k\times n} \tag{4.12}$$

where:

X1 is the matrix containing representation vectors of a primary class compared to,

X2 is the matrix containing representation vectors of a second class compared with,

s is the number of instances in a single class which is fifty

n is the number of representation vector in each class

U1 is the score matrix for the base class (primary)

U2 is the score matrix representing second class (secondary)

For example, the comparison of number 6 and 9

To measure the contrast, the average Euclidean distance (ED) between two classes of a pair, is calculated using Equation 4.12.

$$\overline{\mathrm{ED}} = \frac{1}{s}\sum_{p=1}^{s}\sqrt{(\mathbf{u1}_{p,1}-\mathbf{u2}_{p,1})^2+(\mathbf{u1}_{p,2}-\mathbf{u2}_{p,2})^2+(\mathbf{u1}_{p,3}-\mathbf{u2}_{p,3})^2} \tag{4.13}$$

The efficiency of inter-class variation is evaluated using ED based on the empirical threshold for Euclidean distance. The threshold defines which reference classes have minimal separation. The empirical threshold used for the analysis is the midrange of all paired classes ED values. Appendix II shows the tabulation of the similar classes to each category that satisfies the

threshold for RM and PZM individually. Using RM, there are seventeen alphanumeric characters as distinct classes, whereas PZM has fourteen classes, respectively. PZMs contributes to significantly small intra-class variation, which could be a function of rotational invariance associated with PZM. For example, numbers 6 and 9 are similar to 0 and O, which could have been caused by rotational invariance. Fixing the orientation of the character provides improved class partition. There is a better separation among classes using RM than PZM using a 35% proportion. However, the trend starts to reverse with increasing proportions. For 65% proportion, there are twenty-three distinct classes based on PZM and nineteen classes for PZM. The higher proportion gives an advantage for better separation between most classes. This study indicates RM and PZM with 65% to be more appropriate for classification. However, the confidence in the outcome of classification depends on the single classified classes.

4.2.2 Classifiers

There is a total of thirteen single classifiers, including six tuning parameter-based classifiers and seven distinct similarity measures. The standalone is used to compare a vector to a space defined by the class. In contrast, similarity measures are used to measure the similarity between a vector and a mean representation vector of each category.

- **Tuning Parameter based Classifiers**

The tuning parameter-dependent classifiers are kNN, PLS-DA, Mahalanobis distance (MD) [92], Q-residual (Q-res), sine, and divergence criterion (DC) [93]. Each method is based on comparing an image ($\mathbf{x}_i$), a representation vector with *n* number of moments to a category ($\mathbf{X}$), and a matrix containing image representation vectors of *m* reference images with several moments. MD, Q-res, sinβ, and DC are eigenvector-based classifiers where each class space is spanned with eigenvectors from the singular value decomposition detailed in Equation 4.11.

Classification for PLS-DA is based on the number of latent variables (LVs), and kNN is the number of neighbors.

For eigenvector-based classifiers, the class membership is based on the maximum separation among the classes. The classifier value is transformed so that the class membership is based on the lowest value. Each predicted class value $\hat{y}_{unk}$ for PLS-DA is transformed to a minimum value $\hat{y}_t = \hat{y}_{max} - \hat{y}_{unk}$, where $\hat{y}_{max}$ is the maximum predicted value over all rows of the predicted values for individual windows. The minimum values are evaluated using $NN_{unk} = NN_{max} - NN$ for kNN algorithm. The NN_{max} is maximum nearest neighbor (NN) value over all rows of NN values for specific windows. The list of the equations (4.14-4.19) to compute these six classifiers are mentioned below:

1. kNN via Euclidean distance

$$d_{unk,j} = \left\| \mathbf{x}_{unk} - \mathbf{x}_j \right\| \quad j=1,\ldots,n \tag{4.14}$$

where:

n is the number of nearest neighbors

$\mathbf{x}_{unk}$ is the representation vector of the unknown image

$\mathbf{x}_j$ is the representation vector of reference classes

2. PLS-DA

$$\mathbf{Y}_{m\times n} = \mathbf{X}_{m\times p}\mathbf{B}_{p\times n} \qquad \hat{\mathbf{B}} = \mathbf{X}_k^{+}\mathbf{Y} \qquad \hat{\mathbf{y}}_{unk} = \mathbf{x}_{unk}^{\mathrm{T}}\hat{\mathbf{B}} \tag{4.15}$$

where:

p is the length of the representation vector (441 moments)

m is the total number of instances in thirty-six classes (1800 instances)

n is the number of classes (36 alphanumeric characters)

X is the augmented matrix of all 36 classes containing representation vectors

Y is the augmented matrix of 36 blocks (represents 36 classes respectively) with dummy variables (1 and -1); each block has 50 rows, and 36 columns in which an individual column representing the class belonging to is denoted by one and rest of the columns are -1.

k is the number of LVs

$\mathbf{X}^{+}$ is the pseudo-inverse of **X**.

3. Mahalanobis Distance (MD)

$$\tilde{\mathbf{C}} = \tilde{\mathbf{X}}^{\mathrm{T}}\tilde{\mathbf{X}} \qquad \tilde{\mathbf{C}} = \mathbf{U}\mathbf{S}\mathbf{V}^{\mathrm{T}} \qquad \tilde{\mathbf{C}}_k^{+} = \mathbf{V}_k\mathbf{S}_k^{-1}\mathbf{U}_k^{\mathrm{T}}$$
$$\mathrm{MD}_{unk} = \sqrt{\left(\mathbf{x}_{unk} - \overline{\mathbf{x}}\right)^{\mathrm{T}} \tilde{\mathbf{C}}_k^{+} \left(\mathbf{x}_{unk} - \overline{\mathbf{x}}\right)} \tag{4.16}$$

where:

X is the matrix containing representation vectors of each class

$\tilde{\mathbf{X}}$ is the column-wise mean-centered **X**

$\overline{\mathbf{x}}$ is the mean representation vector of **X**

$\tilde{\mathbf{C}}$ is the covariance matrix of $\tilde{\mathbf{X}}$

$\tilde{\mathbf{C}}^{+}$ is the pseudo-inverse of $\tilde{\mathbf{C}}$

k is the number of eigenvectors

4. Q- res

$$\mathbf{x}_{unk}^{\perp} = (\mathbf{I} - \mathbf{V}_k\mathbf{V}_k^{\mathrm{T}})\mathbf{x}_{unk} \qquad \mathbf{X} = \mathbf{U}\mathbf{S}\mathbf{V}^{\mathrm{T}}$$
$$\mathrm{Q}_{unk} = \left\|\mathbf{x}_{unk}^{\perp}\right\| \tag{4.17}$$

5. Sine

$$\sin\beta_i = \frac{\left\|\mathbf{x}_{unk}^{\perp}\right\|}{\left\|\mathbf{x}_{unk}\right\|} \tag{4.18}$$

6. Divergence Criterion

$$\mathbf{C} = \mathbf{X}^{\mathrm{T}}\mathbf{X}$$

$$\mathrm{DC}_i = \left|\tfrac{1}{2} tr\left(\left(\mathbf{x}_{unk} - \mathbf{C}\right)\left(\mathbf{x}_{unk}^{+} - \mathbf{C}_k^{+}\right)\right)\right| + \left|\tfrac{1}{2} tr\left(\left(\mathbf{x}_{unk}^{+} + \mathbf{C}_k^{+}\right)\left(\mathbf{x}_{unk} - \overline{\mathbf{x}}\right)\left(\mathbf{x}_{unk} - \overline{\mathbf{x}}\right)^{\mathrm{T}}\right)\right| \quad (4.19)$$

where:

tr is the sum of the diagonal elements of a matrix

C is the covariance matrix of **X**

$\mathbf{C}^{+}$ are the pseudo-inverse **C**

- **Similarity Measures (SM)**

All the similarity measures are subject to minimization for fusion classification. Cosine angle, ED, inner product correlation, and determinant measures the similarity or dissimilarity between two vectors [94]. Procrustes analysis (PA) [95] is transformed to account for additifonal two classifiers.

There are two types of PA; one is unconstrained PA, which determines the degree of difficulty based on the rotation and dilation contained in the transformation matrix $(\mathbf{T}_{unk})$ to map $\mathbf{x}_{unk}$ onto $\overline{\mathbf{x}}$ by $\overline{\mathbf{x}} = \mathbf{x}_{unk}\mathbf{T}_{unk}$. The sample transformation matrix $\mathbf{T}_{unk}$ ($\mathbf{T}_{unk} = \mathbf{x}_{unk}^{+}\overline{\mathbf{x}}$) uses the pseudo inverse ($\mathbf{x}_{unk}^{+}$), which is derived by $\mathbf{x}_{unk}^{+} = \left(\frac{\mathbf{x}_{unk}}{\| \mathbf{x}_{unk} \|}\right)\left(\frac{1}{\| \mathbf{x}_{unk} \|^2}\right)\left(\frac{\mathbf{x}_{unk}}{\| \mathbf{x}_{unk} \|}\right)^{\mathrm{T}} = \frac{\mathbf{x}_{unk}\mathbf{x}_{unk}^{\mathrm{T}}}{\| \mathbf{x}_{unk} \|^4}$. In order to determine the degree of rotation and dilation information contained in $\mathbf{T}_{unk}$, a reference or unknown transformation matrix is required. The reference $\mathbf{T}$ $(\mathbf{T} = \mathbf{x}^{+}\overline{\mathbf{x}})$ is an evaluation of self-transformation with the pseudo inverse ($\overline{\mathbf{x}}^{+}$) calculated similarly to $\mathbf{x}_{unk}^{+}$. The Frobenius

norm of the difference between $\mathbf{T}$ and $\mathbf{T}_{unk}$ is evaluated as $\Delta\mathbf{T}_{unk} = \| \mathbf{T}_{unk} - \mathbf{T} \|_F$ where $\| \ \|_F$ denotes the Frobenius norm.

The other type of PA is constrained PA, which involves separating the rotation and dilations into an orthogonally constrained rotation matrix ($\mathbf{H}_{unk}$) and a dilation constant (ρ_{unk}). These variables are used to transform $\mathbf{x}_{unk}$ to $\overline{\mathbf{x}}$ ($\overline{\mathbf{x}} = \rho_{unk}\mathbf{x}_{unk}\mathbf{H}_{unk}$). Similar to unconstrained PA, a reference $\mathbf{H}$ and ρ are required for self-transformation. The listed equation 4.23 shows how to compute the rotation matrix and dilation constant for both the target binary image and the mean reference classes. The Frobenius norm of the differences in rotation matrices and dilation constants are evaluated between the test serial number and means of the reference classes. In both PAs', the higher the degree of difficulty, the more likely the phase binary image does not belong to the particular class. The mathematical equations (4.20-4.26) for six similarity measures are presented below:

7. Cosine

$$1 - \cos\theta_i = 1 - \frac{\mathbf{x}_i^{\mathrm{T}}\overline{\mathbf{x}}}{\|\mathbf{x}_i\|\|\overline{\mathbf{x}}\|} \tag{4.20}$$

8. Euclidean distance

$$d_{unk} = \|\mathbf{x}_{unk} - \overline{\mathbf{x}}\| \tag{4.21}$$

9. Determinant

$$det_{unk} = \mathrm{Det}\left(\begin{bmatrix}\mathbf{x}_{unk}^{\mathrm{T}} \\ \overline{\mathbf{x}}^{\mathrm{T}}\end{bmatrix}\begin{bmatrix}\mathbf{x}_{unk} & \overline{\mathbf{x}}\end{bmatrix}\right) = \left(\|\mathbf{x}_{unk}\|\|\overline{\mathbf{x}}\|\sin\theta_i\right)^2 \tag{4.22}$$

This resource was prepared by the author(s) using Federal funds provided by the U.S. Department of Justice. Opinions or points of view expressed are those of the author(s) and do not necessarily reflect the official position or policies of the U.S. Department of Justice.

10. Procrustes Analysis (unconstrained)

$$\begin{aligned}
&\overline{\mathbf{x}} = \mathbf{x}_{unk}\mathbf{T}_{unk} \qquad\qquad \mathbf{T}_{unk} = \mathbf{x}_{unk}^{+}\overline{\mathbf{x}} \\
&\overline{\mathbf{x}} = \overline{\mathbf{x}}\mathbf{T} \qquad\qquad \mathbf{T} = \overline{\mathbf{x}}^{+}\overline{\mathbf{x}} \\
&\Delta T_{unk} = \left\|\mathbf{T}_{unk} - \mathbf{T}\right\|_F
\end{aligned} \tag{4.23}$$

11. Procrustes Analysis (constrained)

$$\begin{aligned}
&\overline{\mathbf{X}} = \rho_{unk}\mathbf{x}_{unk}\mathbf{H}_{unk} \\
&\mathbf{x}_{unk}^{\mathrm{T}}\overline{\mathbf{x}} = \mathbf{U}_{unk}\mathbf{S}_{unk}\mathbf{V}_{unk}^{\mathrm{T}} \\
&\mathbf{H}_{unk} = \mathbf{U}_{unk}\mathbf{V}_{unk}^{\mathbf{T}} \qquad\qquad \rho_i = \frac{tr(\mathbf{S}_{unk})}{tr(\mathbf{x}_{unk}x_{unk}^{\mathbf{T}})} \\
&\overline{\mathbf{x}} = \rho\overline{\mathbf{x}}\mathbf{H} \\
&\overline{\mathbf{x}}^{\mathrm{T}}\overline{\mathbf{x}} = \mathbf{U}\mathbf{S}\mathbf{V}^{\mathrm{T}} \\
&\mathbf{H} = \mathbf{U}\mathbf{V}^{\mathbf{T}} \qquad\qquad \rho = \frac{tr(\mathbf{S})}{tr(\overline{\mathbf{x}}\overline{\mathbf{x}}^{\mathbf{T}})} \\
&\Delta H_{unk} = \left\|\mathbf{H}_{unk} - \mathbf{H}\right\|_F
\end{aligned} \tag{4.24}$$

$$\Delta\rho_{unk} = \left|\rho_{unk} - \rho\right| \tag{4.25}$$

12. Inner Product Correlation

$$1 - r_i = 1 - \frac{tr(\mathbf{x}_{unk}^{\mathrm{T}}\overline{\mathbf{x}})}{\sqrt{tr\left(\mathbf{x}_{unk}^{\mathrm{T}}\mathbf{x}_{unk}\right)tr(\overline{\mathbf{x}}^{\mathrm{T}}\overline{\mathbf{x}})}} \tag{4.26}$$

4.2.3 Fusion

Fusion is carried out using all thirteen classifiers with RM. The sum fusion rule is the most commonly used fusion process for classification [93,96,97]. The fixed tuning parameter window size close or equal to full rank is applied to avoid tuning parameter selection. The window size of forty-five is selected based on the minimum across full rank for each class used in eigenvector-based classifiers. The number of nearest neighbors for kNN is the same as the tuning parameter window used for eigenvector-based classifiers. Before fusion, classifier values were row normalized to unit length in order to eliminate magnitude differences between the

classifiers. The normalized row values are summed for each class, and the class with the lowest sum value is the classified number or letter. Each tuning parameter window for tuning parameter-based classifiers has the same contribution as the individual similarity measures in the fusion process. For each object proportion, the same window size is used for eigenvector-based classifiers. Figure 4-7 shows the normalized raw values of six tuning parameter-based classifiers at each window and SM along with sum fusion value for identification of phase image associated with undefaced 2 (35% proportion).

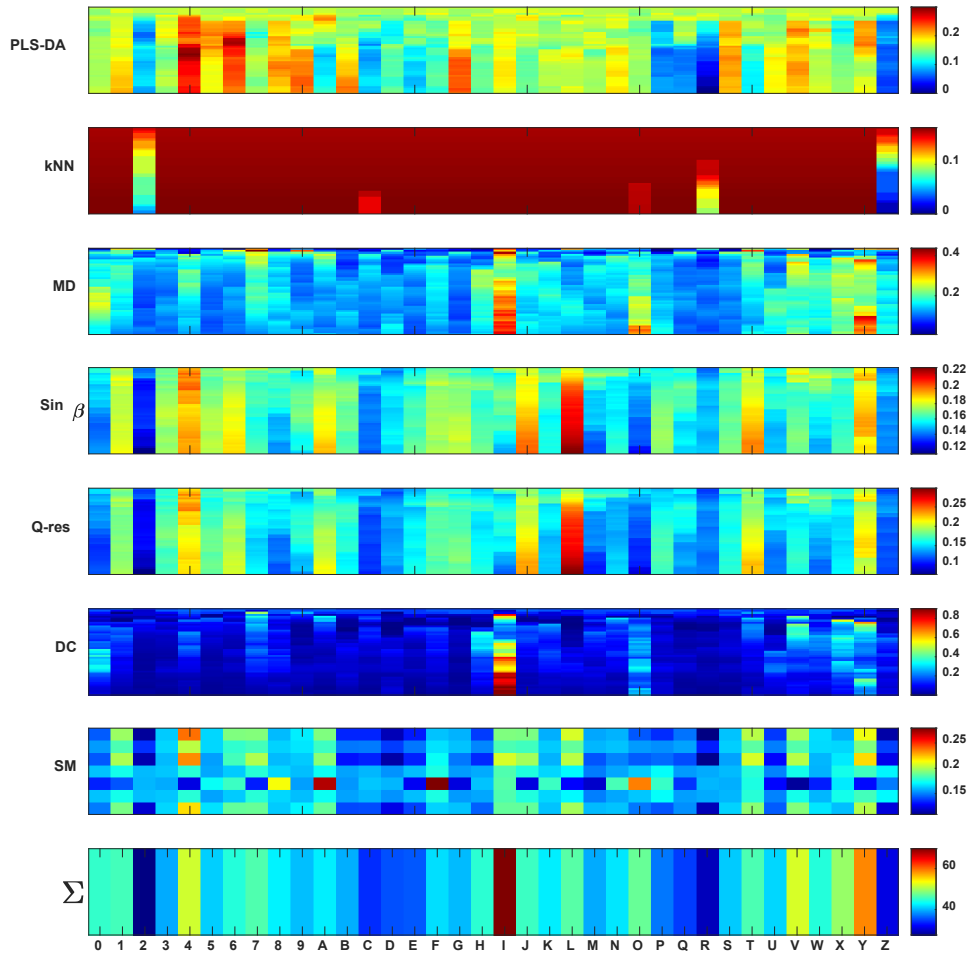

Figure 4-7 Fusion Classification input matrix and sum fusion value (undefaced 2 - original) with RM of a specific proportion (35%) and tuning parameter window size of forty-five

Some classifiers look to misclassify the unknown two as a letter Z or R. PLS-DA, and kNN classifies the unknown as a letter Z. The sine, Q-residual, and some similarity measures look obvious that these classifiers would individually categorize the image as a number 2. However, the rest of the classifiers, including MD and DC, are visually inconclusive. The lowest sum fusion value indicates that the unknown is identified as number 2. Figure 4-8 represents the normalized classifier values of undefaced 2 using PZM.

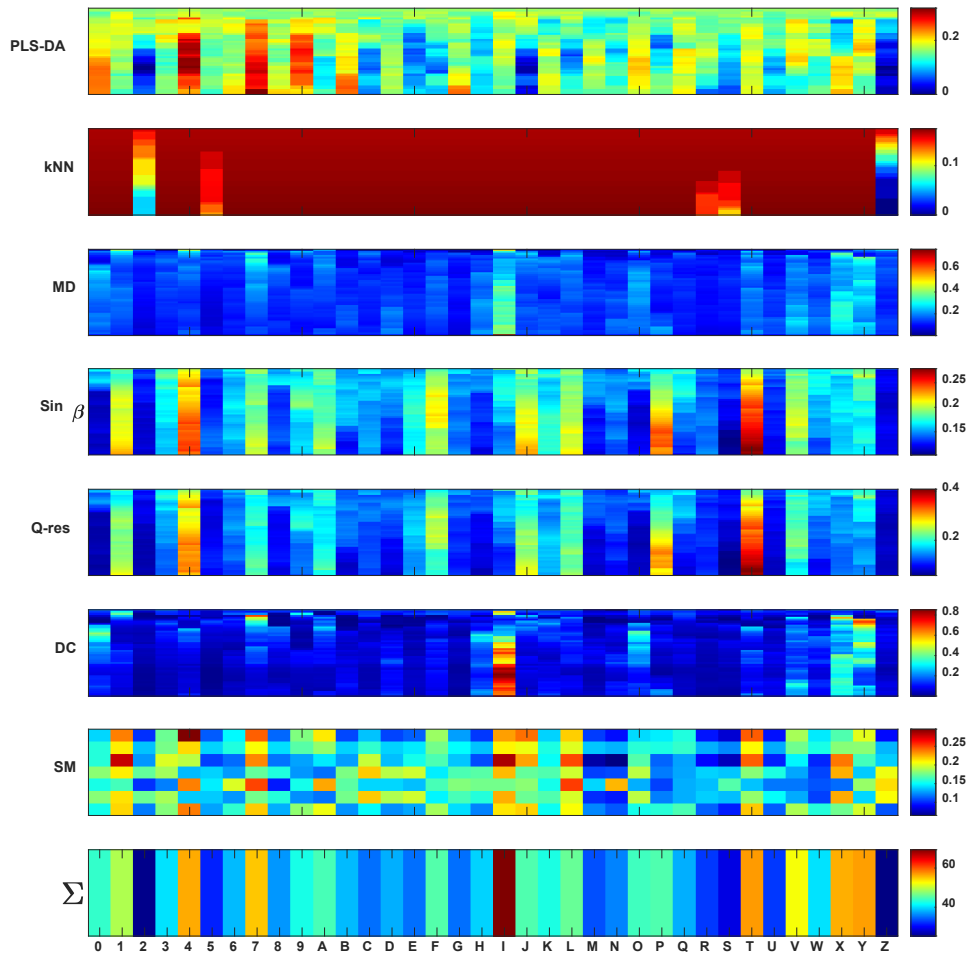

Figure 4-8 Fusion Classification input matrix and sum fusion value (undefaced 2 - original) with PZM of a specific proportion (35%) and tuning parameter window size of forty-five

In figure 4-8, using PZM, PLS-DA, and kNN classify the unknown image as a letter Z. The sinβ and Q-res categorize the character as number 0 or 2, or a letter S. Fusion process could not completely isolate the identity of the unknown number as classes belonging to number 2 and letter Z has very similar low sum fusion value. Figure 4-9 represents the normalized classifier values of undefaced 2 using RM at 65% proportion.

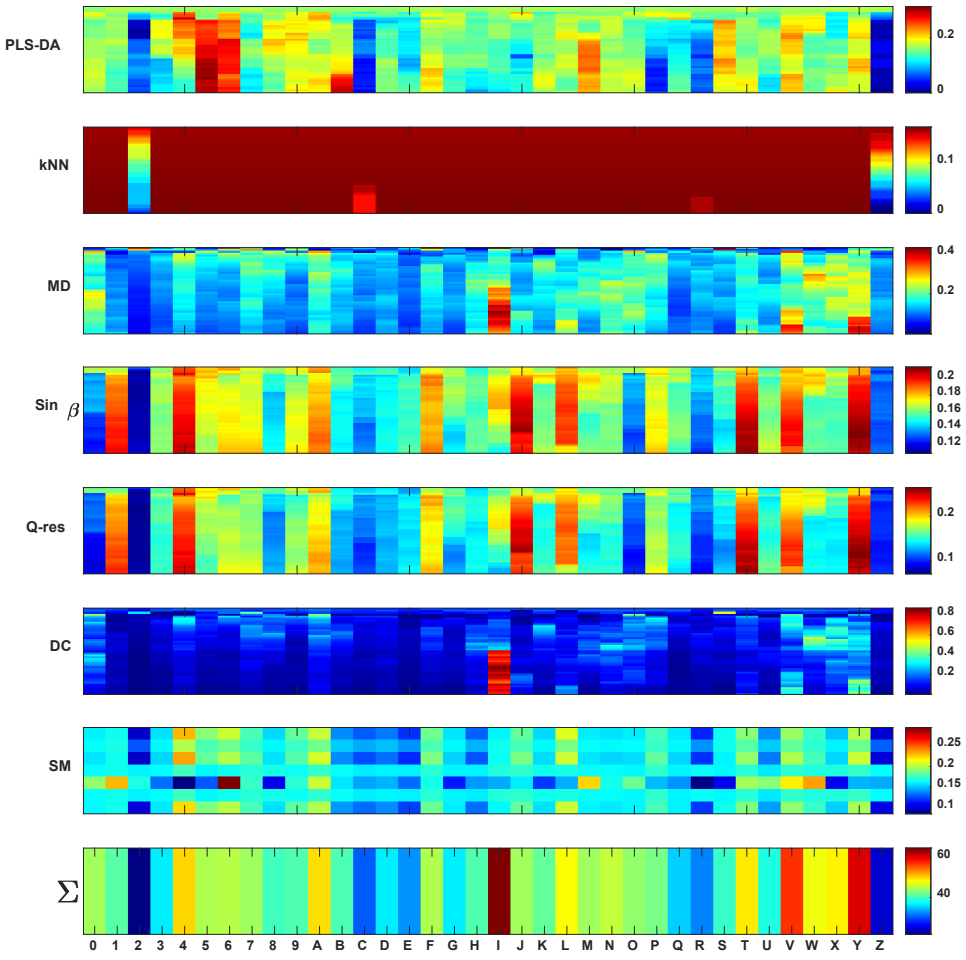

Figure 4-9 Fusion Classification input matrix and sum fusion value (undefaced 2 - original) with RM of a specific proportion (65%) and tuning parameter window size of forty-five

In Figure 4-9, with sinβ and Q-residual for RM, the possibility of number two for correct identification increased with more tuning parameter windows identifies the number correctly. However, the unknown is categorized as a letter Z based on PLS-DA and kNN. The next best candidate is number 2. The selection between R M and PZM looks to affect the individual classifier's performance. Figure 4-10 represents the normalized classifier values and sum fusion values of undefaced two based on PZM and 65% proportion.

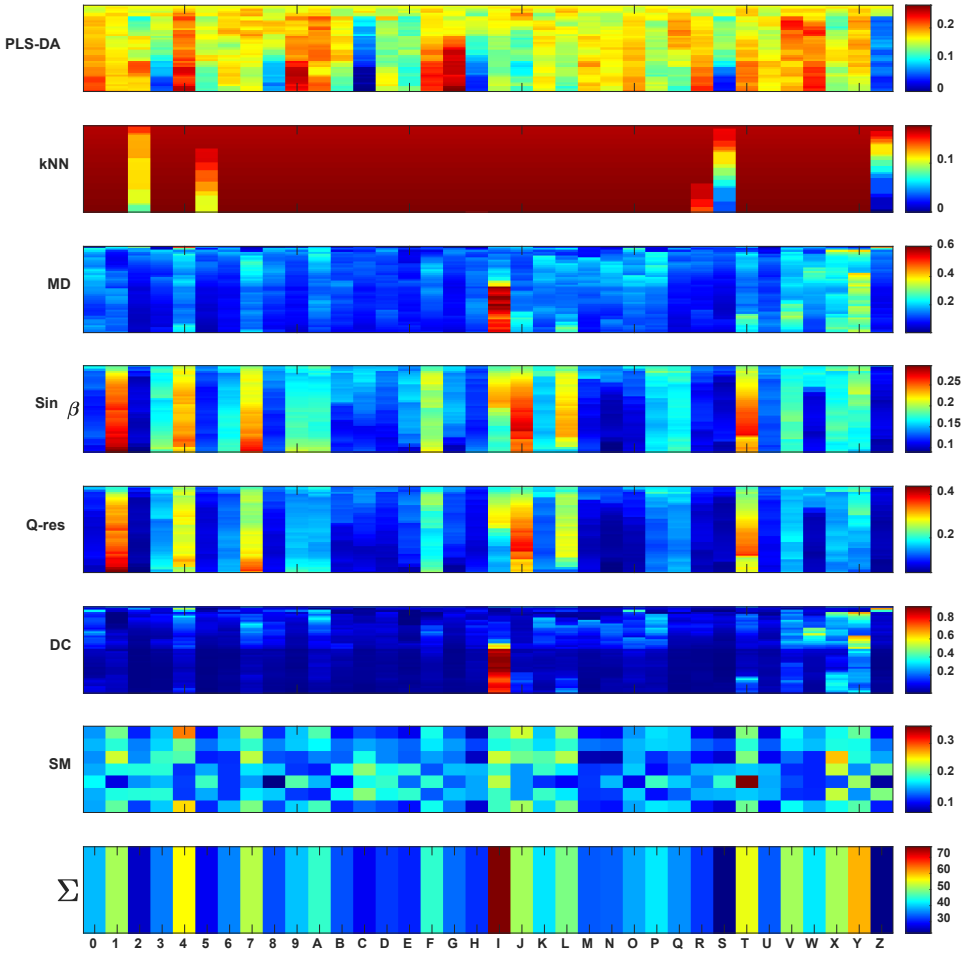

Figure 4-10 Fusion Classification input matrix and sum fusion value (undefaced 2 - original) with PZM of a specific proportion (65%) and tuning parameter window size of forty-five

Comparing Figures 4-8 and 4-10, the object's proportion does not change the identification of fusion classification with PZM. However, in Figure AIII-1 and AIII-2, with 65% proportion, the number is classified correctly. The more substantial proportion contributes to low fusion values with classified class; the number is still misclassified in both proportions for the original. For the replicate, the issue of misclassification is resolved. The outcome of the fusion classification based on PZM is entirely dependent on the object's proportion. Also, using RM in both trials of undefaced 2, Figure 4-7,4-9, AIII-3, and AIII-4 shows a higher proportion of improving most classifiers' ability to categorize the unknown image as a number two conclusively. The two proportions, both high and low, classifies the number accurately, and the outcomes are more consistent and less dependent on object proportion.

The above findings provide evidence for the slight advantage of RM over PZM for better and consistent multi-class classification with fusion. Hence, for the defaced numbers on all test samples, RM is preferred for fusion classification due to its lower dependency on object proportion for robust pattern recognition than PZM. The fusion classification at each proportion using RM would solve a single method selection dilemma. As observed in Figure 4-7, 4-8, 4-9, and 4-10, combining these thirteen classifiers is better than having to choose a single best classifier out of them for accurate identification. Additional classifiers can be incorporated without drastically changing the fusion outcome as long as the new classifiers are not redundant to the existing classifiers and maintain similar distribution of good and weak classifier values.

The analysis performed to find the optimal object's proportion for fusion classification shows the classification performance with 65% is the best among three different proportion tested. Even though the higher proportion improves classification results, and there is a high risk of adding unnecessary features or noise while increasing the proportion, and removing essential

characteristics if the proportion is decreased. The use of an optimal object's proportion is very susceptible to misclassification, similar to choosing a single best classifier. As a result, the majority vote across fusion classification outcomes of different proportions is used to avoid selection and find a reasonable consensus for identification.

Figures 4-11 and 4-12 show the identification of the lowest-ranked category based on the sum fusion of normalized classifiers values for each alphanumeric class at three different proportions for identification of undefaced number two using RM and PZM, respectively.

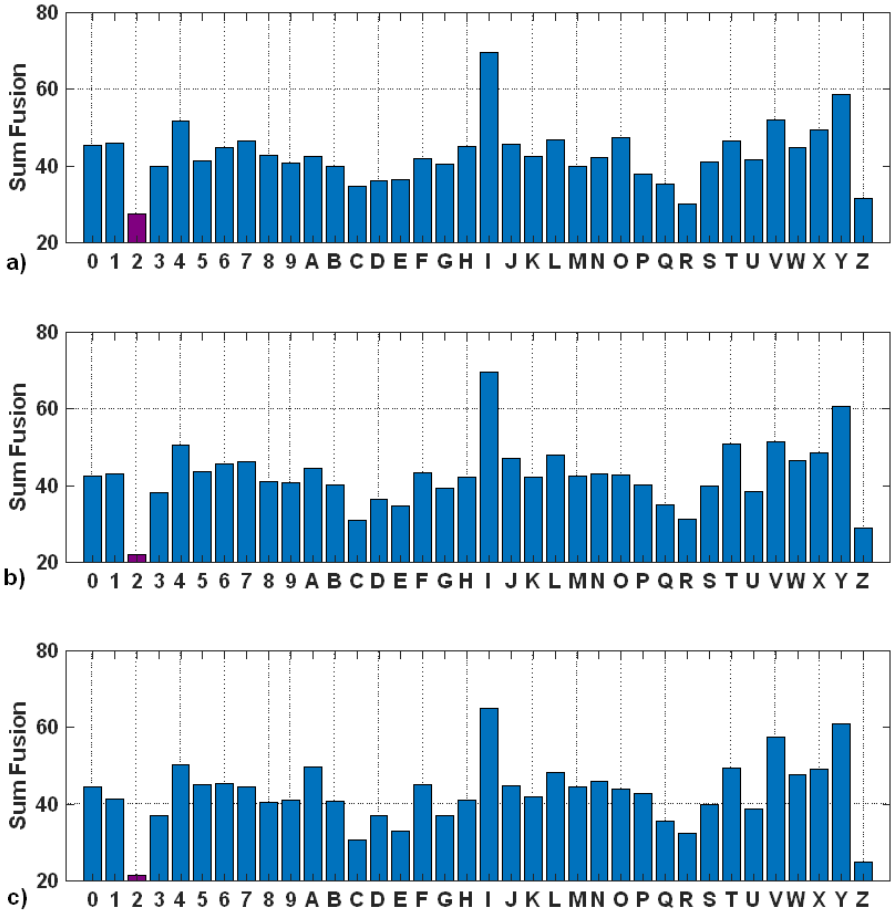

Figure 4-11 Bar plot of Sum Fusion for original of undefaced two (SS) with RM and varying object percentage a) 35%, b) 50% and c) 65%. The magenta color bar represents the lowest sum fusion value (lowest rank)

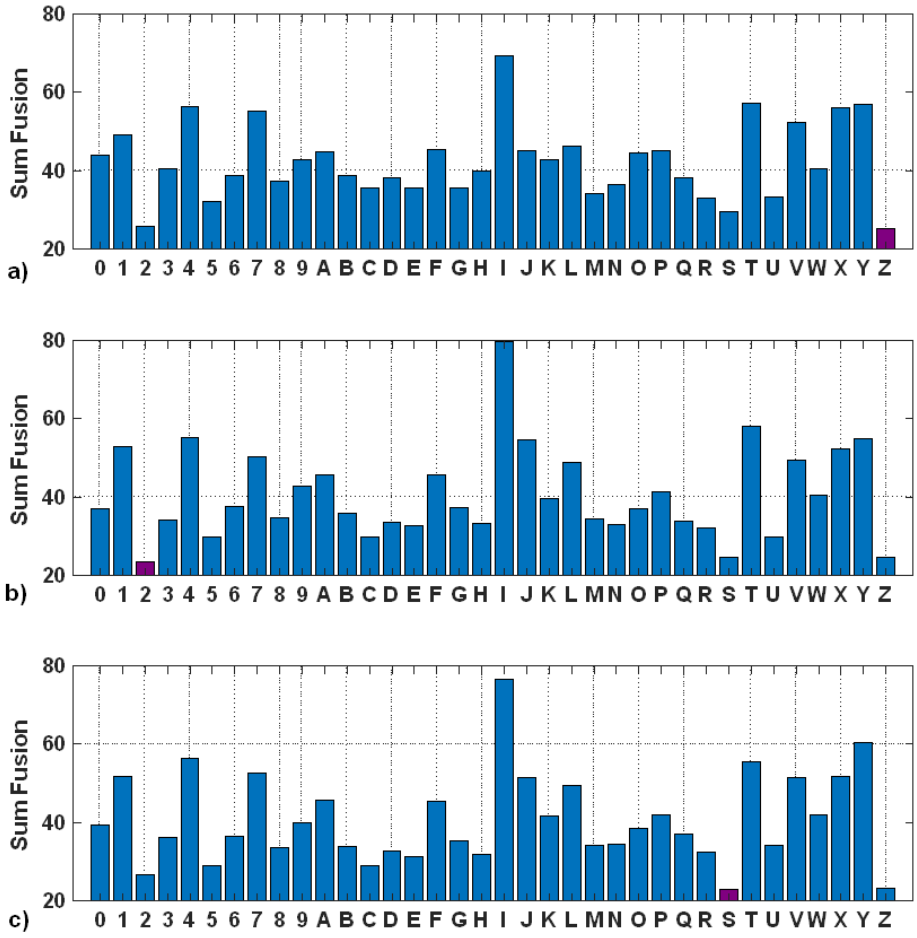

Figure 4-12 Bar plot of Sum Fusion for original of undefaced two (SS) with PZM and varying object percentage a) 35%, b) 50% and c) 65%. The magenta color bar represents the lowest sum fusion value (lowest rank)

With RM, the fusion classification identifies the serial number accurately for all three different proportions. Especially with a 65% object portion, even though most of the classifiers appeared to misclassify the number, fusion classification weighted all the available information equally and came to an accurate conclusion. The serial number was correctly identified with the absolute majority. However, using PZM, the only image with 50% proportion is identified accurately, and there is no majority vote on a classified class. A higher proportion does not necessarily classify the image to the designated class. These observations support better consensus classification with non-optimized classifiers using RM vectors.

The study performed on undefaced two firmly indicates that the proposed automatic character identification protocol (ACIP) is practical for serial number restoration minimizing human bias. However, only undefaced two (treated as pseudo defaced) was studied entirely to develop the protocol; a study on actual defaced serial number is necessary to establish the method's applicability. The lock-in procedure with the optimal range of lock-in frequency along with ACIP is tested with an actual defaced serial number for authentication.

Chapter 5

5.0 Results and Discussion

5.1 Stainless Steel (SS)

The stainless-steel plate, containing partially defaced six and completely defaced two, five, and zero, were processed through the proposed lock-in procedure at frequencies of 0.75Hz, 1Hz, and 1.25Hz. The phase images were evaluated using image analysis to determine a single frequency to recover the defaced serial number, as mentioned in Chapter 3. Table 5-1 shows the optimal frequency for each defaced number on the stainless-steel plate.

Table 5-1 Defaced serial number on Stainless Steel plate and their selected lock-in frequency.

Defaced Serial Number	Lock-in Frequency (Hz)
6	1
2	0.75
5	1
0	1

The enhanced binary images generated through image analysis on phase images are used in the automatic character identification protocol (ACIP) for pattern recognition.

- **Partially Defaced 6 (Replicate)**

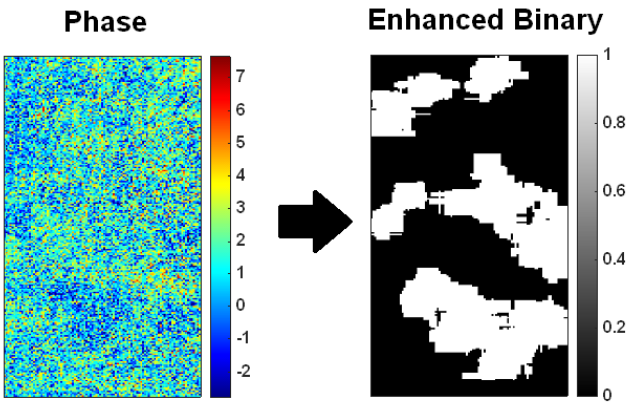

Figure 5-1 Phase and Enhanced Binary images of partially defaced Six (SS)

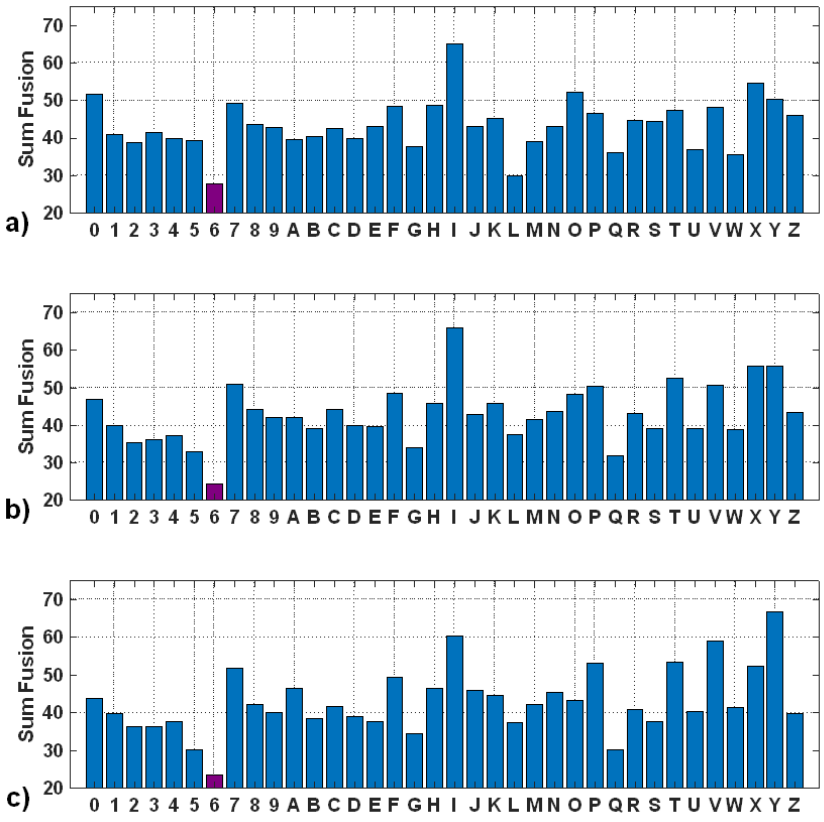

Figure 5-2 Bar plot of Sum Fusion for partially defaced six (SS) with RM and varying object percentage a)35%, b) 50% and c) 65%. The magenta color bars represent the lowest sum fusion value (lowest rank)

As shown in figure 5-2, the fusion classification classifies the recovered serial number pattern as a number six with absolute majority vote. Also, the partially defaced six shows similar trend as undefaced two about fusion classification, the classifier sum fusion value for accurately classified number gets smaller relative to the other lower ranked classes, with increased object proportion. However, the trend starts to get complex with completely defaced serial numbers as the recovered phase images do not have a very definite pattern for an absolute number or letter representation.

- **Defaced 2**

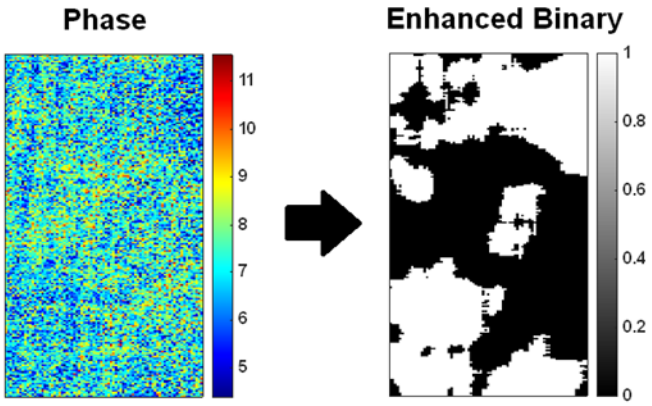

Figure 5-3 Phase and Enhanced Binary images of defaced six (SS)

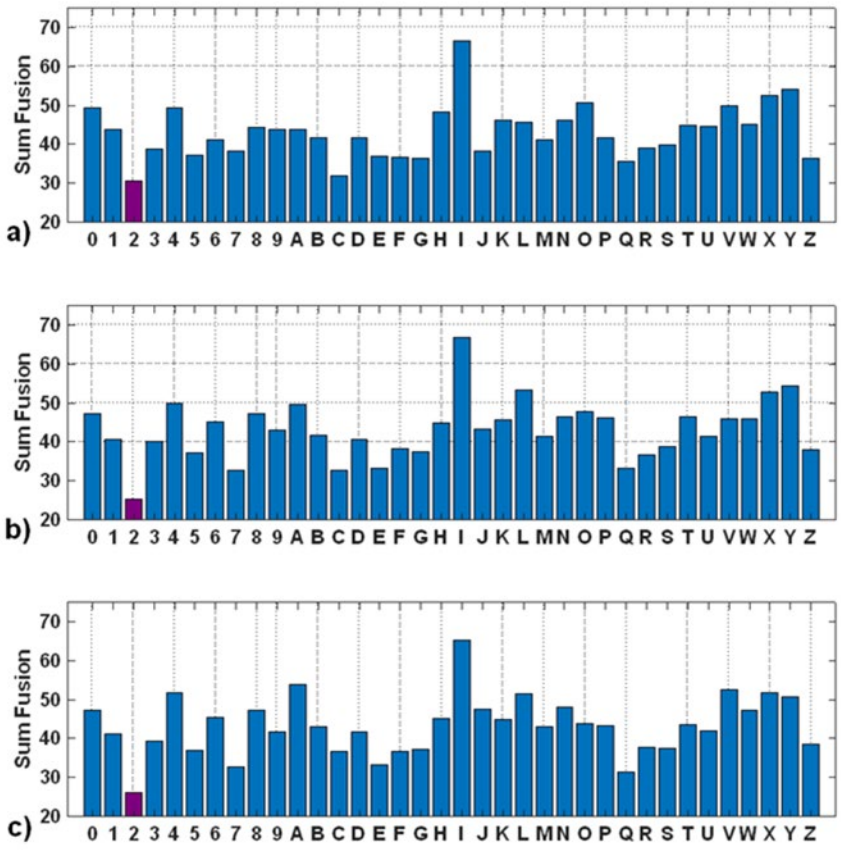

Figure 5-4 Bar plot of Sum Fusion for defaced two (SS) with RM and varying object percentage a)35%, b) 50% and c) 65%. The magenta color bars represents the lowest sum fusion value (lowest rank)

This resource was prepared by the author(s) using Federal funds provided by the U.S. Department of Justice. Opinions or points of view expressed are those of the author(s) and do not necessarily reflect the official position or policies of the U.S. Department of Justice.

- **Defaced 5**

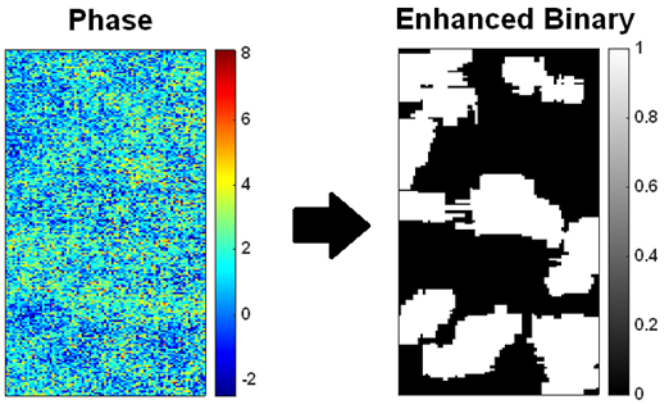

Figure 5-5 Phase and Enhanced Binary images of defaced five (SS)

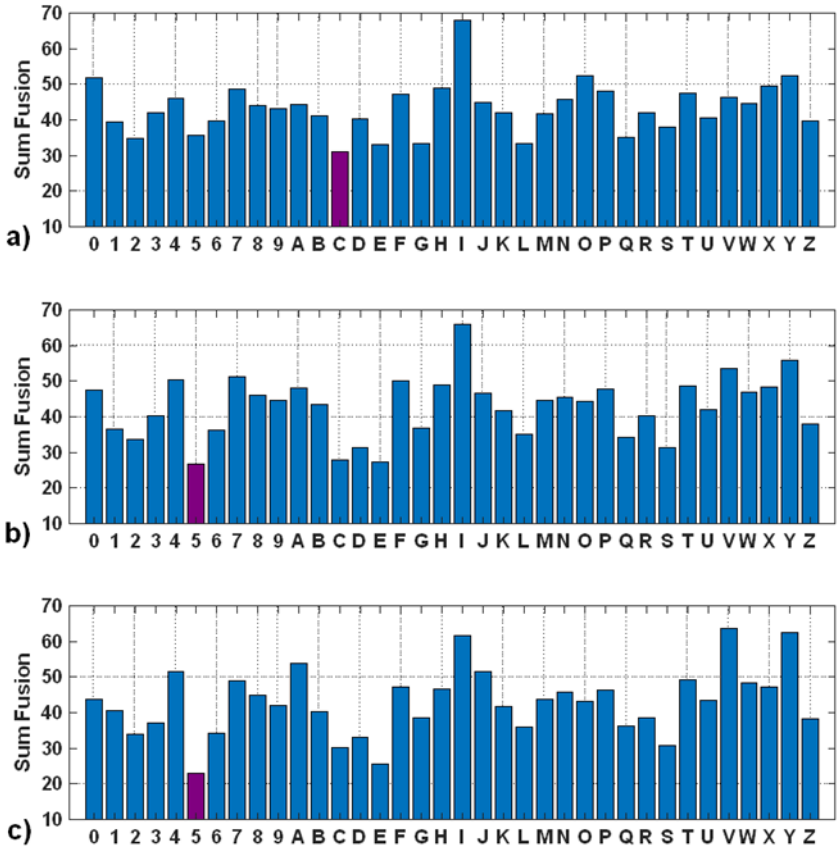

Figure 5-6 Bar plot of Sum Fusion for defaced five (SS) with RM and varying object percentage a)35%, b) 50% and c) 65%. The magenta color bars represents the lowest sum fusion value (lowest rank)

- **Defaced 0**

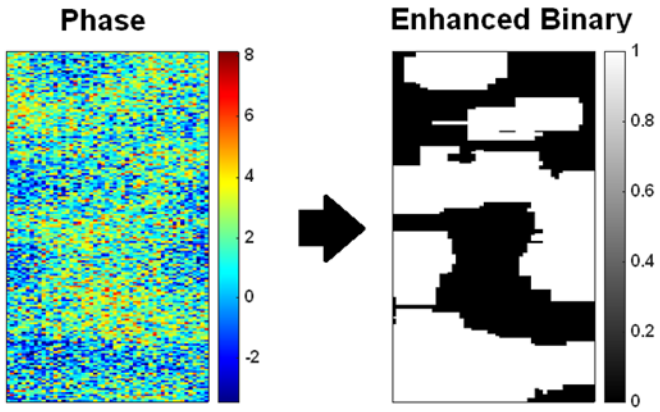

Figure 5-7 Phase and Enhanced Binary images of defaced zero

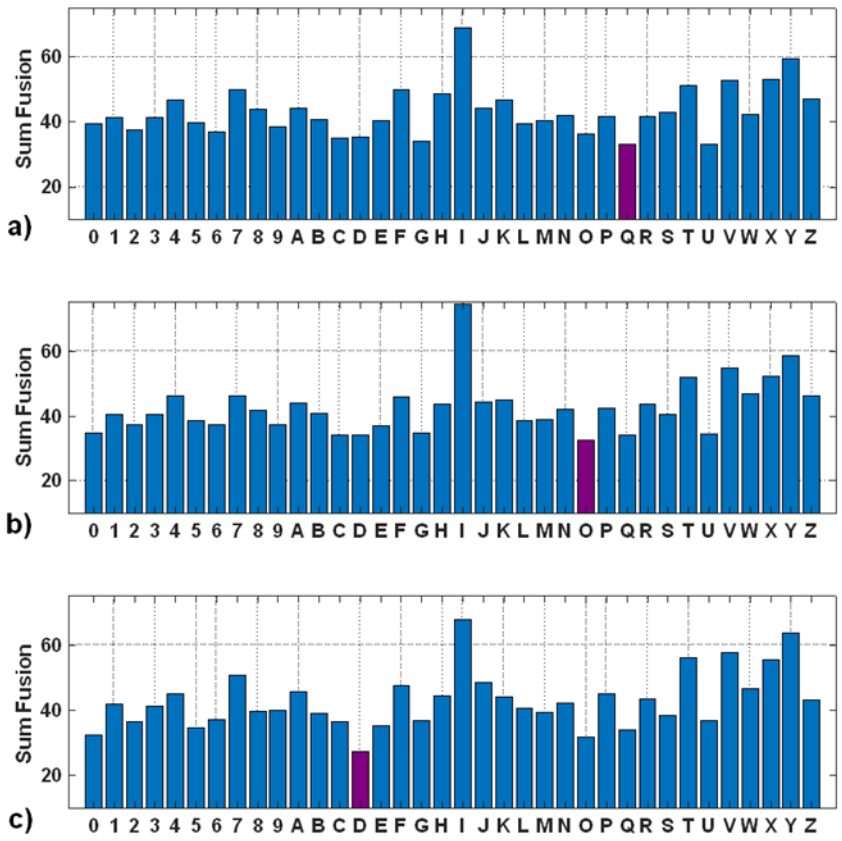

Figure 5-8 Bar plot of Sum Fusion for defaced five (SS) with RM and varying object percentage a)35%, b) 50% and c) 65%. The magenta color bars represents the lowest sum fusion value (lowest rank)

From figures 5-3 and 5-4, it can be observed that the lock-in procedure and ACIP protocol was able to correctly identify the defaced number two with an absolute majority vote (two out of three proportions). Figures 5-5 and 5-6, indicate that the lock-in procedure and ACIP protocol was able to correctly identify the defaced number five with a majority vote (two out of three proportions).

Even though figure 5-7 may suggest the recovered number as the defaced number zero based on visual interpretation, the proposed identification pattern for serial number restoration was not able to provide correct identification on any proportion set-ups, as shown in figure 5-8. This anomaly could be caused by the minimal intra-class variation between 0 and Q, O, or D defined by the Euclidean distance, as shown in Figure 4-7. Although the majority vote for classification was inconclusive, fusion classification can classify the number to a particular group of classes that is very similar to the defaced number or letter.

5.2 Gun Barrel (GB)

The two defaced numbers on a gun barrel, one and two, were treated through the proposed lock-in procedure at frequencies of 1Hz, 1.25Hz, and 1.5Hz. The phase image analysis similar to stainless steel was applied to find a single frequency to recover the defaced serial number. The pattern recognition method (ACIP) was applied for the enhanced binary image obtained from the phase image at optimal lock-in frequency. Table 5-1 shows the optimal frequency for each defaced number on the gun barrel.

Table 5-2 Defaced serial number on a Gun Barrel and their selected lock-in frequency

Defaced Serial Number	Lock-in Frequency (Hz)
1	1.5
2	1.5

- **Defaced 1**

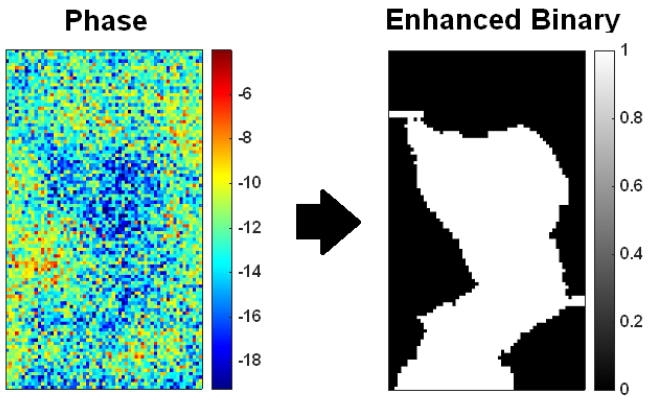

Figure 5-9 Phase and Enhanced Binary images of defaced one (GB)

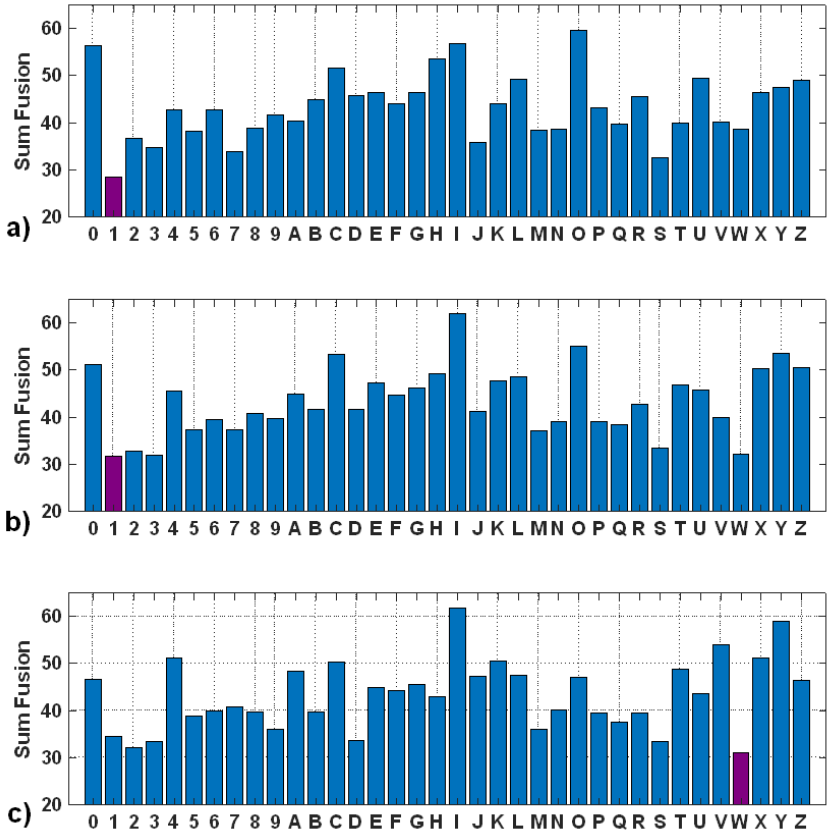

Figure 5-10 Bar plot of Sum Fusion for defaced two (GB) with RM and varying object percentage a)35%, b) 50% and c) 65%. The magenta color bars represent the lowest sum fusion value (lowest rank)

- **Defaced 2**

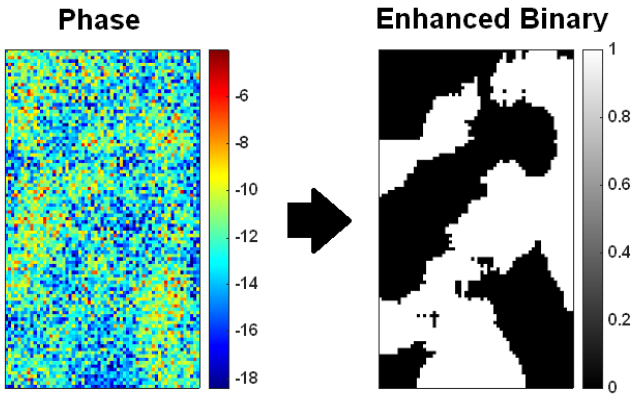

Figure 5-11 Phase and Enhanced Binary images of defaced two (GB)

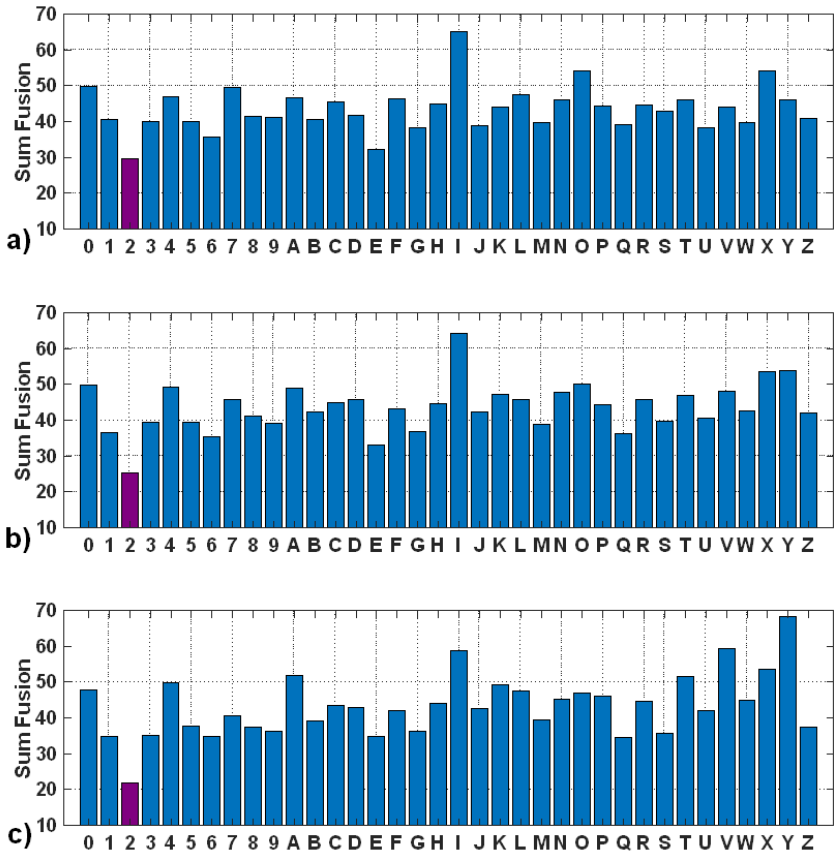

Figure 5-12 Bar plot of Sum Fusion for defaced two (GB) with RM and varying object percentage a)35%, b) 50% and c) 65%. The magenta color bars represent the lowest sum fusion value (lowest rank)

This resource was prepared by the author(s) using Federal funds provided by the U.S. Department of Justice. Opinions or points of view expressed are those of the author(s) and do not necessarily reflect the official position or policies of the U.S. Department of Justice.

Figures 5-9 and 5-10, show that the lock-in procedure along with ACIP protocol was able to correctly identify the defaced number one with the majority vote (two out of three proportions). For this particular scenario, the classifier sum fusion value for accurately classified number gets smaller relative to the other lower ranked classes, with decreased object proportion. This trend is reverse about the identity of the defaced serial number on stainless steel plate, warning the potential risk of using a fixed object's proportion. The majority vote among independent fusion classification minimizes the risk of selection. With an absolute majority vote, defaced number two is classified, as shown in figure 5-11.

5.3 Laser Engraved Needle Holder (NH)

The procedure similar to the gun barrel sample was applied. Table 5-1 shows the optimal frequency for each of the two defaced numbers (3 and 4) on a laser engraved needle handler.

Table 5-3 Defaced serial number on a needle holder and their selected lock-in frequency

Defaced Serial Number	Lock-in Frequency (Hz)
3	1.5
4	1.5

- **Defaced3**

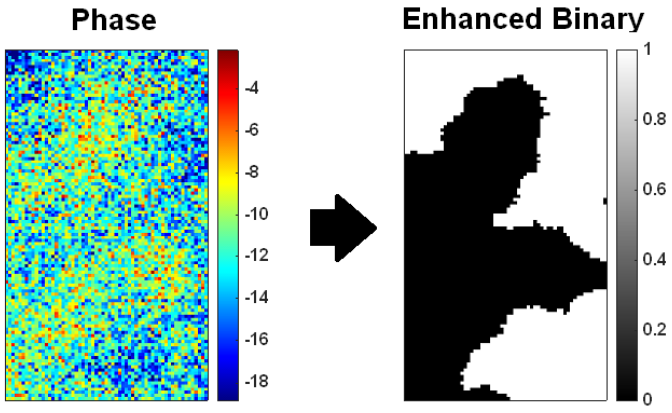

Figure 5-13 Phase and Enhanced Binary images of defaced three (NH)

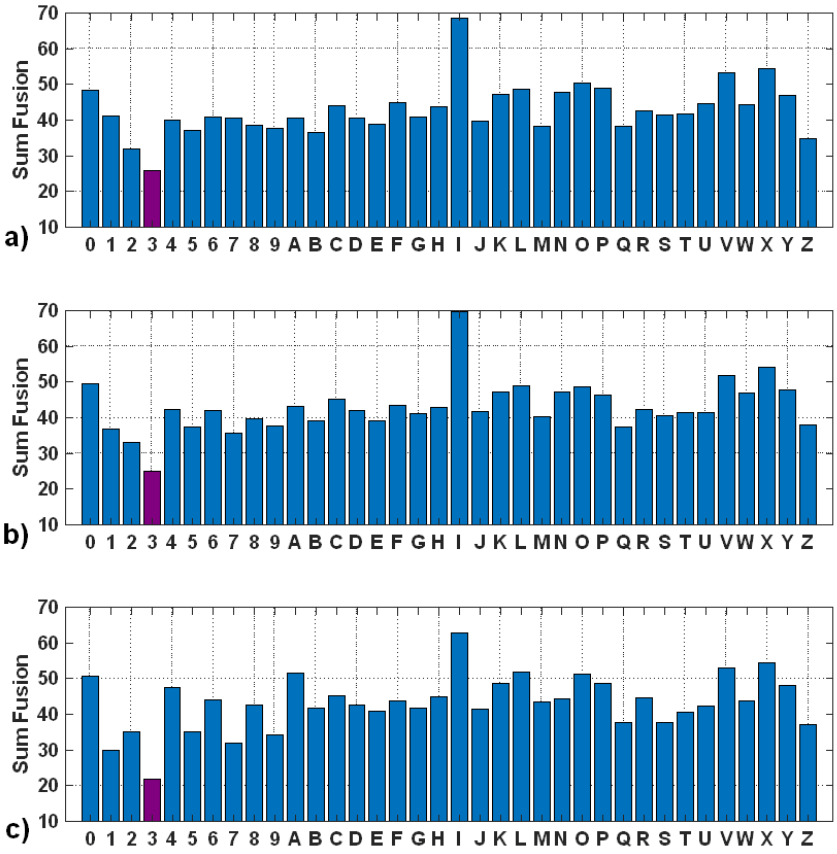

Figure 5-14 Bar plot of Sum Fusion for defaced three (NH) with RM and varying object percentage a)35%, b) 50% and c) 65%. The magenta color bars represent the lowest sum fusion value (lowest rank)

- **Defaced 4**

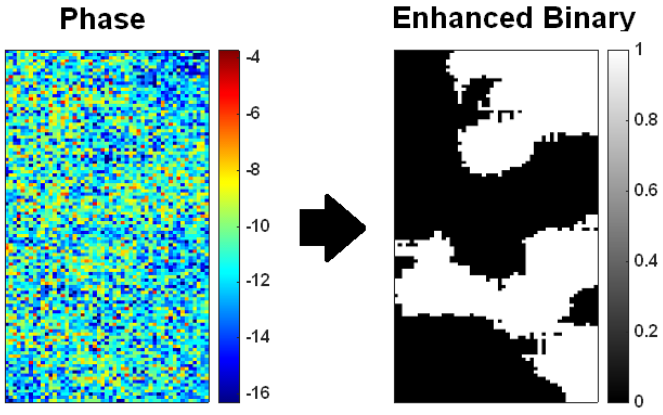

Figure 5-15 Phase and Enhanced Binary images of defaced four (NH)

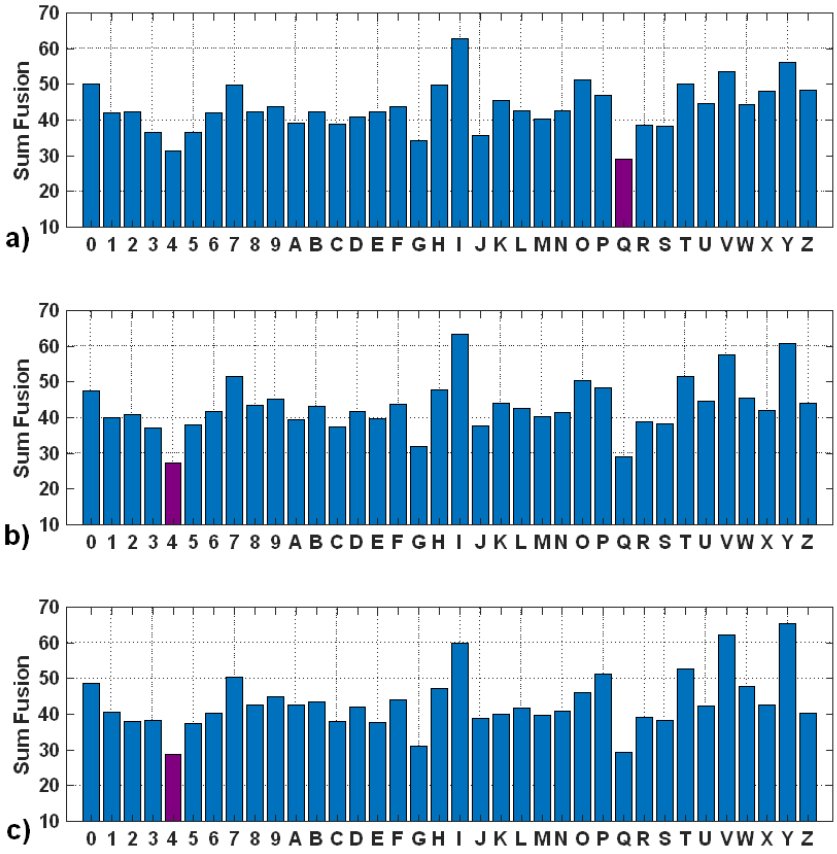

Figure 5-16 Bar plot of Sum Fusion for defaced three (NH) with RM and varying object percentage a)35%, b) 50% and c) 65%. The magenta color bars represent the lowest sum fusion value (lowest rank)

The two defaced numbers (three and four) on a laser engraved needle holder are accurately identified using ACIP on the developed phase images via lock-in.

5.4 Discussion

For serial number restoration, the lock-in procedure is the main engine. The determination of lock-in frequency is a crucial part of the procedure to avoid blind frequencies. The frequencies outside 0.5 – 2 Hz are blind frequencies where there is no contrast between plastic deformation and non-deformed area. At an optimal frequency, the features of the defaced serial number are extracted at maximum contrast. The ideal frequency for defaced serial numbers on stainless steel was 0.75Hz (defaced 2), and 1 Hz (undefaced 2; defaced 6,5, and 0) while the

other two test samples (Gun Barrel and Needle Holder) was determined to be 1.5Hz. Even though the contrast of the features is not feasible for visual interpretation, image analysis for feature enhancement helps to characterize the features' pattern efficiently. All the enhanced images for the defaced serial number on all test samples suggest that the enhanced binary image obtained from phase images via image analysis has more defined characteristics for visual interpretation and pattern recognition.

The secondary engine is the automatic character identification protocol (ACIP). The protocol depends on the quality of the feature extraction. The enhanced image for undefaced and partially defaced numbers has a clear pattern, making it easier for ACIP to identify the numbers with high confidence. The quality of the defaced number phase images varies with minimal contrast, which made automation of the identification process very difficult to achieve. However, the developed ACIP can minimize the risk of misidentification of the recovered serial number by implementing fusion classification and a majority vote. All the defaced numbers used for testing except one were accurately identified with ACIP. The misclassified defaced number presents a limitation of the protocol caused by the small intra-class variation between some of the classes. The drawback can be observed while identifying defaced number zero. There was inconclusive identification, with all of the object's proportion not identifying the defaced number to be a zero. Instead, they were classified as Q, O and D. This issue can be handled by finding an overlapping class closest to all the misclassified numbers. The zero class is closest to each of those misclassified numbers, comparing individually to Q, O, and D using Euclidean distance. The application of fusion classification with the majority vote shows efficacy for pattern recognition.

The developed lock-in procedure, primarily phase shift, can reliably extract the features of the defaced serial number within a specific range of lock-in frequency. Assuming the features

of an enhanced binary image has the pattern of obliterated serial numbers, the ACIP can be used as a standard method to identify a number or a letter.

Even though there is a reproducibility for undefaced two, it is challenging to replicate the defaced serial number restoration. For undefaced two, the temperature gradient is higher due to the significant difference between the thermal conductivity of the stamped region and the unstamped metal surface underneath the electric tape. The presence of air in the stamped region contributes to a significant difference in thermal conductivity. However, for defaced numbers, there is a negligible temperature gradient between the deformed and non-deformed areas of metal since there is no air pocket. The reproducibility with feature extraction using lock-in thermography is a concern for defaced serial number restoration. The problem is addressed by fine-tuning the best lock-in frequency for the individual defaced number in a very controlled environment, such as a steady thermal energy wave. The depth of defacing can be used as a guideline to adjust lock-in frequency within the optimal range of 0.5 – 2Hz. The defaced numbers of a gun barrel and a need holder were restored at the higher end of the optimal range (1.5Hz). The depth of defacing for these samples is relatively small compared to the stainless-steel samples. The extracted pattern is reproducible based on the study but does not necessarily resemble the defaced number accurately. Prior knowledge of exact deformed location on the metal surfaces increases the degree of accuracy and reproducibility for recovery of the defaced serial number.

Chapter 6

6.0 Conclusion

A primary motivation in this study was to develop a reliable experimental design and feature extraction for serial number restoration via infrared lock-in thermography. The experimental design was modified from the previously developed method. The essential modifications were sample surface preparation, use of black tape rather than paint to absorb the laser power and lower the emissivity. The experiment was carried out at room temperature rather than an elevated one. Application of these techniques to a non-defaced serial number provided appropriate settings to find the best range of lock-in frequency for serial number restoration. The phase shift, a lock-in technique to compress thermal images, is the most fitting approach to extract plastic strain features underneath the metal surface. The surface temperature gradient has a very insignificant effect on the spatial distribution of phase shift compared to amplitude. This superiority allows performing feature extraction across all samples defaced serial numbers consistently. The developed lock-in procedure in this study makes it possible for the feature extraction with the phase shift at the single best lock-in frequency for each defaced serial number. The feature extraction on the previously developed method was based on multivariate image analysis (MIA), performing PCA on multiple phase images. PCA requires determining the number of phase images for reliable feature extraction. The newly developed procedure eliminates the necessity of MIA and still extract useful features. The adjustment in experimental design enhances the efficacy of lock-in thermography for feature extraction without applying MIA on multiple temporal phase images.

The other significant aim of this study was to develop an automatic character identification protocol (ACIP) for identifying phase image features that could be a defaced

number or letter. The protocol is proposed to be user friendly and independent of any human bias. Image analysis, including binarization, smoothing, segmentation, dilation, and erosion, was performed, which was able to enhance the features for identification. Both numbers and letters were used as references, making the identification process complex due to the presence of some references with similar patterns. Fusion classification was used as an alternative to library matching with fusion based on PZM. The applicability of PZM due to rotational invariant property diminishes with an increasing number of classes, whereas the use of RM with no rotational invariance is suitable for classification. In conclusion, fusion classification was able to consistently classify the features in the phase image as a number or letter that would be the identity of a defaced serial number.

The success of the revised non-destructive method on all samples shows the possibility of its use as a standard method for serial number restoration. The experiments carried out in this study validates the flexibility and consistency of the lock-in procedure across varying defacing techniques, stamping, and samples. Assuming the extracted features are an accurate representation of the plastic deformation zone of the stamped serial number and non-stamped area regardless of the degree of contrast between them, ACIP is a robust method for features pattern recognition to identify the defaced serial number. With fusion classification, the risk of misclassification was minimized, assuring the correct identification of a number or a letter.

6.1 Future Work

The lock-in procedure and automatic character identification protocol (ACIP) developed in this study will be compared with the standard method of serial number restoration, chemical etching, performed by the Crime Lab on various types of samples.

References

1. Unobe, Ikwulono David. Development of a Non-Destructive Technique for the Restoration of Defaced Serial Numbers. Retrieved May 10, 2019, from search.ebscohost.com/login.aspx?direct=true&db=cat06825a&AN=isu.b2268250&site=eds-live&scope=site.
2. Ikwulono Unobe, Lisa Lau, John Kalivas, Rene Rodriguez, & Andrew Sorensen. (2019). Restoration of defaced serial numbers using lock-in infrared thermography (Part I). *Journal of Spectral Imaging*, *8*(1), a19. https://doi-org.libpublic3.library.isu.edu/10.1255/jsi.2019.a19
3. Identification Markings Placed on Firearms (98R-341P). (2001, August 03). Retrieved June 20, 2020, from https://www.federalregister.gov/documents/2001/08/03/01-19418/identification-markings-placed-on-firearms-98r-341p
4. L. Nickolls, The scientific investigation of crime, Butterworth, London, 1956.
5. M.A.M. Zaili, R. Kuppuswamy, H. Harun, Restoration of engraved marks on steel surfaces by etching technique, Forensic Sci. Int. 171 (2007) 27–32.
6. G. Wightman, J. Matthew, Restoration of stamp marks on steel components, Forensic Sci. Int. 180 (2008) 32–36. doi:10.1016/J.FORSCIINT.2008.06.017.
7. D.E. Polk, B. Giessen, Metallurgical aspects of serial number recovery, AFTE J. 21 (1989) 174–181.
8. Guijun Yang, & Soo-Jin Park. (2019). Deformation of Single Crystals, Polycrystalline Materials, and Thin Films: A Review. *Materials*, *12*(12), 2003.
9. Branch, N. A., Subhash, G., Arakere, N. K., & Klecka, M. A. (2010). Material-dependent representative plastic strain for the prediction of indentation hardness. *Acta Materialia*,

58(19), 6487–6494. https://doi-org.libpublic3.library.isu.edu/DOI: 10.1016/j.actamat.2010.08.010.

10. A. Killey, J.P. Sargent, Analysis of thermal nondestructive testing, J. Phys. D. Appl. Phys. 22 (1989) 216–224. doi:10.1088/0022-3727/22/1/032.
11. P.J. Shull, Nondestructive evaluation: theory, techniques, and applications, CRC press, 2016.
12. C. Ibarra-Castanedo, M. Genest, S. Guibert, J.-M. Piau, X.P. V Maldague, A. Bendada, Inspection of aerospace materials by pulsed thermography, lock-in thermography, and vibrothermography: a comparative study, in: Thermosense XXIX, International Society for Optics and Photonics, 2007: p. 654116.
13. C. Ibarra-Castanedo, J.-M. Piau, S. Guilbert, N.P. Avdelidis, M. Genest, A. Bendada, X.P. V Maldague, Comparative study of active thermography techniques for the nondestructive evaluation of honeycomb structures, Res. Nondestruct. Eval. 20 (2009) 1–31.
14. O. Breitenstein, W. Warta, M. Langenkamp, Lock-in Thermography - Basics and Use for Evaluating Electronic Devices and Materials, Berlin/ Heidelberg: Springer, 2010. doi:10.1007/978-3-642-02417-7.
15. Bauer, J., Breitenstein, O., & Wagner, J.-M. (2009). Lock-in Thermography: A Versatile Tool for Failure Analysis of Solar Cells. *Electronic Device Failure Analysis*, *11*(3), 6–12.
16. Teh, C. H., & Chin, R. T. (1988). On image analysis by the methods of moments. *IEEE Transactions on pattern analysis and machine intelligence*, *10*(4), 496-513.
17. M.R. Teague, Image analysis via the general theory of moments, J. Opt. Soc. Am. 70 (1980) 920. doi:10.1364/JOSA.70.000920.

18. G. Kumar, P.K. Bhatia, A detailed review of feature extraction in image processing systems, in: Adv. Comput. Commun. Technol. (ACCT), 2014 Fourth Int. Conf., IEEE, 2014: pp. 5–12.

19. Beyerer, J., Richter, M., & Nagel, M. (2018). *Pattern Recognition : Introduction, Features, Classifiers and Principles: Vol. First edition*. De Gruyter Oldenbourg.

20. Vincent, D. B. (2013). Pattern Recognition : Practices, Perspectives, and Challenges. Nova Science Publishers, Inc.

21. S. Chevallier, D. Bertrand, A. Kohler, P. Courcoux, Application of PLS-DA in multivariate image analysis, J. Chemom. 20 (2006) 221–229. doi:10.1002/cem.994.

22. Ballabio, D., & Consonni, V. (2013). Classification tools in chemistry. Part 1: linear models. PLS-DA. *Analytical Methods*, *5*(16), 3790-3798.

23. Peterson, L. E. (2009). K-nearest neighbor. *Scholarpedia*, *4*(2), 1883.

24. Garcia, V., Debreuve, E., & Barlaud, M. (2008, June). Fast k nearest neighbor search using GPU. In *2008 IEEE Computer Society Conference on Computer Vision and Pattern Recognition Workshops* (pp. 1-6). IEEE.

25. Liaw, A., & Wiener, M. (2002). Classification and regression by randomForest. *R news*, *2*(3), 18-22.

26. Brownfield, B., Lemos, T., & Kalivas, J. H. (2018). Consensus classification using non-optimized classifiers. *Analytical chemistry*, *90*(7), 4429-4437.

27. Kalivas, J. H. (2019). Data fusion of nonoptimized models: applications to outlier detection, classification, and image library searching. In *Data Handling in Science and Technology* (Vol. 31, pp. 345-370). Elsevier

28. Metals and metallic alloys. (n.d.). Retrieved June 20, 2020, from https://www.ggspdt.com/42a-metals-and-metallic-alloys.html

29. Chapter 7: Dislocations & Strengthening Mechanisms - ppt video online download. (n.d.). Retrieved June 20, 2020, from https://slideplayer.com/slide/8114903/

30. Christian, J. W. (1983). Some surprising features of the plastic deformation of body-centered cubic metals and alloys. *Metallurgical transactions A*, *14*(7), 1237-1256.

31. Schuh, B., Mendez-Martin, F., Völker, B., George, E. P., Clemens, H., Pippan, R., & Hohenwarter, A. (2015). Mechanical properties, microstructure and thermal stability of a nanocrystalline CoCrFeMnNi high-entropy alloy after severe plastic deformation. *Acta Materialia*, *96*, 258-268.

32. Atallah, S. (1966). A relationship between emissivity and thermal conductivity of metals. *British journal of applied physics*, *17*(4), 573.

33. Branch, N. A., Subhash, G., Arakere, N. K., & Klecka, M. A. (2010). Material-dependent representative plastic strain for the prediction of indentation hardness. *Acta materialia*, *58*(19), 6487-6494.

34. Treptow, R. S. (1978). Handbook of methods for the restoration of obliterated serial numbers.

35. White, R. M., & Keller, R. R. (2015). Restoration of firearm serial numbers with electron backscatter diffraction (EBSD). *Forensic science international*, *249*, 266-270.

36. Necker, C., & Forsyth, R. (2010). The potential application of EBSD to serial number restoration. Microscopy and Microanalysis, 16(S2), 1578-1579.

37. G.S. Klees, The restoration or detection of obliterated laser-etched firearm markings by scanning electron microscopy and x-ray mapping, AFTE J. 41 (2009) 184–187.

38. Wolfer, D. A., & Lee, W. J. (1959). Application of magnetic principles to the restoration of serial numbers. *J. Crim. L. & Criminology*, *50*, 519.

39. G. Peeler, S. Gutowski, S. Wrobel, The Restoration of Impressed Characters on Aluminum Alloy Motorcycle Frames, J. Forensic Identif. 58 (2008) 27–32.

40. P.B. Wilson, The Restoration of Erased Serial Identification Marks, Police J. Theory, Pract. Princ. 52 (1979) 233–242. doi:10.1177/0032258X7905200304.

41. M. Okayasu, K. Sato, M. Mizuno, A new etching technique for revealing the plastic deformation zone in an Al–Cu–Mg alloy, J. Mater. Sci. 43 (2008) 2792–2798.

42. J.I. Thornton, P.J. Cashman, The mechanism of the restoration of obliterated serial numbers by acid etching, J. Forensic Sci. Soc. 16 (1976) 69–71.

43. G. Wightman, J. Matthew, Restoration of stamp marks on steel components, Forensic Sci. Int. 180 (2008) 32–36. doi:10.1016/J.FORSCIINT.2008.06.017.

44. A.J. Çengel, Yunus A.; Ghajar, Heat and Mass Transfer: Fundamentals & Applications, McGraw-Hill Higher Education, 2015.

45. C.R. Dalton, B.W. Olson, F.C. Lai, Nondestructive evaluation of surface defects using scanning infrared thermography, J. Thermophys. Heat Transf. 23 (2009) 716–724.

46. M. Airouche, L., AR. Al-Kassir, J., A.J.. Arenas, F., B.C.. Arrue, A., G. Bebis, A., M. Bertozzi, A., . . . Y. Zhou, P. (1970, January 01). Thermal cameras and applications: A survey. Retrieved June 20, 2020, from https://link.springer.com/article/10.1007/s00138-013-0570-5

47. K. Cramer, P. Howell, H. Syed, Quantitative thermal imaging of aircraft structures, in: Thermosense XVII An Int. Conf. Therm. Sens. Imaging Diagnostic Appl., 1995: pp. 226–233. 161

48. Strzałkowski, K., Streza, M., & Pawlak, M. (2015). Lock-in thermography versus PPE calorimetry for accurate measurements of thermophysical properties of solid samples: A comparative study. *Measurement*, *64*, 64–70. https://doi-org.libpublic3.library.isu.edu/DOI: 10.1016/j.measurement.2014.12.040.

49. M. Choi, K. Kang, J. Park, W. Kim, K. Kim, Quantitative determination of a subsurface defect of reference specimen by lock-in infrared thermography, NDT E Int. 41 (2008) 119–124. doi:10.1016/J.NDTEINT.2007.08.006.

50. O. Breitenstein, C. Schmidt, D. Karg, Thermal failure analysis by IR lock-in thermography, Microelectron. Fail. Anal. Desk Ref. Fifth Ed. EDFAS. (2004).

51. W. Bai, B.S. Wong, Evaluation of defects in composite plates under convective environments using lock-in thermography, Meas. Sci. Technol. 12 (2001) 142–150. doi:10.1088/0957-0233/12/2/303.

52. Wolf, C., Jolion, J. M., & Chassaing, F. (2002, August). Text localization, enhancement and binarization in multimedia documents. In *Object recognition supported by user interaction for service robots* (Vol. 2, pp. 1037-1040). IEEE.

53. Maragos, P., Schafer, R. W., & Butt, M. A. (Eds.). (2012). *Mathematical morphology and its applications to image and signal processing* (Vol. 5). Springer Science & Business Media.

54. C. Qing, Evaluation of OCR Algorithms for Images with Different Spatial Resolution and Noise, 2003.

55. J.M. Prats-Montalbán, A. de Juan, A. Ferrer, Multivariate image analysis: A review with applications, Chemom. Intell. Lab. Syst. 107 (2011) 1–23. doi:10.1016/J.CHEMOLAB.2011.03.002.

56. P. Geladi, H. Grahn, Multivariate image analysis, Wiley, 1996.

57. I.T. Jolliffe, Principal component analysis, Springer, 2002.

58. C. Suh, A. Rajagopalan, X. Li, K. Rajan, The application of Principal Component Analysis to materials science data, Data Sci. J. 1 (2002) 19–26. doi:10.2481/dsj.1.19.

59. Rajic, N. (2002). Principal component thermography for flaw contrast enhancement and flaw depth characterisation in composite structures. *Composite structures*, *58*(4), 521-528.

60. Bledsoe, W. W., & Browning, I. (1959, December). Pattern recognition and reading by machine. In *Papers presented at the December 1-3, 1959, eastern joint IRE-AIEE-ACM computer conference* (pp. 225-232).

61. ping Tian, D. (2013). A review on image feature extraction and representation techniques. *International Journal of Multimedia and Ubiquitous Engineering*, *8*(4), 385-396.

62. Matus, F., & Flusser, J. (1993). Image representation via a finite Radon transform. *IEEE Transactions on Pattern Analysis and Machine Intelligence*, *15*(10), 996-1006.

63. Jégou, H., Douze, M., Schmid, C., & Pérez, P. (2010, June). Aggregating local descriptors into a compact image representation. In *2010 IEEE computer society conference on computer vision and pattern recognition* (pp. 3304-3311). IEEE.

64. Choras, R. S. (2007). Image feature extraction techniques and their applications for CBIR and biometrics systems. *International journal of biology and biomedical engineering*, *1*(1), 6-16.

65. Mingqiang, Y., Kidiyo, K., & Joseph, R. (2008). A survey of shape feature extraction techniques. *Pattern recognition*, *15*(7), 43-90.

66. Kumar, G., & Bhatia, P. K. (2014, February). A detailed review of feature extraction in image processing systems. In *2014 Fourth international conference on advanced computing & communication technologies* (pp. 5-12). IEEE.

67. Liu, C. L., Nakashima, K., Sako, H., & Fujisawa, H. (2004). Handwritten digit recognition: investigation of normalization and feature extraction techniques. *Pattern Recognition*, *37*(2), 265-279.

68. Medjahed, S. A. (2015). A comparative study of feature extraction methods in images classification. *International journal of image, graphics and signal processing*, *7*(3), 16.

69. Suykens, J. A., & Vandewalle, J. (1999). Least squares support vector machine classifiers. *Neural processing letters*, *9*(3), 293-300.

70. Chua, L. O., & Yang, L. (1988). Cellular neural networks: Theory. *IEEE Transactions on circuits and systems*, *35*(10), 1257-1272.

71. Sarle, W. S. (1994). Neural networks and statistical models.

72. Yegnanarayana, B. (2009). *Artificial neural networks*. PHI Learning Pvt. Ltd.

73. Khotanzad, A., & Hong, Y. H. (1990). Invariant image recognition by Zernike moments. *IEEE Transactions on pattern analysis and machine intelligence*, *12*(5), 489-497.

74. Pang, Y. H., BJ, A. T., & CL, D. N. (2005). Enhanced pseudo Zernike moments in face recognition. *IEICE Electronics Express*, *2*(3), 70-75.

75. Chong, C. W., Raveendran, P., & Mukundan, R. (2003). The scale invariants of pseudo-Zernike moments. Pattern Analysis & Applications, 6(3), 176-184.

76. YE, B., & PENG, J. X. (2003). Improvement and invariance analysis of pseudo-Zernike moments. *Journal of Image and Graphics*, *3*.

77. Khotanzad, A., & Hong, Y. H. (1990). Rotation invariant image recognition using features selected via a systematic method. *Pattern recognition*, *23*(10), 1089-1101.

78. C. Singh, P. Sharma, Performance analysis of various local and global shape descriptors for image retrieval, Multimed. Syst. 19 (2013) 339–357. doi:10.1007/s00530-012-0288-7.

79. Papakostas, G. A., Boutalis, Y. S., Karras, D. A., & Mertzios, B. G. (2010). Efficient computation of Zernike and Pseudo-Zernike moments for pattern classification applications. *Pattern Recognition and Image Analysis*, *20*(1), 56-64.

80. C. Singh, E. Walia, R. Upneja, Accurate calculation of Zernike moments, Inf. Sci. (Ny). 233 (2013) 255–275. doi:10.1016/J.INS.2013.01.012.

81. F. Ghorbel, S. Derrode, R. Mezhoud, T. Bannour, S. Dhahbi, Image reconstruction from a complete set of similarity invariants extracted from complex moments, Pattern Recognit. Lett. 27 (2006) 1361–1369.

82. Ballabio, D., & Consonni, V. (2013). Classification tools in chemistry. Part 1: linear models. PLS-DA. *Analytical Methods*, *5*(16), 3790-3798.

83. Da Silva, V. A., Talhavini, M., Peixoto, I. C., Zacca, J. J., Maldaner, A. O., & Braga, J. W. (2014). Non-destructive identification of different types and brands of blue pen inks in cursive handwriting by visible spectroscopy and PLS-DA for forensic analysis. *Microchemical Journal*, *116*, 235-243.

84. Worley, B., Halouska, S., & Powers, R. (2013). Utilities for quantifying separation in PCA/PLS-DA scores plots. Analytical biochemistry, 433(2), 102-104.

85. PLS-DA. (n.d.). Retrieved June 22, 2020, from https://imdevsoftware.wordpress.com/tag/pls-da/

86. Weinberger, K. Q., Blitzer, J., & Saul, L. K. (2006). Distance metric learning for large margin nearest neighbor classification. In *Advances in neural information processing systems* (pp. 1473-1480).

87. Zhang, M. L., & Zhou, Z. H. (2005, July). A k-nearest neighbor based algorithm for multi-label classification. In 2005 IEEE international conference on granular computing (Vol. 2, pp. 718-721). IEEE.

88. Ali, A. (2019, November 24). K-Nearest Neighbor with Practical Implementation. Retrieved June 22, 2020, from https://medium.com/machine-learning-researcher/k-nearest-neighbors-in-machine-learning-e794014abd2a

89. Huang, X., & Zhang, L. (2012). An SVM ensemble approach combining spectral, structural, and semantic features for the classification of high-resolution remotely sensed imagery. IEEE transactions on geoscience and remote sensing, 51(1), 257-272.

90. Mohiuddin, K. M., & Mao, J. (1994). A comparative study of different classifiers for handprinted character recognition. In *Machine Intelligence and Pattern Recognition* (Vol. 16, pp. 437-448). North-Holland.

91. Precision Forensic Testing, Stamped Serial Number Restoration Metal – Precision Forensic Testing, (n.d.). https://www.precisionforensictesting.com/collections/crime-laboratory-products/products/stamped-serial-number-restoration-metal (accessed June 20, 2018).

92. De Maesschalck, R., Jouan-Rimbaud, D., & Massart, D. L. (2000). The mahalanobis distance. Chemometrics and intelligent laboratory systems, 50(1), 1-18.

93. Kalivas, J. H. (2019). Data fusion of nonoptimized models: applications to outlier detection, classification, and image library searching. In *Data Handling in Science and Technology* (Vol. 31, pp. 345-370). Elsevier.

94. Brereton, R. G. (2009). *Chemometrics for pattern recognition*. John Wiley & Sons.

95. Gower, J. C. (1975). Generalized procrustes analysis. Psychometrika, 40(1), 33-51.

96. Kittler, J., & Alkoot, F. M. (2003). Sum versus vote fusion in multiple classifier systems. IEEE transactions on pattern analysis and machine intelligence, 25(1), 110-115.

97. D.L. Hall, J. Llinas, An introduction to multisensor data fusion, Proc. IEEE. 85 (1997) 6–23. doi:10.1109/5.554205.

Appendix I: Images of Reference Alphanumeric Characters

Thirty-six alphanumeric characters (0-9 and A-Z) (25 distinct Microsoft Fonts)

Font style: Normal and Italics

This resource was prepared by the author(s) using Federal funds provided by the U.S. Department of Justice. Opinions or points of view expressed are those of the author(s) and do not necessarily reflect the official position or policies of the U.S. Department of Justice.

12a. 

12b. 

13a. 

13b. 

14a. 

14b. 

15a. 

15b. 

16a. 

16b. 

17a. 

17b. 

18a. 

18b. 

19a. 

19b. 

20a. 

20b. 

21a. 

21b. 

22a. 

22b. 

23a. 

23b. 

24a. 

24b. 

25a. 

25b. 

Index	Fonts (a = normal and b = italics)
1a. and 1b.	Gungsuh
2a. and 2b.	Franklin Gothic Book
3a. and 3b.	Segoe UI Black
4a. and 4b.	Cambria Math
5a. and 5b.	Arial
6a. and 6b.	New Gothic MT
7a. and 7b.	Abadi
8a. and 8b.	Agency FB
9a. and 9b.	Bahnschrift
10a. and 10b.	Bookman Old Style
11a. and 11b.	Baskerville Old Face
12a. and 12b.	Bauhaus
13a. and 13b.	Bernard MT Conc
14a. and 14b.	Bodoni MT Posted
15a. and 15b.	Bodoni MT
16a. and 16b.	Rockwell
17a. and 17b.	Comic Sans MS
18a. and 18b.	Segoe Print
19a. and 19b.	Showcard Gothic
20a. and 20b.	Wide Latin
21a. and 21b.	Goudy Stout
22a. and 22b.	Cooper Black
23a. and 23b.	OCRB,
24a. and 24b.	Biome
25a. and 25b.	Niagara Gold

Appendix II: Similar reference class

Table AII-1 Breakdown of similar classes within Microsoft font reference classes (0-9 and A-Z)

Class	Similar Class					
	RM			PZM		
	35% (ED<0.137)	50% (ED<0.138)	65% (ED<0.128)	35% (ED<0.132)	50% (ED<0.133)	65% (ED<0.132)
0	D G O Q U	D G O Q U	D G O Q U	69DGOQR	6 9 G O Q	6 9 O
1	I	I	I	I	I	I
2				S		
3						
4						
5	S	S		S	S	
6	G	G		0 G O	0 G O	O G O
7						
8	B H S	B H	B	B R S	B S	
9				0 O	0 O	0 O
A						
B	8 B H	8 B H	8 D	8 R S	8 D R U	U
C						
D	0 B O U	0 B O	0 B O	0 B R U	B	
E						
F	P	P	P			
G	0 6 O U	0 6 O	0	0 6 O U	0 6 O	6
H	8 B M N R	8 B N R	N R	B R U	R U	R
I	1	1	1	1	1	1
J						
K			X	R		
L						
M	H			N	N	N
N	H	H	H	M R	M	M
O	0 D G Q U	0 D G Q U	0 D	0 6 9 G Q	0 6 9 G Q	0 6 9
P	F	F	F			
Q	0 O	0 O	0	0 O	0 O	
R	H	H	H	08BDHKNS	B H	H
S	5 8	5		2 5 8 R	5 8	
T						
U	0 D G O	0 D O	0	B D G H R	B H	B
V				Y		
W						
X			K			
Y				V		
Z						

This resource was prepared by the author(s) using Federal funds provided by the U.S. Department of Justice. Opinions or points of view expressed are those of the author(s) and do not necessarily reflect the official position or policies of the U.S. Department of Justice.

Appendix III: Additional Results

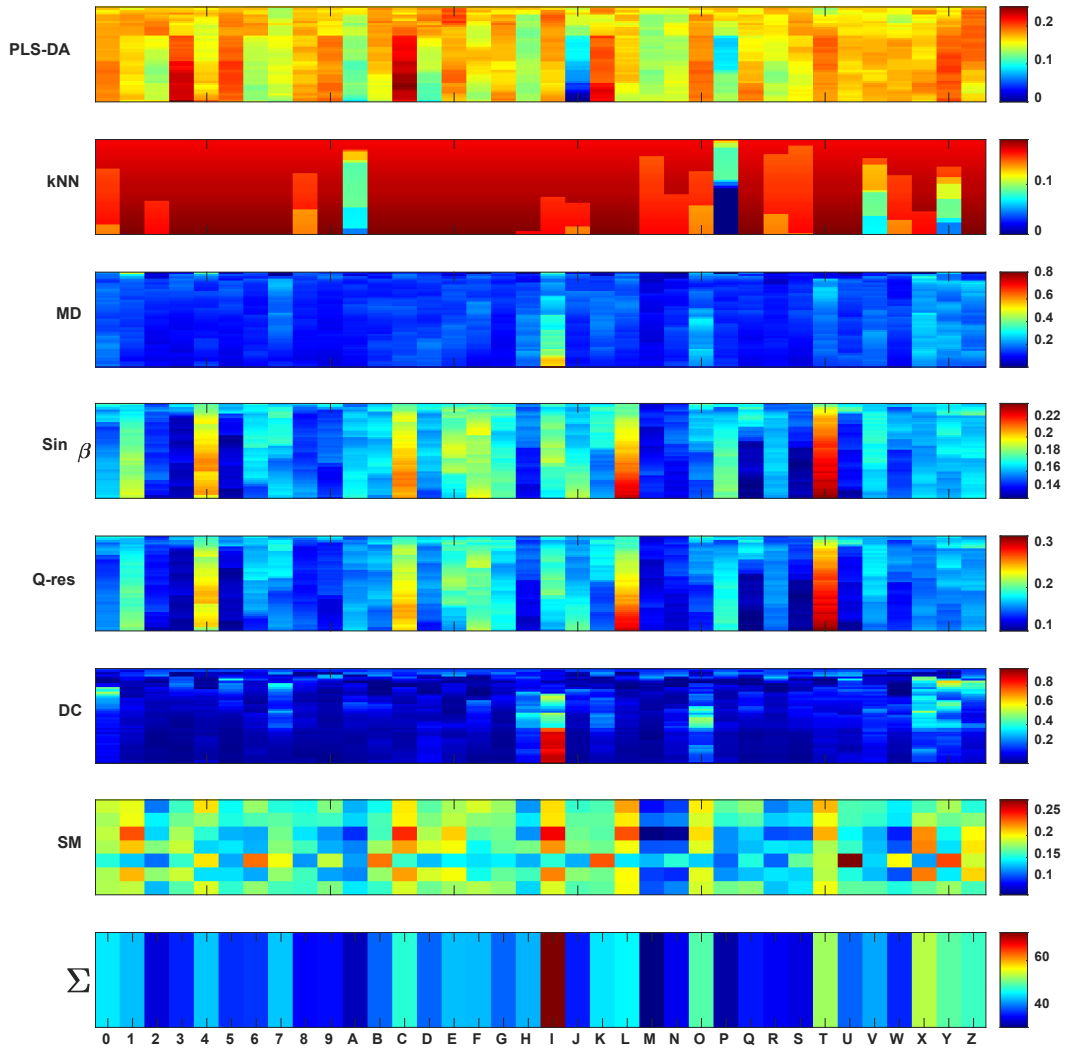

Figure AIII-1 Fusion Classification input matrix and sum fusion value (undefaced 2 - replicate) with PZM of a specific proportion (35%)

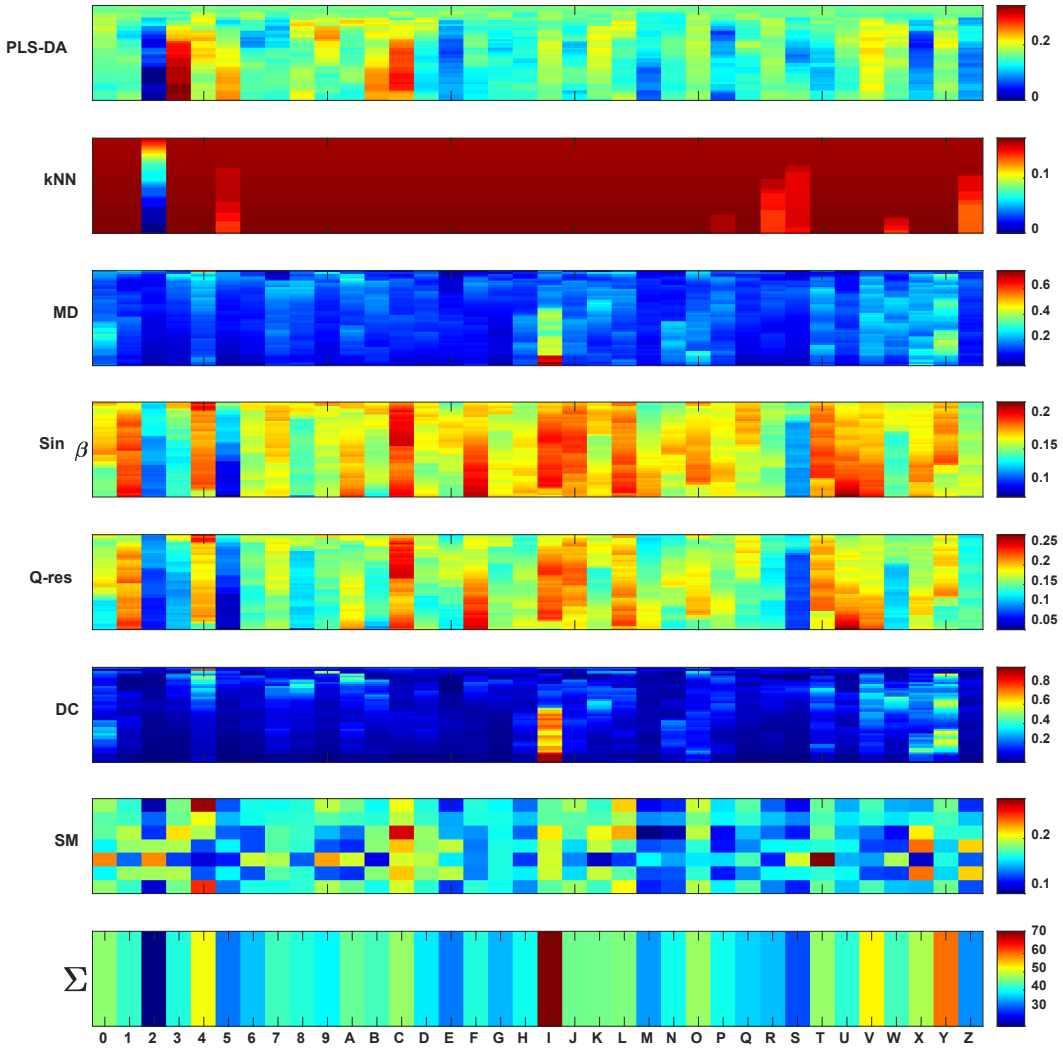

Figure AIII-2 Fusion Classification input matrix and sum fusion value (undefaced 2 - replicate) with PZM of a specific proportion (65%)

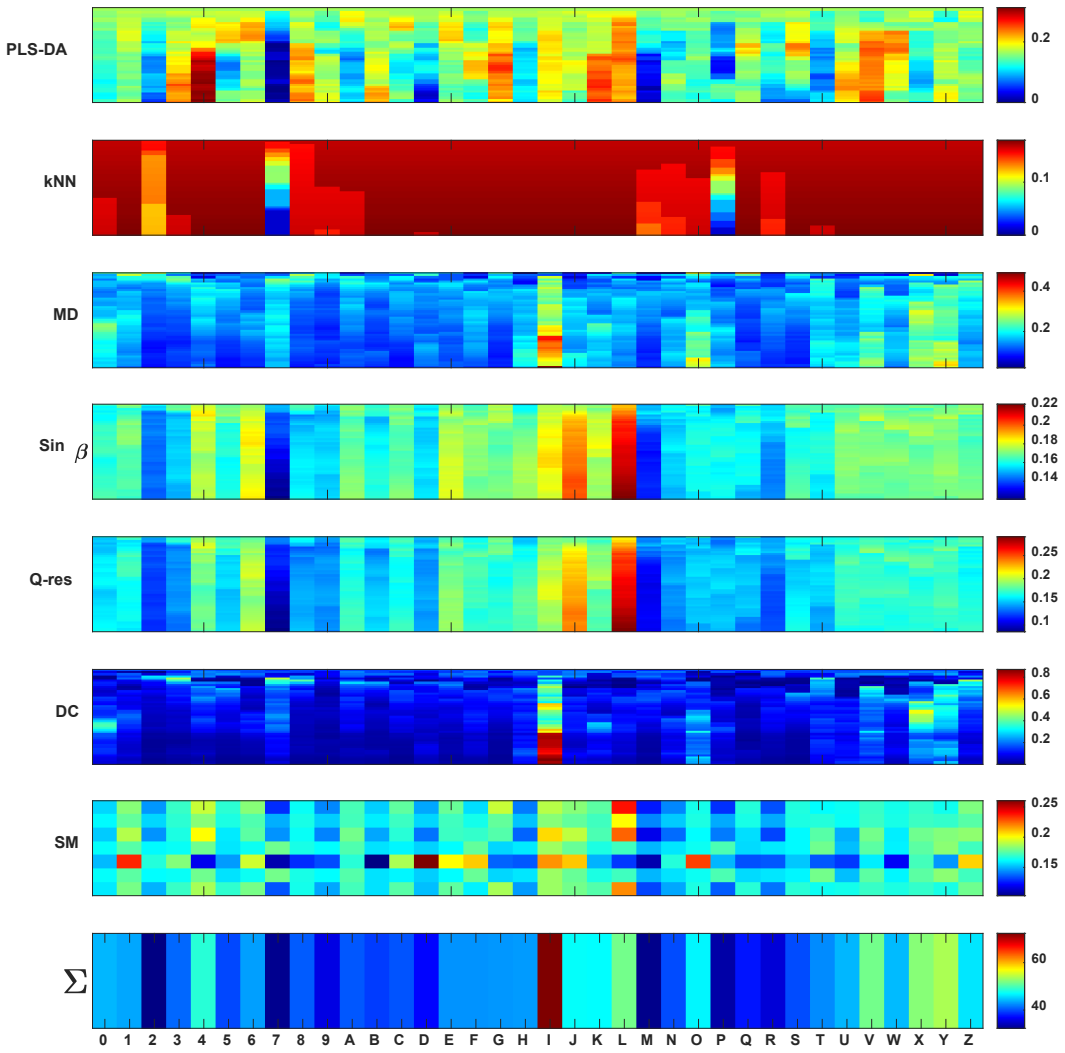

Figure AIII-3 Fusion Classification input matrix and sum fusion value (undefaced 2 - replicate) with RM a specific proportion (35%)

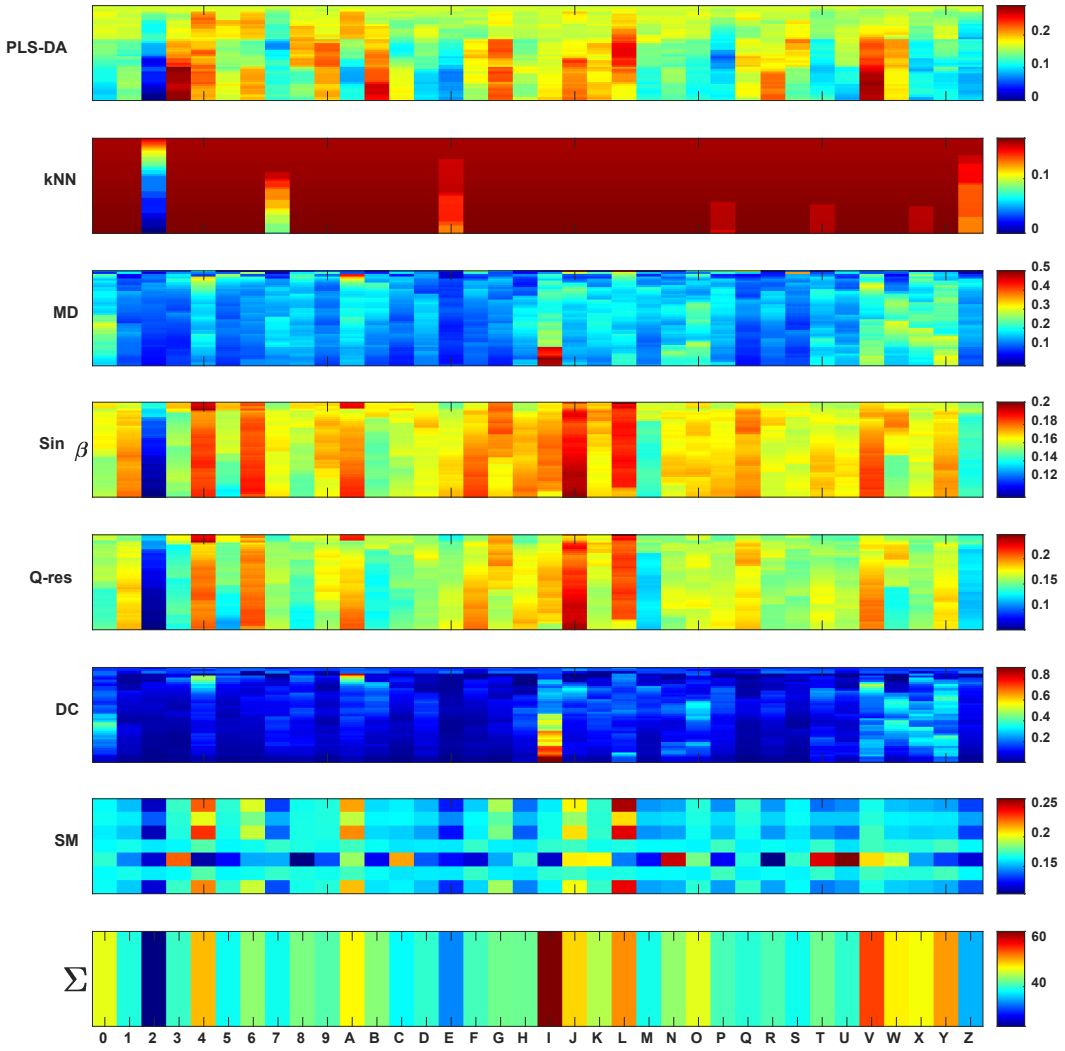

Figure AIII-4 Fusion Classification input matrix and sum fusion value (undefaced 2 - replicate) with RM of a specific proportion (65%)

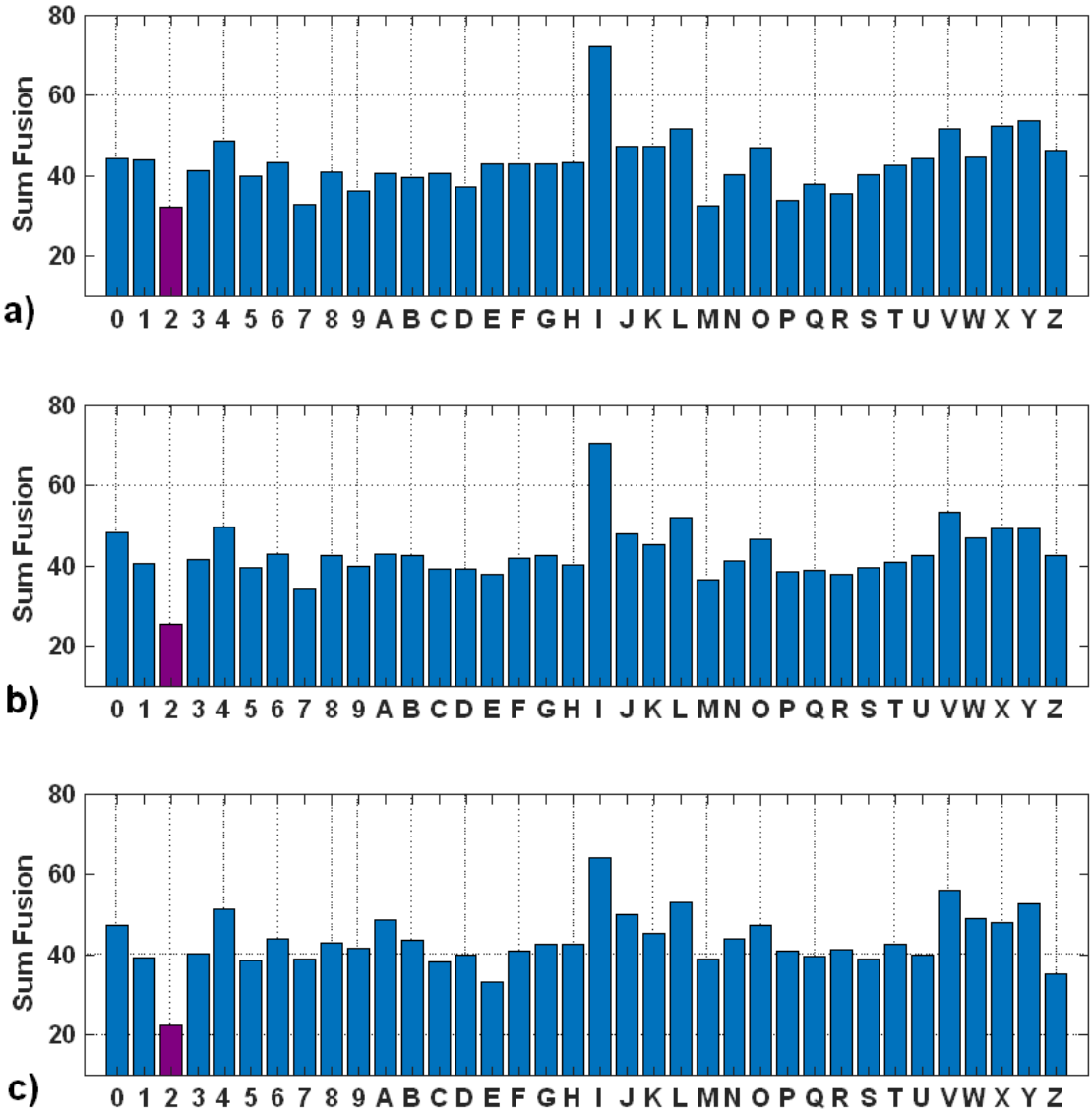

Figure AIII-5 Bar plot of Sum Fusion for a replicate of undefaced two with RM and varying object percentage a)35%, b) 50% and c) 65%. The magenta color bars represent the lowest sum fusion value (lowest rank)

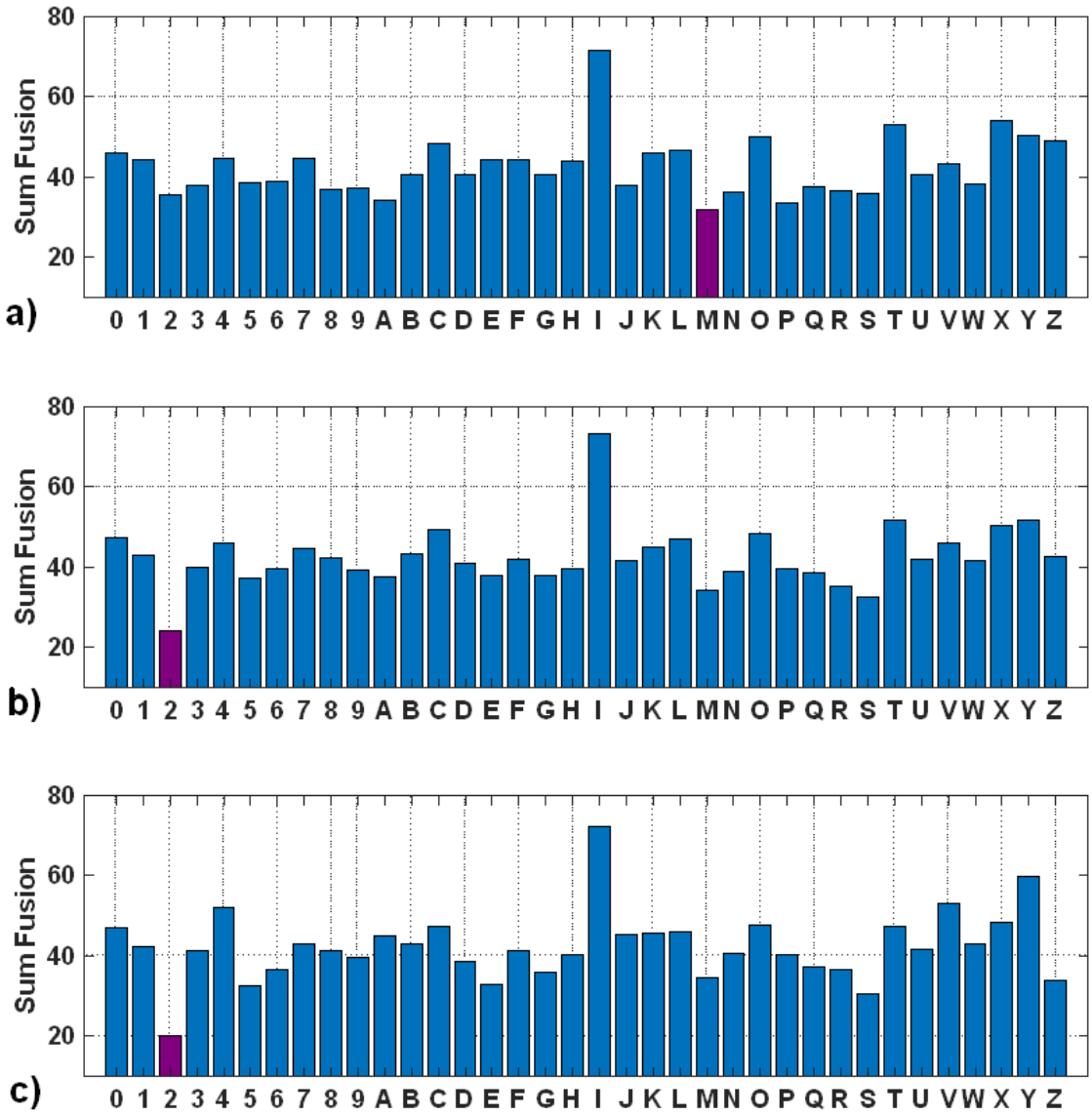

Figure AIII-6 Bar plot of Sum Fusion for a replicate of undefaced two with PZM and varying object percentage a)35%, b) 50% and c) 65%. The magenta color bars represent the lowest sum fusion value (lowest rank)

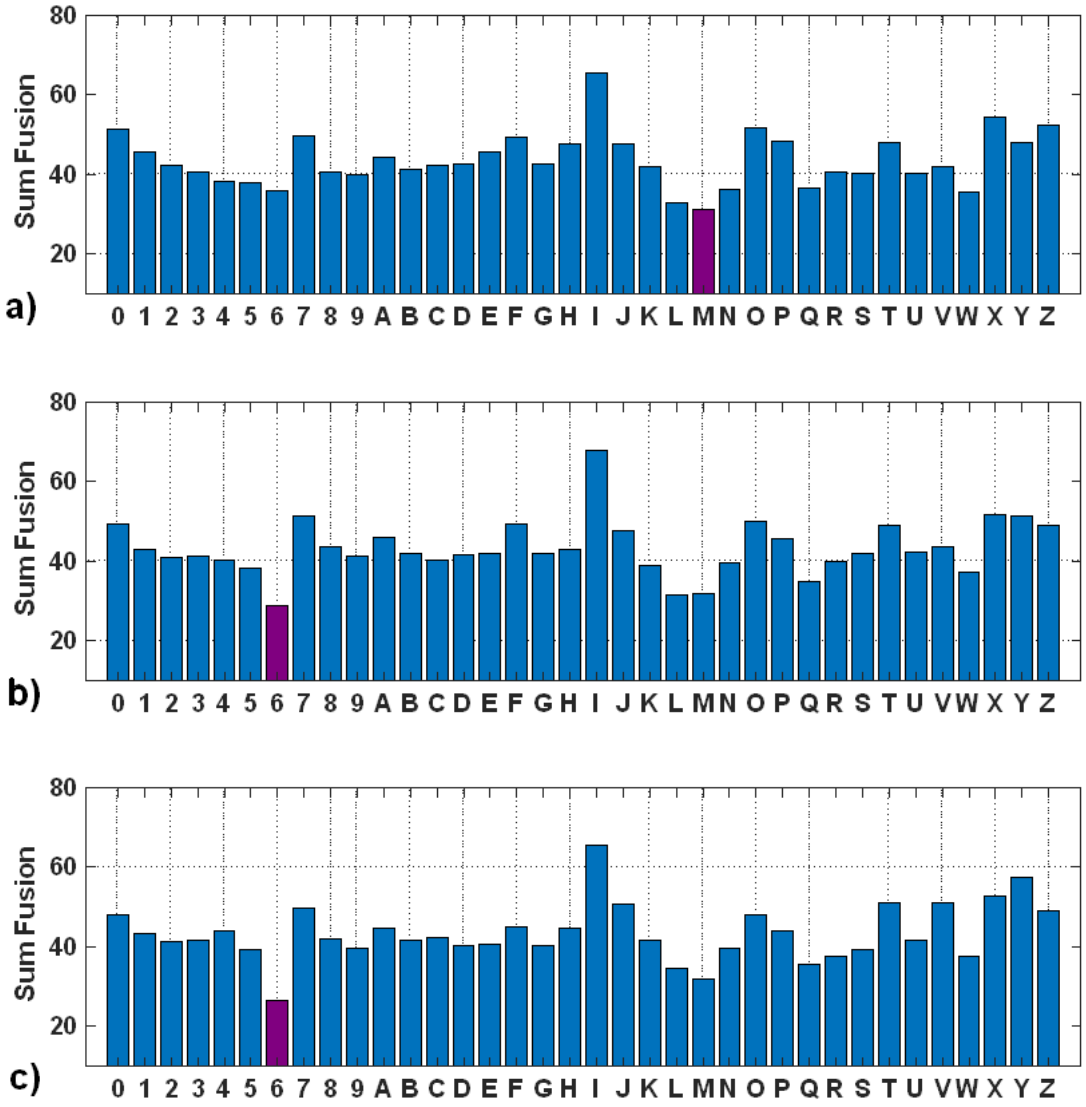

Figure AIII-7 Bar plot of Sum Fusion for an original of partially defaced six with RM and varying object percentage a)35%, b) 50% and c) 65%. The magenta color bars represents the lowest fusion value (lowest rank)

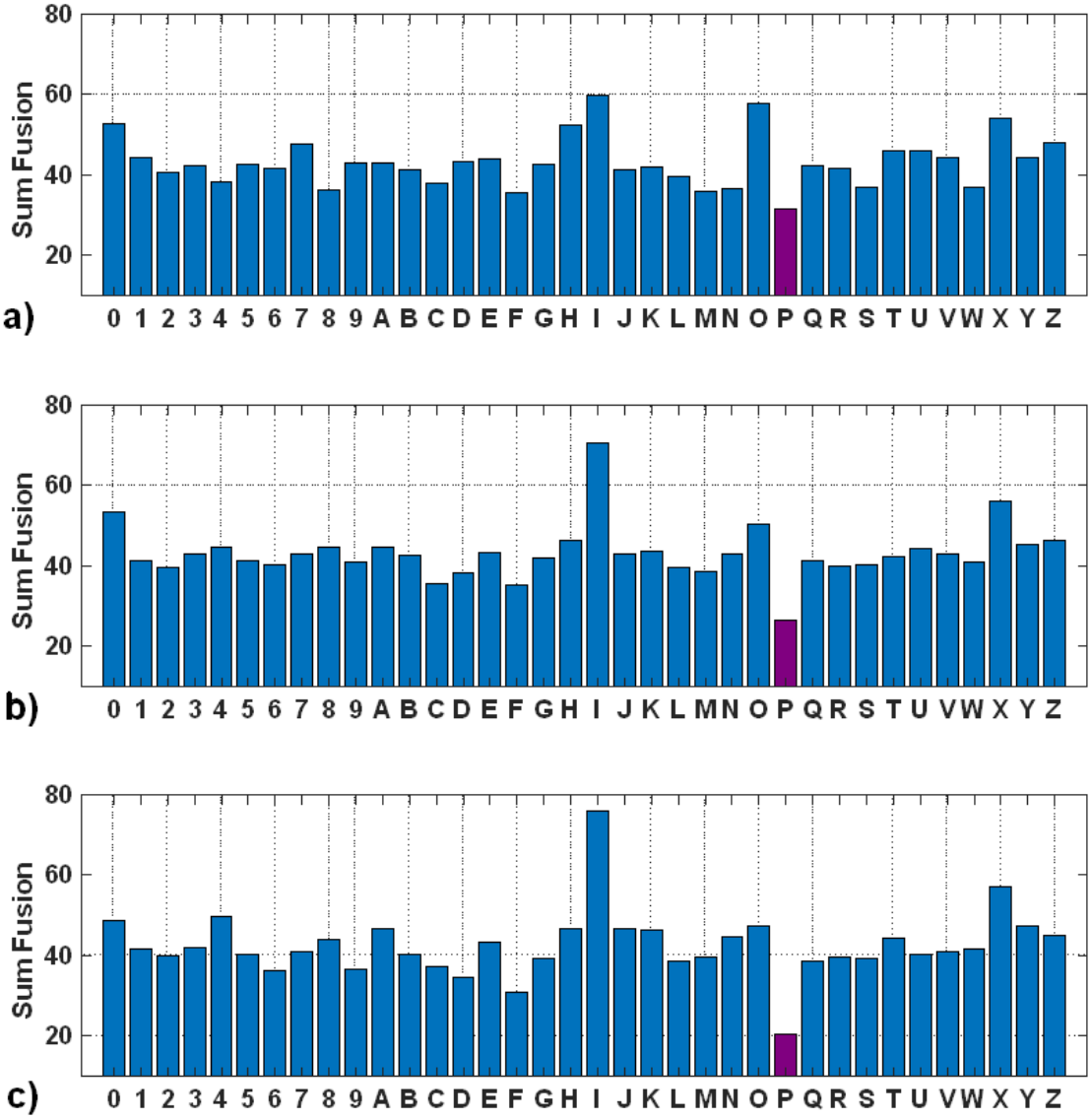

Figure AIII-8 Bar plot of Sum Fusion for an original of partially defaced six with PZM and varying object percentage a)35%, b) 50% and c) 65%. The magenta color bars represent the lowest sum fusion value (lowest rank)